U.S. Department of Transportation
OST-R CRS&SI Technologies Program – Phase VI –

Final Report

Research Title: Quantitative Sensing of Bridges, Railways, and Tunnels with Autonomous Unmanned Aerial Vehicles

Contract Number: OASRTRS-14-H-UML

Reporting Period: 9/15/2014 ~ 12/14/2016

Project Ending Period: 12/14/2016

Principal Investigator: Tzuyang Yu
Associate Professor/Associate Chair for Doctoral Studies
Department of Civil and Environmental Engineering
University of Massachusetts Lowell
Lowell, Massachusetts 01854-2827

Program Manager: Caesar Singh, P.E.
Office of the Assistant Secretary for Research and Technology,
U.S. Department of Transportation
1200 New Jersey Avenue, SE, E33-467
Washington, DC 20590

Lowell, Massachusetts
May 4, 2017

TABLE OF CONTENTS

GLOSSARY

CWIR: Continuous Wace Imaging Radar

DIC: Digital Image Correlation

GPS: Global Positioning System

GUI: Graphic User Interface

IR: Infrared

LiDAR: Light Detection And Ranging

NDT/E/I: Nondestructive Testing/Evaluation/Inspection

PSI: Physical Sciences, Inc.

QAUAV: Quantitative Autonomous Unmanned Aerial Vehicle

Radar: RAdio Detection And Ranging

SAR: Synthetic Aperture Radar

SHM: Structural Health Monitoring

SLAM: Simultaneous Localization And Mapping

TAC: Technical Advisory Council

UAV: Unmanned Aerial Vehicle

UML: University of Massachusetts Lowell

EXECUTIVE SUMMARY

Managing a growing population of deteriorated transportation infrastructure systems (i.e. bridges, railways, tunnels) is one of biggest challenges faced by the nation. Traditional inspection and monitoring techniques (e.g., visual inspection, mechanical sounding, rebound hammer, cover meter, electrical potential measurements, ultrasound, ground penetrating radar) for bridges, railways, and tunnels require lane closure and are labor intensive and time-consuming. Existing remote sensing techniques (e.g., LiDAR, aerial photos) using fixed-wing aircraft are capable of conducting large-area inspection but are constrained by viewing areas accessible only from above, at a large distance, and are not capable of inspecting all areas of interest (e.g., bridge piers, bridge girder bottom, and tunnel walls). Automated, low-cost, efficient inspection techniques for interrogating critical components of bridges, railways, and tunnels are needed. The objective of this project is to develop a system-level, decision-support unmanned aerial vehicle (UAV) sensing system for the autonomous, efficient inspection of bridges, railways, and tunnels, using radar, digital image correlation, and thermal sensors. The proposed UAV sensing system represents the next generation of rapid, low-cost interrogation technology for infrastructure inspection and monitoring of critical transportation infrastructure.

In this final report, major research achievements and findings from our conducted tasks are summarized and reported. Additional technical details in our research tasks can be found in submitted quarterly reports. The objective of this project is to develop an unmanned aerial vehicle (UAV) system that can be used to autonomously interrogate numerous areas on civil structures easily without requiring expensive, time consuming aerial lifts or inconsistent visual inspections. The proposed sensing platform includes innovative continuous wave imaging radar and digital image correlation to monitor structures or quantify damage. This project represents the next generation of localized, autonomous inspection and monitoring methods using robotic platform.

Chapter 1. Introduction

Efficient inspection of bridges, railways, and tunnels for their post-hazards response is a challenging task. Manmade and natural hazards including terrorism, earthquakes, floods, and hurricanes, as well as material deterioration and aging can reduce the safety margin of the structures and result in the need for repair. Failures of bridges, railways, tunnels cause inventory loss to the nation, transportation cost to road users, and can result in fatalities. In the President's FY 2014 budget request, "Building a 21st Century Infrastructure" is emphasized by "providing $50 billion for upfront infrastructure investments, including $40 billion for "Fix it First" projects, to invest immediately in repairing highways, bridges, transit systems, and airports nationwide; and $10 billion for competitive programs to encourage innovation in completing high-value infrastructure projects." To achieve the goal of good repair, good inspection is necessary to provide the information regarding the level of repair needed and the area to repair. Fig. 1 shows recent examples of bridge and tunnel failures.

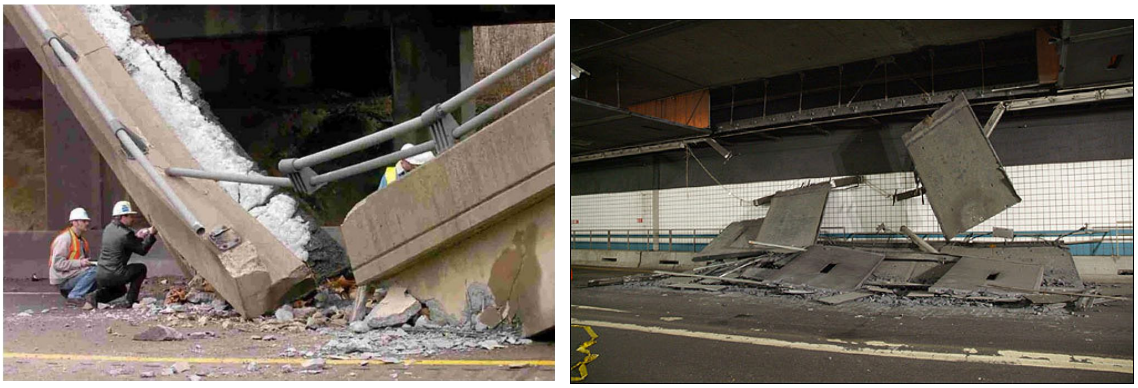

Fig. 1. Bridge and tunnel failures: (left) I-70 Lake View Drive Bridge (Pittsburgh, PA) and (right) I-93 Tunnel (Boston, MA)

The current status of inspection and monitoring technologies (visual inspection, mechanical sounding, rebound hammer, cover meter, electrical half-cell potential (HCP), ultrasonic testing (UT), acoustic emission (AE), ground penetrating radar (GPR), fiber optic sensor (FOS), LiDAR (light detection and ranging), and laser Doppler vibrometer (LDV)), are either: **(i)** time-consuming and labor intensive (e.g., visual inspection and all contact inspection methods), or **(ii)** only capable of very large area inspection with low resolution (e.g. aerial fixed-wing remote sensing), or **(iii)** only capable of performing open-space inspection and cannot access all areas in limited space (e.g., underside of a bridge, tunnel walls), or **(iv)** equipped with heavy platform/vehicles (e.g., GPR, LDV). Safety issues, interference with traffic, and subjective evaluation are additional disadvantages associated with some of the traditional inspection techniques. Fig. 2 shows a few typical inspection scenarios using visual inspection, UT, HCP, and GPR.

A new system-level, decision-support unmanned aerial vehicle (UAV) sensor is proposed for the quantitative, autonomous, efficient inspection of bridges, railways, and tunnels, utilizing imaging radar, digital image correlation (DIC), and thermal sensors. In

the proposed UAV sensing platform, a decision-support asset analysis tool is first used to **(i)** perform and assessment of of the aging infrastructure systems and **(ii)** prioritize the structures in need of inspection/repair. This analysis is performed based on the impact of each aged/deteriorated structure on various local traffic networks, using previous inspection records/reports. Once this system-level analysis is completed, the UAV sensing system will be sent to the structure with the highest inspection priority. The proposed UAV sensing platform (called "CivilEye") is designed to carry imaging radar, digital image correlation (DIC), and thermal imaging sensors and is wirelessly controlled by a ground control station. The imaging radar sensor is sensitive to conductive targets and will be used to detect surface/subsurface cracking in concrete structures, as well as steel rebar corrosion inside concrete. The DIC sensor is capable of measuring deformation and strain and will be used to construct the large-area strain profile of the structure. Surface strain profile provided by DIC will be used to verify the subsurface image produced by imaging radar. The thermal image sensor is sensitive to temperature difference and will be used for material characterization (e.g., detecting water in concrete cracks, rust on steel members).

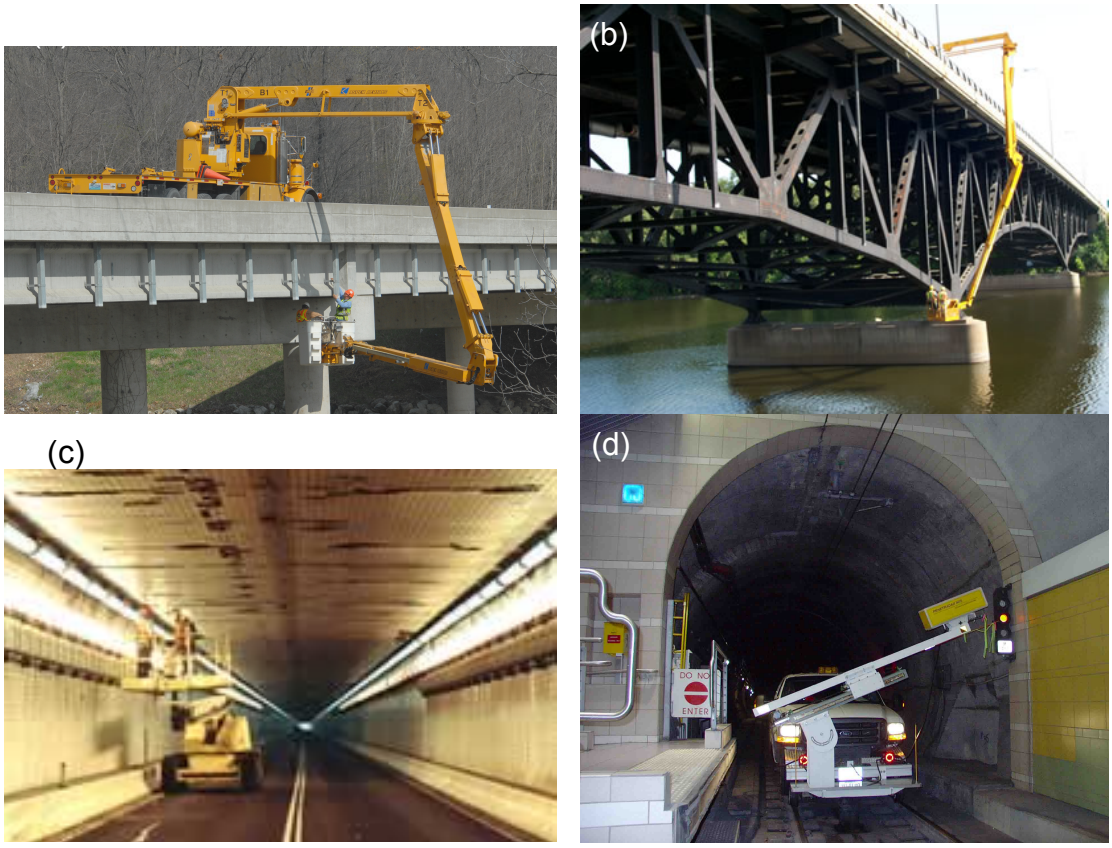

Fig. 2. Examples of bridge, railway, and tunnel inspection (a) Concrete bridge inspection (MN-DOT); (b) Steel bridge inspection (MO-DOT); (c) Tunnel inspection (FHWA); (d) Railway tunnel inspection using GPR

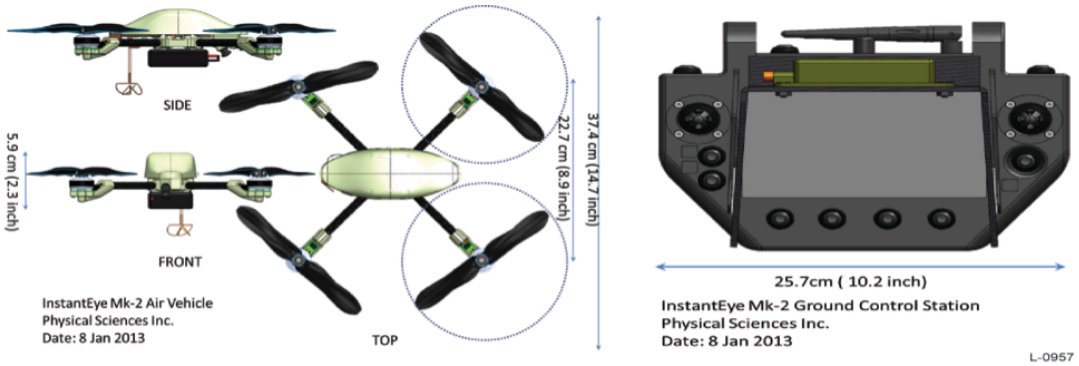

Fig. 3. InstantEye MKII Air Vehicle (left), and Ground Control Unit (right)

With the preloaded coordinates of a structure under inspection, the proposed CivilEye system performs preliminary or detailed autonomous inspection on the structure. It is expected that structural inspectors will not need to control the UAV for the pre-programmed inspection tasks as positioning the aerial platform will be automated. Fig. 3 shows a successful commercial product, InstantEye developed and manufactured by one of the team's industry members, Physical Sciences, Inc. (PSI), that serves as the foundation for creating the proposed CivilEye system. Fig. 4 illustrates the inspection scheme of the proposed CivilEye UAV in the areas/spaces difficult to access by conventional inspection techniques using a mechanical lift on special vehicles.

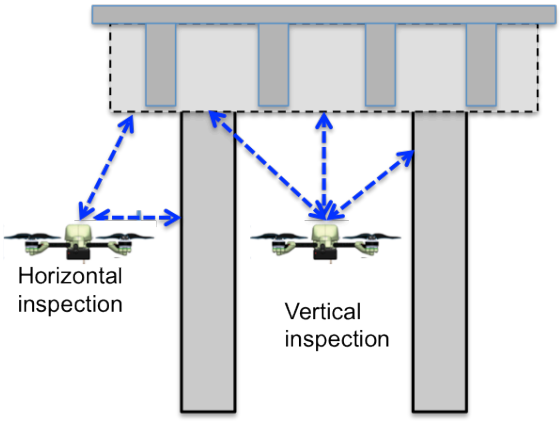

Fig. 4. Inspection scheme of the CivilEye system in the areas difficult to access

While performing autonomous inspection of structures, real-time visual images can be captured and transmitted onto the screen of the ground control unit (Fig. 3, right) for the inspector to perform preliminarily evaluation of the damage. This function allows the inspector to conduct visual inspection in parallel to the quantitative sensing the proposed CivilEye system performs.

The proposed CivilEye system will be the first high-accuracy quantitative UAV sensing system of its kind, capable of surface (mechanical strain/deformation) and subsurface (steel rebar corrosion in concrete) measurement. Different from other UAV

systems using visual images for qualitative inspection, high-accuracy position control and prediction algorithms are not required in those systems. On the other hand, in order to perform quantitative sensing of structures, the UAV system must either be able to control its position with high-accuracy or identify its position with high-accuracy.

When inspecting different structures using the proposed CivilEye system, target defects/damages are identified. For the inspection of concrete bridges, surface distress, subsurface cracking, subsurface steel rebar corrosion, and material deterioration (alkaline silicate reaction) are considered. For the inspection of steel bridges, surface corrosion/rust, surface distress due to excessive fatigue failure and invisible corrosion of bolts are considered. For the inspection of railways, steel anchor corrosion, concrete tie cracking, deformation of rails, stress concentration due to ballast pocket development, surface distress due to rail squart, and subsurface ballast pocket development are considered. For inspection of tunnels, surface distress, subsurface cracking, subsurface steel rebar corrosion, and material deterioration are considered. The operating principles of the proposed sensors and the UAV design and control algorithms, as well as the decision-support tools, are described in this final report.

Chapter 2. Literature Review

In this chapter, reported research activities regarding SAR imaging, DIC, and UAV are briefly reviewed and reported.

2.1 Synthetic Aperture Radar Imaging

Remotely inspecting concrete structures for the early detection of subsurface defects such as steel rebar corrosion is an attractive technological capability for the effective maintenance of critical civil infrastructures. Compared to surface defects (e.g., concrete cracking), subsurface defects are better candidates for early stage damage detection and structural health monitoring. Existing NDT/E (nondestructive testing/evaluation) methods are constrained by their own characteristics, preventing them from becoming a practical, subsurface remote sensing technique. For example, ultrasonic testing (UT) can detect subsurface defects in steel structures but perfect coupling between UT transducers and the structure is usually required. Subsurface imaging applications of UT on concrete structures have been reported (Krause *et al.* 2001; Schickert *et al.* 2003; Hoegh and Khazanovich 2015). Other acoustic techniques such as impact-echo also have been applied to the imaging of concrete structures (Sansalone and Street 1997). Ground penetrating radar (GPR) is capable of conducting subsurface profiling of road pavements and underground pipelines in either ground-coupled or air-coupled mode, but the separation distance between GPR antenna and the target is usually less than 0.5 m (20 in.) (Bungey 2004; Daniels 2007; Jol 2009). Other non-contact radar and microwave techniques that can perform remote sensing are for structural testing or displacement monitoring, which cannot perform subsurface inspection or sensing (Shinozuka *et al.* 2000; Pieraccini *et al.* 2004; Bennett and Rutz 2012). In a recent review on the NDT/E methods for concrete bridges, it was reported that only contact GPR techniques can perform subsurface sensing of concrete structures (Rehman *et al.* 2016). In other words, contact or near contact radar/microwave methods (e.g., GPR) are capable of conducting subsurface sensing, while non-contact or remote radar/microwave methods can conduct surface sensing. Only a very few studies on the use of synthetic aperture radar (SAR) imaging for the subsurface sensing of concrete structures.

Rhim and Buyukozturk (2000) reported their concrete imaging work for the detection of concrete delamination and subsurface steel rebars, using three microwave bands. They demonstrated the feasibility of SAR for the subsurface delamination and rebar detection of concrete using laboratory specimens. No quantitative condition assessment criterion was reported in their work.

Li and Narayanan (2006) studied physics based image data fusion techniques by processing the raw data collected from multiple inverse synthetic aperture radar (ISAR) sensors. They derived an appropriate data fusion rule in order to generate a composite image containing increased target shape characteristics for improved target recognition. However, the composite image can be reconstructed using the inverse 2-D Fourier Transform over the separated multiple integration areas. In addition, the algorithm of Matrix Fourier Transform (MFT) can be regarded as an exact interpolation, thus there is

no information loss caused by data fusion. Moreover, they reported that the rotation centers need to be carefully selected in order to properly register the multiple images before performing the image data fusion.

Yu and Buyukozturk (2008) studied the use of ISAR on concrete for subsurface sensing by studying the effects of inspection angle and signal bandwidth, using laboratory FRP (fiber reinforced polymer)-wrapped concrete specimens. They demonstrated that resolution of SAR images can be improved by increased frequency, increased bandwidth, and increased angular range (synthetic aperture).

Bu *et al.* (2010) applied an algorithm for synthetic aperture radar (SAR) imaging based on compressed sensing (CS) theory. A random fractional Fourier transform (FRFT) matrix was used as the sensing matrix. Typically, an imaging with SAR typically requires large bandwidth for collecting and processing. Conventionally, large amounts of the echo data are sampled for achieving high resolution imaging, requiring a long time to collect data. To achieve high resolution SAR imaging with fewer data samples and better efficiency, new approaches are needed. They reported that the CS theory affirms possibility to recover certain signals and images from far fewer samples or measurements than conventional methods use. They cast the problems of SAR into the emerging framework of CS. Their simulations demonstrated that the proposed approach has achieved comparable results with the existing CS-based approaches.

Yu (2011) proposed a method to use SAR imaging for the subsurface damage detection of concrete structures using mathematical morphology and Euler's number. The method utilizes far-field steady-state electromagnetic waves reflected from the surface of multilayer composite systems and generates the in-depth profile of the inspected composite systems using inverse synthetic aperture radar (ISAR) imaging technique. Spatial imagery of the system can be reconstructed with the structural and geometric features of the multilayer system. These features are revealed by discrete scatterers in the imagery. Reconstructed imagery can be used for detecting construction defects and structural damages in the near-surface region of the system. The theoretical background of the method is described, followed by experimental measurements on glass- fiber-reinforced polymer (GFRP)-confined concrete cylinders with an artificial defect as an example of multilayer composite systems. Continuous waves in the frequency range of 8 to 12 GHz were used. The imaging results show that the proposed method can reveal the location and size of the embedded defect in the GFRP-concrete composite system, indicating the potential use of the method as a basis for distant radar/microwave nondestructive testing/evaluation techniques in civil engineering.

Yu *et al.* (2016) combined SAR and laser acoustic sensing for the detection of subsurface delamination in laboratory FRP-wrapped concrete specimens and studied the pros and cons of hybrid NDT. Two different remote nondestructive testing (NDT) techniques, the acoustic-laser and imaging radar techniques, were studied for near-surface defect detection in fiber-reinforced polymer (FRP) retrofitted systems. In the acoustic-laser technique, the targeted structure is excited by acoustic waves, while vibration data on a measurement point is remotely collected. In the imaging radar technique, radar

signals (electromagnetic waves) are remotely emitted toward the target structure and measured when they are reflected from the structure. Three FRP-bonded concrete cylinders with various defect sizes were fabricated for laser and radar measurements. They found that detectability of the imaging radar technique depends on background characteristics (e.g. geometry, material's property), inspection scheme (e.g. angle, distance/range, frequency), and defect characteristics (e.g. size, shape, orientation). In this paper, radar detectability is quantified by a signal-to-noise ratio. In addition, in the SAR images of damaged specimens, scattering radar signals are reconstructed at or near the location of a subsurface/ interfacial defect and used to indicate the presence of the defect. In our experimental SAR imaging result of carbon FRP-concrete specimens, the presence of scattering signals in SAR images indicates the presence of a subsurface anomaly. The amplitude of the scattering signals increases with the increase of anomaly size. The maximum amplitude of the scattering signals also suggests the location of the anomaly. Meanwhile, optimal inspection angle depends on (i) the geometry and size of subsurface anomaly, (ii) surface roughness of the background, and (iii) distribution of dielectric properties in the background and the anomaly (dielectric contrast).

Yu (2016) proposed a novel SAR image transformation approach called K-R-I transform for solving the difficulties in SAR image comparison problem. He proposed a feature extraction algorithm to quantitatively assess the condition of intact and damaged carbon fiber reinforced polymer (CFRP)-wrapped concrete cylinders using synthetic aperture radar (SAR) images. The proposed algorithm converts SAR images into a simplified representation, based on the shape, size, and amplitude of SAR images. In this approach, the shape of scatterers in a SAR image is characterized by average Gaussian curvature (K), area ratio (R), and SAR amplitude (I), and is represented by a K-R-I curve. SAR images of intact and damaged CFRP-wrapped concrete cylinders were generated by a stripmap SAR imaging radar system (10.5 GHz) at various inspection angles (0°, 15°, 25°, 30°, 45°, and 60°). From our experimental result, it is found that the K-R-I representation of SAR images is capable of distinguishing damaged SAR images from intact ones at different inspection angles. Quantitative dissimilarity between the K-R-I curves of intact and damaged specimens is assessed by coefficient of correlation and compared with the signal-to-noise ratio (SNR) of SAR images. It is found that the dissimilarity of K-R-I curves is closely related to the SNR of SAR images, demonstrating the feasibility and potential of the proposed K-R-I representation.

2.2 Digital Image Correlation Sensing

Lecompte *et al.* (2006) investigated crack detection of prestressed concrete beams using DIC and LED-CCD techniques. They used Green-Lagrange strain expression to calculate deformation. Since classical experimental techniques, strain gauge, and extensometers do not provide sufficient illustration to comprehend local damage mechanism, they used full field measurement techniques focused on a given region of interest (ROI) of the target. They used a 17.6-m long prestressed beam specimen in their experiment. Four point bending was performed on the specimen, where the two bending points were decoupled. Four loading unloading cycle were performed where 45, 65, 76, 95 kN respectively were exerted from per jack. In DIC technique, images were taken

every 10 kN loading interval. Subsequently, the displacement and deformation field at the surface of object were calculated on the basis of comparing between images at different loading steps. The image was divided into a number of subsets where the subset size was 7x7, 11x11, or 15x15 pixels. The software determined the displacement values of the centers of the subsets. Their study showed that crack detects appearance and evolution of cracks before the cracks become visually detectable. They reported that DIC can be utilized to accurately locate the crack in the Zone of Interest (ZOI).

Hild *et al.* (2006) proposed an approach to evaluate mode I and II stress intensity factors by combining image correlation and elastic displacement field identification. For brittle materials, crack length and crack opening measurement to quantify the stress intensity factor and toughness. Thus determining crack tip location is a major challenge. They used a sandwich beam to obtain stable crack propagation. The sandwich beam was made of place silicon carbide (SiC) specimen in between two steel beams. Since the crack was complex and dependent on complex geometry and surface friction, they did not use analytical or numerical identification of the stress intensity. Instead, two CCD cameras were used to take 1008x1016 pixels resolution pictures. A 6-nm physical crack was detected in their experiment. Meanwhile, the test results showed that the errors were 2%, 3%, and 10% for 10^{-3}, $5x10^{-4}$, and $2.5x10^{-4}$ strain levels. Finally, using known values of elastic properties of silicon carbide (E = 410 GPa, γ= 0.15), they calculated stress intensity factor by using crack opening displacement. They also claimed that the technique was almost perfectly measure crack opening displacements in perspective of accessing scales were well below light wavelength. It reveals the way to crack identification and even quantify toughness measurement.

Mulle *et al.* (2009) reported the development of a DIC system to experimentally determine surface stress distribution of a composite structure submitted to bending tests. They used a beam type specimen which presents design singularities such as important thicknesses, ply drop off zones and a reinforced zone. They considered the central reinforced zone of the specimen. In order to estimate the strain distribution during a series of 3 and 4-point bending tests, several optical fiber Bragg grating sensors were embedded in various levels of the ply stack. Simultaneously, surface strain field measurements by three dimensional digital image correlations were undertaken. Both techniques showed a general linear distribution of longitudinal strains through the thickness of the thick zone but values are slightly different. A numerical model was developed and a test-calculation dialogue was carried out. The complementary information gathered by the two optical techniques for in-core and surface measurements revealed the importance of considering structural and edge effects.

Chen *et al.* (2010) proposed a two-step extended digital image correlation (X-DIC) method to directly quantify full field displacement with discontinuities by using partition of unity method as extended finite element method (X-FEM). In the first step, approximate displacement of target was measured. Newton-Rephson method (iterative process) was later utilized to approach the specific displacement value. To validate the method, they performed two tests; the rigid body translation test and uniaxial tensile test. A flat plate with artificial speckle was used to perform rigid body translation test. In this test, a three dimensional adjustable shelf pushed the specimen 20 μm to horizontal direction. Couple of CCD camera was used to take DIC pictures. The original digital

image size was 512x512 pixels. Displacement was measured in 19x19 pixels subset. Their average test result was identical to theoretical measurements. An aluminum test specimen was used to conduct vertical and horizontal displacement of uniaxial tension. The electronic universal testing machine was used to exert necessary loads. One image from 100 N load was compared with 1500 N image. 11x11 to 19x19 pixels subset was used to determine displacement. The result was close to theoretical value, and also had a great deal of agreement with following principle: a uniaxial tensile load, the horizontal displacements of all points in a vertical line has the same value, and vertical displacements of all points in a vertical line are linear in distribution. A 40.1x270x11 mm^3 specimen with two cracks on each side was loaded by an electronic universal testing machine to measure the deformation across crack domain. Couple of CCD camera captured image when applied load were 31 N and 266 N. It revealed from experimental result that the displacement of both vertical and horizontal direction were discontinuous. They found that increase of vertical displacement across to crack is more effective than horizontal displacement.

Kamaya *et al.* (2011) reported a procedure to determine true stress-strain curves and to measure post-necking strain. They used hourglass type specimens made of carbon steel plate for welding structures. Three specimens with different notch radius (10mm, 5mm, and 2mm) and a minimum diameter of 6mm were used in their tension tests. They carried out tension tests in a laboratory environment with room temperature. Loading rate was fixed at 0.2mm per minutes. A pair of 5M-pixel CCD cameras was used to determine nominal strain distribution and local displacement. The specimens were dot painted to implement digital image correlation technique. They performed finite element analysis (FEA) using ABAQUS to model a quarter of the specimen and demonstrated that simulated result agrees with experimental result.

Destrebecq *et al.* (2011) studied crack detection and measurement technique to measure beam deflection and curvature of a full scale reinforced concrete beam after 25 years of service in severe industrial environment by using digital image correlation (DIC) technique. Test specimen was 7,840 mm long, and cross sectional area was 160x450 mm^2. Mechanical properties of concrete were found from a standard cylinder compression test, cored out from another companion beam. A residual deflection was determined to be approximately 2.6 mm. A region of interest (ROI) with 718x102 mm^2 in the tension zone was chosen to use DIC technique. The ROI was divided into 10x10 pixels zone of interest (ZOI). They used a 2D image correlation system with 12 bits dynamic camera (by Philips). The CCD camera had 1,024x1,024 pixels. Moreover, an LVDT sensor was installed at the mid span to measure beam deflection. The specimen was tested in four points bending with a 7,000 mm effective span. They used five-cycle loading, and the beam was crashed in the last cycle. By processing the image taken by DIC system, displacement values were acquired by one ZOI line only. Longitudinal displacement discontinuity revealed appearance of crack, the vertical amplitude of discontinuity correlates crack opening. They also observed that the cracks did not completely close upon unloading, due to the interlocking mechanism of aggregates. From the theoretical calculation of crack opening, they observed that crack opening rate is much lower than expected in pure bending. The appearance of a longitudinal compressive force in the beam was assumed to be responsible for the delay. They also demonstrated that DIC technique is suitable for early crack detection and measurements.

Meanwhile, their DIC measurement was generally in good agreement with LVDT measurement and suitable for in-situ damage detection.

Wu *et al.* (2011) studied the properties of the fracture process zone (FPZ) in concrete using DIC. Their study correlated FPZ length with load and specimen parameters. In their experiment, they investigated six concrete specimens with different sizes and notch depths. A universal testing machine exerted 0.005 mm/min loading rate on specimens during testing. A clip gauge installed at the center of the notch to measure the crack mouth opening displacement (CMOD). A camera was placed 1.5 m apart perpendicular to the test specimen to capture images every second until the total failure of the specimen, the image was processed by post-processing device. 1,024x768 pixels resolution was adopted. They concluded that DIC measurement to obtain development and length of FPZ is reasonably accurate.

2.3 Unmanned Aerial Vehicles for Infrastructure Inspection

Unmanned aerial vehicles (UAVs) or unmanned airborne systems (UASs) are widely used in military, civilian, scientific, and commercial applications around the world. Engineers have discovered a wide range of civilian applications for these airborne, mobile vehicles, including farming, wildfire fighting, law enforcement, counter-terrorism, environmental monitoring, georeferencing, surveying search-and-rescue operations, traffic surveillance, construction safety surveillance, seismic risk assessment, and infrastructure inspection. In general, UAVs represent an economical approach compared with other ground approaches.

Existing UAV applications require different specifications and features of the vehicle. Some of the most important features considered a UAV for a particular purpose include size, type, maneuverability, range, endurance, payload capacity, equipment needs and wind resistance, are elaborated in the following.

- **Type**: For civilian UAV systems, two types of UAV are used; rotary wing and fixed wing. Rotary wing UAV is a VTOL-aircraft (Vertical Take Off and Landing) that can hover over any target and can take off and land without any runway. Fixed wing UAV cannot hover and needs a runway or a launcher to launch, but it typically has more endurance than a rotary wing UAV.
- **Payload**: Depending on the design of UAV, the payload of UAVs is typically in the range of 0.5 – 15 kg (in 2017). This has important implications on the type of sensors and other accessories that the UAV can carry.
- **Flight speed**: Rotary wing UAV typically has slower speed than the one of fixed wing UAV. Rotary wing UAV can fly in the speed range of 0~40 miles per hour (mph). Civilian fixed wing UAV can fly in the speed range of 10~50 mph, while military fixed wing UAV can achieve higher speeds.
- **Endurance**: UAVs vary greatly in endurance, ranging from 10 minutes to 12 hours (in 2017). For the same vehicle, the payload greatly influences the endurance. Larger payloads result in shorter endurance. Vibrant wind environments also lead to shorter endurance. Endurance is certainly affected by

the sensors used onboard of UAV when the sensors share same power source with the UAV platform.

- **Power source**: Currently, there are two power sources for civilian UAV, fuel-based and battery-based. Fuel-based UAV has longer endurance but is less safe while the battery-based UAV has shorter endurance with better safety. Recently, many researchers have been working on using solar energy to power UAVs. For instance, Shiau *et al.* (2009) proposed a solar power management system (SPMS) consisting of maximum power point tracking (MPPT), battery management, and power conversion stages, which provide the power required for on-board electronic systems. Power source has important implications on endurance and risks. It is foreseeable that sustainable power solutions of UAV will rely on the use of alternative energy sources (e.g., solar).
- **Flight altitude**: Existing UAVs have large variations in terms of flight altitude. The maximal flight altitude of most civilian UAVs ranges from 300 m to 1,000 m. For applications in need of a large bird's-eye view of target, a UAV system with higher altitudes should be required.
- **Wind resistance/stability/controllability**: Small-size UAV typically shows lower wind resistance against strong wind and gust (e.g., large than 7 m/s or 15 mph). But it varies depending on the control algorithm of individual UAV systems. This has very important implications for the risk factors. Wind resistance/stability/controllability of UAV affects the quality of collected images and videos when using optical sensors on UAV, as well as the signal-to-noise ratio (SNR) when using other sensors. Better wind resistance can be achieve with advanced control algorithms, but endurance may be sacrificed
- **Level of autonomy**: Most of commercially available UAV systems require full human supervision (zero autonomy) or full manual operation. Autonomous UAV systems are typically designed relying on the availability of GPS signals, suggesting the requirement of an open, outdoor environment. Waypoint GPS navigation technology is usually used in achieving full autonomy of UAV.
- **Sensing capability**: Different applications require different sensors, such as spectral cameras with different bands, LiDAR, and gas sensors (for measuring air quality). Some UAVs are equipped with simple integrations of different sensors while others are not. The selection of sensors depends largely on the specifications (e.g., payload, speed) of UAV and the applications.
- **Size**: For most applications, size of UAV is not a major concern unless it affects the payload, endurance, and wind resistance/stability of UAV. However, size can be a constraint for infrastructure sensing and monitoring. For example, detailed inspection of steel and concrete bridge diaphragms prevents large UAV from accessing the limited space between bridge girders for steel corrosion and concrete cracking detection.
- **Cost**: Currently, the cost of commercially available UAV systems ranges from less than $100 USD to $4,000 USD (in 2007). Prices are different by the specifications of UAV, mainly payload, endurance, and level of autonomy. A cost-effectiveness analysis of UAV is suggested per application.

The abovementioned features can be used as design criteria for designing/selecting a UAV platform for a given application or problem. A ranking system can be developed of the applicability and cost-effectiveness of the UAV technologies for different transportation applications based on application needs. Table 1 compares selected civilian UAV systems commercially available in the market.

Table 1. Comparison of selected commercial UAV systems

	Type	Payload (kg)	Flight speed (mph)	Endurance (min)	Power source	Flight altitude (m)	Wind resistance	Sensors	Dim. (cm)	Weight (kg)
Aibotix A6 V2	4M	2	18	30	Battery	1,000	Yes	GPS, thermal image, DSLR camera, multispectral	105 x 105 x 45	3.4
Aerobot ES20-10	2M					60.96		GPS		
Skycamusa	6M			10	Battery	1,000	10 mph	GPS		
MD4-200	4M	0.2	18	30	Battery	1,000		GPS	54 x 54	1.1
MD4-1000	4M	1.2	27	88	Battery	4,000		GPS	103 x 103	2.65
MD4-3000	4M	3.0	36	45	Battery	1,000		GPS	103 x 103	10.4
SteadiDrone QU4D X	4M	8.0		60	Battery		Strong winds	GPS	91 x 91 x 47.5	3.58
SteadiDrone QU4D	4M	0.8		60	Battery		Strong winds	GPS, GoPro 3+	61.5 x 61.5 x 16.5	1.5
SteadiDrone MAVRIK	4M	2.0		18	Battery		Strong winds	GPS	77.7 x 50 x 20.5	2.2
PARC	4M			720	AC/DC	3,048		GPS, Night Vision		
Draganflyer X4-ES	4M	0.8	4.5		Battery	2,438.4		GPS	87 x 87 x 29	
Draganflyer X4-C	4M	0.335	4.5		Battery	2,438.4		GPS	59.5 x 59.5 x 25.5	
Draganflyer X4-P	4M	0.8	4.5		Battery	2,438.4		GPS	87 x 87 x 30	
Draganflyer X6	6M	0.335	4.5		Battery	2,438.4		GPS	90 x 84 x 26.5	
Draganflyer Guardian	4M	0.42	4.5		Battery	2,438.4		GPS	59.5 x 59.5 x 25.5	
Trimble UX5	FW		50	50	Battery	2,500	40 mph	GPS	100 x 65 x 10	2.5
Trimble X100	FW		50	45	Battery	2,500	40 mph	GPS	100 x 65 x 10	2.2

Hammer *et al.* (2007) reported an approach to deblur UAV aerial images (blind deconvolution) for civil structures inspections using Mumford-Shah/Total Variation (MSTV) regularization. In their approach, detection of defects from the images did not depend of the sensor type applied to obtain the images. Rather, ability to detect defects on

structures depended on image quality, which is sensitive to internal parameters of the UAV (vibrations modes, video exposure times, etc.) and to external parameters (turbulence, bad illumination of the scene, etc.). A UAV was used to inspect a bridge in western France. Four cases were considered in his experiment. The first case was a noise-free synthetic image (blurred by a kernel which is the convolution of an out-of-focus blur) to simulate surface cracks of various sizes. The second case was a satellite image in which the MSTV obtained a clearer image and better reconstruction of some details. In the third experiment, they simulated a real noisy image by using the same degraded satellite image, but this time, affected by Gaussian noise. The MSTV showed better robustness to noise again. Finally, in the fourth experiment, a real image from a UAV was considered. While zooming in on detailed parts of the bridge, blurring of the images occurred leading to the purely "blind" context on the shape and size of the subject. Image clarity was improved using their method, at the cost of losing image contrast.

Metni and Hamel (2007) discussed the aerodynamics of UAV for structural monitoring structures and bridge maintenance. They presented a control strategy for autonomous flight with orientation limits in order to keep the target within the camera's view. Their strategy only required a measurable system with a video camera for planar surface, with a limitation that the UAV's orientation at small angles. They used an X4-flyer UAV capable of quasi-stationary flights to locate defects and cracks on bridges. They also identified three different existing methods of visual servoing: i) 3D position-based visual servoing, ii) 2D image based visual servoing, and iii) 2½D combining visual features obtained directly from the image and features expressed in the Euclidean space. In their approach, visual data were obtained via projection of real world images onto the camera image surface. The coordinates of the same point in a body-fixed frame and the world frame were related in order to produce projective mapping or homograph matrix. Finally, a simulation test was conducted with a helicopter to inspect defects on bridges by means of a mounted video camera. In their field test, video images were used to bridge inspection and condition assessment.

Hallermann and Morgenthal (2014) developed a UAV system using airborne photos and video for bridge inspection in semi-autonomous mode. They used a wind resistant (up to 12 m/s or 27 mph) UAV with mounted camera and GPS to acquire digital images and videos to reduce the time spent and technicality required for bridge inspection using conventional methods. The UAV used (AscTec Falcon 8) (see Fig. 5) was an octorotor (with eight rotors) which are arranged on two arms in a V-shape configuration. It has a standard payload of 650 g, an endurance of up to 18 minutes (with a standard payload) and resistant to magnetic fields. The modified camera mount enabled a horizontal angular freedom of 360^{o} and a camera tilt angle on 90^{o} (up and down). A major issue of the method was found to be the blurring of the images due to strong winds. In their simulation, the camera was displaced vertically about 1 m and horizontally by 2.25 m. A probability distribution was created to investigate the effects of the continuous movement of the camera. For bridge inspection, they used GPS navigation software (Way Point Navigation System) and a pre-planned matrix-based flight plan for very high or long span bridges, or a flight feature referred to as Point of Interest (POI) that allows the vehicle to fly around a structure at a constant distance.

Fig. 5. Flight system Falcon UAV system with mounted digital camera Sony NEX 5 and additional camera Panasonic Lumix and mobile ground station (Hallermann and Morgenthal 2014)

They also presented how they applied image and video data obtained from the UAV to detect displacements on a retaining wall. After camera calibration, some changes were applied on the wall by removing and later replacing some bricks to simulate displacement on the retaining wall. The same pre-planned flight of the UAV was conducted both before and after the change. The photos were processed to form 3D-point clouds with the help of the georefrenced control points. They concluded by noting that further research is required on the analysis of detection quality based on computer vision algorithm, which could be possible by using Probability of Detection.

Hößler and Landgraf (2014) developed a measuring system to detect overtaking vehicles. The measuring system consisted of a UAV called HORUS (Hovering Remote-Controlled Ultra-light Sensor) and a high-resolution camera. The H-shape of the UAV allowed different arrangements of payloads and power solutions. The UAV-based measuring process was almost completely automated. HORUS was equipped with a camera gimbal that stabilized the camera angle while UAV changes pitch and/or roll. The camera used a fisheye lens with a 120^{o} view angle. In determining the global coordinates of aerial images of the recorded vehicles, an automated image processing algorithm was proposed. The ability of the measuring system to detect overtaking maneuvers was proven by the analysis of more than 600 recorded image sequences. From their result, the monitoring system HORUS can be applied to investigate intersection-related accidents.

Sumitro *et al.* (2013) mounted a high-definition camera, a DIC sensor, and a GPS system onto a UAV platform and used the system for bridge inspection and SHM. This SHM system was applied to Oshiba cable-stayed bridge (built in 1997). A Crack-width Recognition System (CRS) was developed to automatically interpret crack width from the recorded images by a 3D laser scanner, Gigapixel Imaging System (GPIS) and the UAV system to calculate the crack index (CI) of the bridge. The contrast and brightness of concrete surface were found to be important and affected the qualify of CI calculation. For better crack-width interpretation, they found that it is necessary to investigate the

effect of grey level and image resolution. Fig. 6 shows an application example of their UAV system.

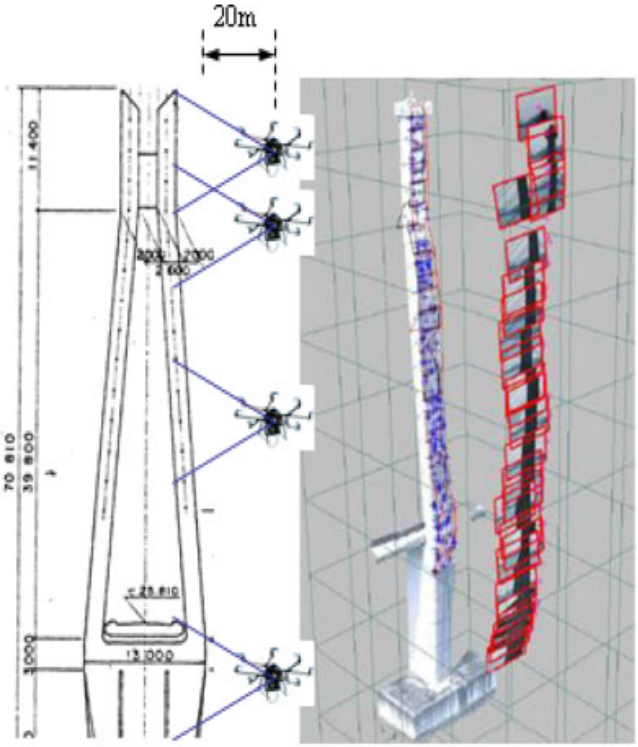

Fig. 6. UAV measurement scheme (Sumitro *et al.* 2013)

CyPhy Works, Inc. (2014) and Georgia Institute of Technology developed a UAV system for inspection and monitoring of civil infrastructures like bridges and dams. Their UAV system applied paradigms in the civil infrastructure domain: Robotic Assisted Inspection (RAI) and Autonomous Robotic Monitoring (ARM). In their design, RAI enabled inspectors to perform consistent, repeatable, thorough, frequent, fully documented inspections, which will in turn lead to more effective prioritization of maintenance and repairs. RAI was meant to expedite bridge inspections because it does not require the setup of snooper trucks or climbing harnesses and will save money by eliminating direct costs associated with bridge inspections, as well as the indirect costs incurred (lane closures) and safety of inspectors. On the other hand, ARM represented a different approach to be an installed, in-situ civil infrastructure monitoring system. ARM was used to monitor civil infrastructure without the need for an inspector onsite.

The PARC system (see Fig. 7) consists of a Ground Control Station (GCS) and a quadrotor VTOL air vehicle. The PARC vehicle carries a gyro-stabilized, gimbal mounted, EO/IR camera payload. In addition to the camera system, PARC has additional payload capacity for communications devices. If additional payload capacity is required, the camera payload can be removed. The PARC system can operate at altitudes of up to 1,000 feet above ground level, or 11,000 feet density altitude.

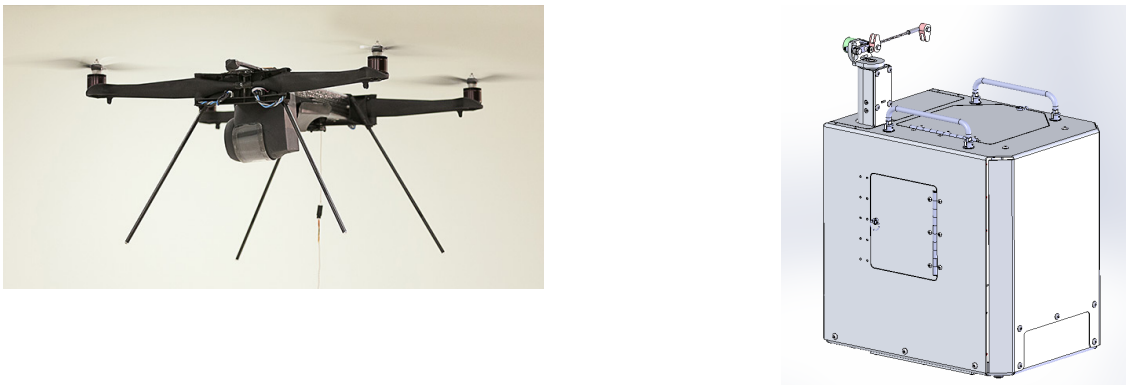

(a) (b)

Fig. 7. PARC (a) Surrogate vehicle and (b) microfilament management (ChyPhy Works 2014)

In 2014, Florida DOT was working with Florida Institute of Technology on a project entitled **"**Proof of Concept for Using Unmanned Aerial Vehicles for High Mast Pole and Bridge Inspections" in order to cut down the time and cost spent on inspecting Florida's approximately 7000 bridges and 4,300 HMLs (high mast luminous or lights). Their approach was to collect the necessary images of the structures and tag them with the UAV's GPS for image processing (Avendano *et al.* 2013).

In addition to ChyPhy Works' PARC system, there are also many companies developing UAV for infrastructure inspection, such as Draganflyers X4-P (by Draganfly Innovations) for inspecting bridges, joint sealants, scaffoldings and cranes. At the present time (in 2017), the market for infrastructure inspection is global and is extensively developing and evolving. Inventors and entrepreneurs are constantly releasing new UAV products for specialized applications ranging from traffic surveillance to surface crack mapping of critical civil infrastructure around the world. Nonetheless, there is no reported UAV system capable of performing subsurface sensing of concrete structures using SAR imaging.

Chapter 3. Development of An Airborne Imaging Radar Sensor

In this chapter, design and manufacturing of an airborne imaging radar sensor is introduced.

3.1 Design Concept

To be used on UAV, the airborne imaging radar must be able to acquire radar signals continuously. It is not possible to have UAS go-stop-go with the accurate and stationary positions like other ground scanning systems using stationary positioners. Our first step is to evaluate the current imaging radar system and explore its UAV portability. This step includes assessing the performance of radar at continuous mode in data acquisition speed and developing tradeoffs between radar speed and radar detectable range.

The acquisition speed of each signal is generally determined by radar frequency sweep time, data transfer time through serial port, and the overhead time for communication between personal computer (PC) and the control board. According to the specification of the radar controlling board, each frequency sweep can be completed in ~75 ms for 1,500 frequency points. The frequency sweep data are transferred to PC at the Baud rate of 115,200 bits/second. As an example of 1,500 frequency points, the data format for each frequency point is a string of 11 ASCII characters, plus an additional terminal character. The minimum time for data transfer is 1,500x12x8/115,200 = 1.25 seconds. Fig. 8 shows an experiment with 200 continuous signal acquisitions. With 1,500 frequency points for each acquisition, the actual average acquisition time is 1.61 seconds, which includes frequency sweep time, data transfer time, and communication overhead between PC and radar control board.

Decreasing frequency points can speed up the signal acquisition, but it will reduce the detectable range. As displaced in Fig. 9, the average acquisition time drops to 0.63 second for 501 frequency points. Table 2 lists the tradeoffs between signal acquisition time and detectable range for different frequency points. In real applications, one can choose optimized parameters according to the specific acquisition speed and detectable range requirements.

Based on the current hardware limitation of radar controller, we may have a minimum of 0.63 seconds latency due to the system acquisition and system re-initiation. In order to mitigate the performance impacts. We have to propose two different solutions (1) flight compensation algorithm and (2) new control board with no gap latency.

(1) Flight compensation algorithm: First solution is to design a flight algorithm to fly through the target area multiple times but with the different start and stop points with designed offsets. We also need to record the each mission flight time. We have to use linear estimation to fill the data matrix of the interest target area.

(2) Control board: After we review the control board from our radar board vendor, we found the reason for gap latency is due to its 16bit ADC. The only way to improve the latency is to redesign a control board. At this point, we may need to seek for the software solution first. The fully control board will cost time and additional budget.

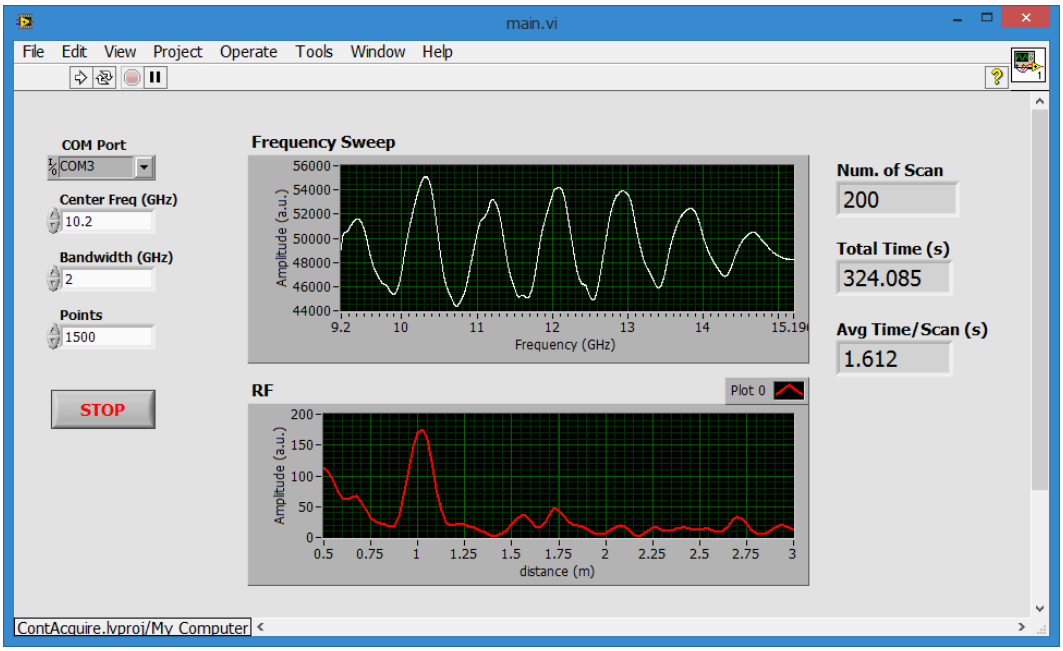

Fig. 8. 200 continuous signal acquisitions. A metallic target was placed 1m from the opening of the horn antenna.

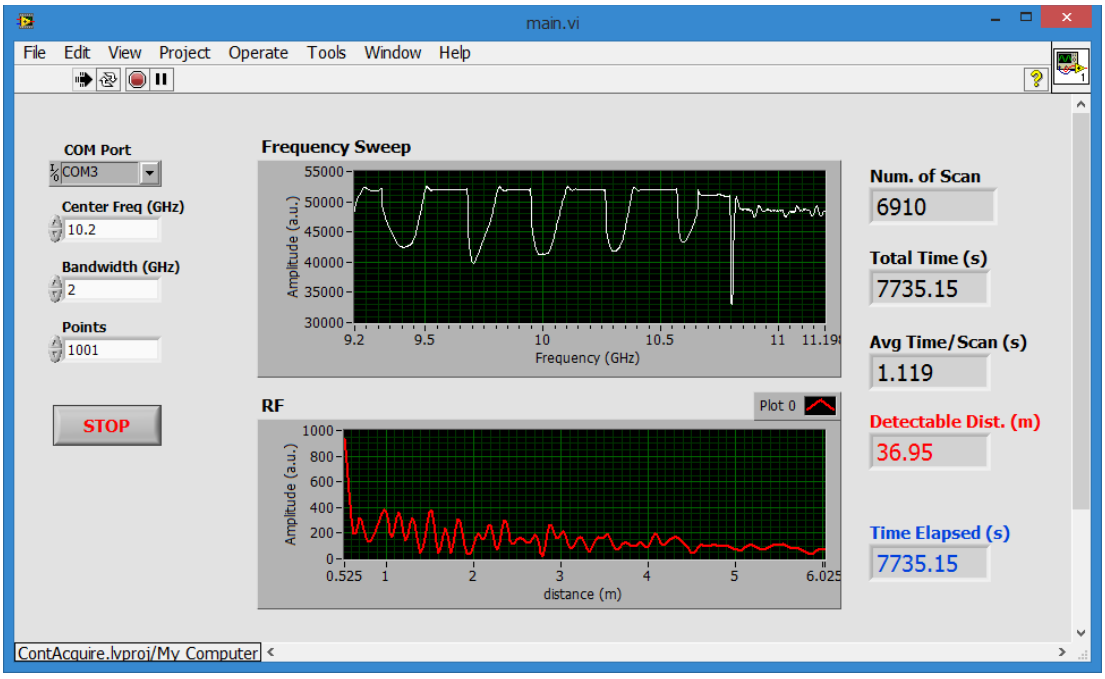

Fig. 9. Attenuated radar signal amplitude when voltage is low

Table 2. Dependency of frequency points on signal acquisition speed and the detectable range

Frequency Points	Acquisition Time, T_a (s)	Detectable Range (m)
1,500	1.61	56
1,200	1.31	44
1,000	1.12	37
750	0.87	28
500	0.63	18

Flight speed Assumption

If we want to move UAV along X-axis with a speed V m/s, the sampling separation is equal to $d=V*T_a$. If we can set average flight speed V = 4/40 s = 0.1 m/s. d = 0.1*0.63 = 0.063 m = 6.3 cm. Our SAR separation is determined by 0.5 wavelength of TX frequency and the lab system which is around 2.5 cm. Apparently, we have to either decrease the UAV speed or reduce the frequency points.

3.2 Power Design

We use a 12V battery pack and design a power management system with PCB for the UAV system. The power consumption for the actual system will determine the battery pack weight. We limit the total battery weight under 0.5lb as the design goal, also expecting that it may exceed the design goal if the flight time and power consumption become greater than expected values. The total weight of battery pack is between 200g to 250g, with limited system endurance.

A pack of four batteries, instead of an AC-DC converter, is used for powering the radar and its controller for continuously acquiring radar signals. After the batteries are fully charged and connected to the radar load, the output of battery is 16.1V and the output of voltage regulator for radar system is 11.8V, as shown in Fig. 10.

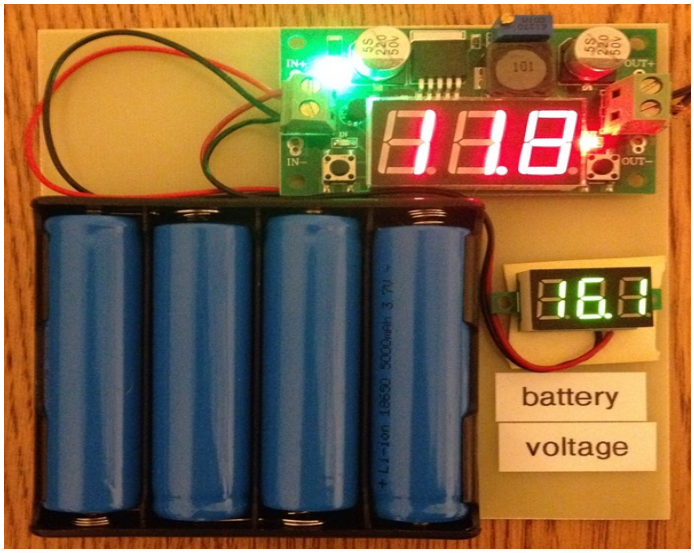

Fig. 10. Battery voltage and regulator output after continuously running for one hour

Table 3. Battery voltage and regulator output vs. running time

Running Time (mins.)	Battery Voltage (V)	Regulator Output Voltage (V)
0	16.2	11.8
30	15.5	11.8
60	15.3	11.8
90	14.9	11.8
120	13.2	11.2
123	11.8	10.5
125	11.1	9.8
127	9.8	8.5
128	8.6	7.3

After 120 minutes of operation, the regulator voltage starts to drop, consequently the radar frequency sweep signal starts to flat out at the end (Fig. 8). After 128 minutes, the output of regulator drops to 7.3V, and the radar signal experiences a severe attenuation (Fig. 9). These tests are important for us to understand the power consumption of imaging radar in order to choose an appropriate power solution.

On the sensor battery system design, we use a 12V battery pack and designed a power management system with PCB in the current version. The power consumption for the actual system determines the battery pack weight. We limit the total battery system weight under 0.5lb but it is possible that the final weight may exceed 0.5lb if the flight time and power consumption are more than expected. In summary,

- The total weight of battery pack is adjustable between 200g and 250g. Tradeoffs are system endurance and payload.
- The battery can sustain more than 60 mins when fully charged.

3.3 Radar Control Board Design

The control board for radar and UAV communications is selected to be MinnowBoard Max. From the MinnowBoard development guide, the board can be operated with a minimum current of 2.1A to 2.4A. We move the MinnowBoard from the original planned packing with radar to inside of UAV. Summary of the radar control board design is listed in the following.

- Review connection options (Most likely is USB 2.0 ad connect to RS 232)
- Memory is 32GB SD CARD
- Operation time is under review with portable power bank selection (Max 2.1A)
- Power consumption 2400mA 500mA (USB2) + 900mA (USB3) + 500mA (core) + 500mA (other peripherals) = 2400mA.

Regarding the control board testing with the radar board, we move all our control and signal processing ability from a laptop computer installed with LabView to the MinnowBoard. We connect the board with an AC/DC adapter, as shown in Fig. 11.

A C++ control program, as displayed in Fig. 12, is developed to continuously acquiring the frequency scanning data of the radar system. It records the data from the board and saves the date to a USB flash memory. Fig. 12 demonstrates our ability to control the board without using a laptop computer.

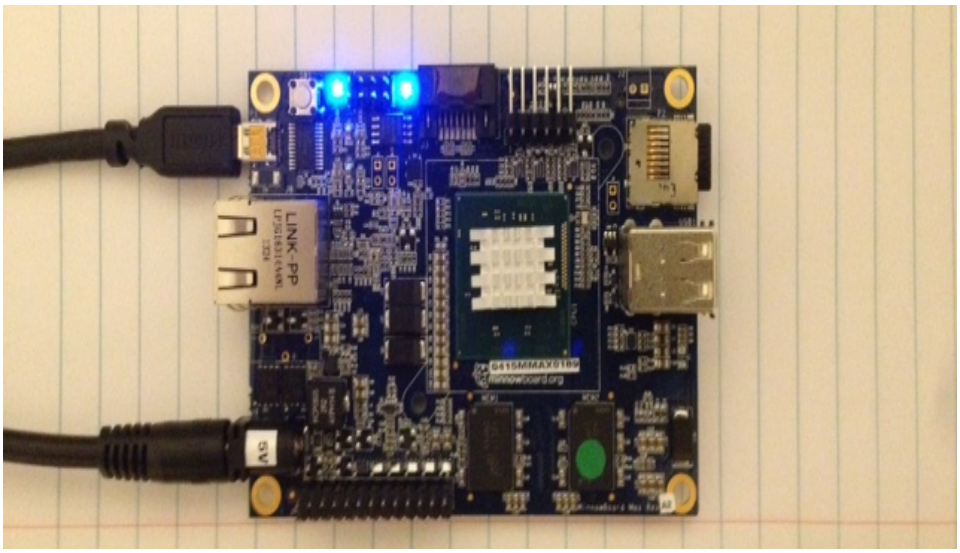

Fig. 11. MinnowBoard system

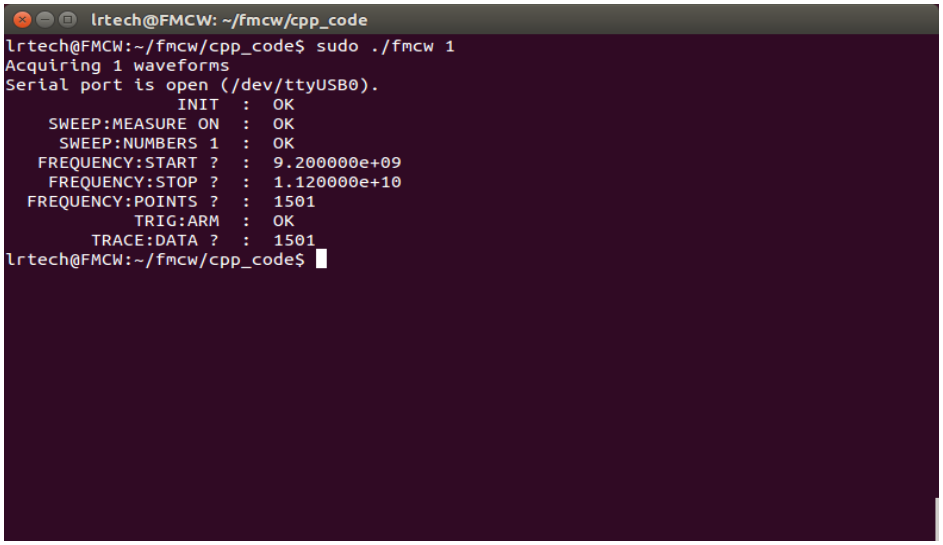

Fig. 12. A screen shot of performing frequency scan using C++ language

The simple setup to connect everything without a laptop computer is shown in Fig. 13. There is an additional USB hub in the setup since we have to use a mouse and a keyboard to program the C++ code into the board with a temporary computer screen. Those accessories will not be necessary in our final design.

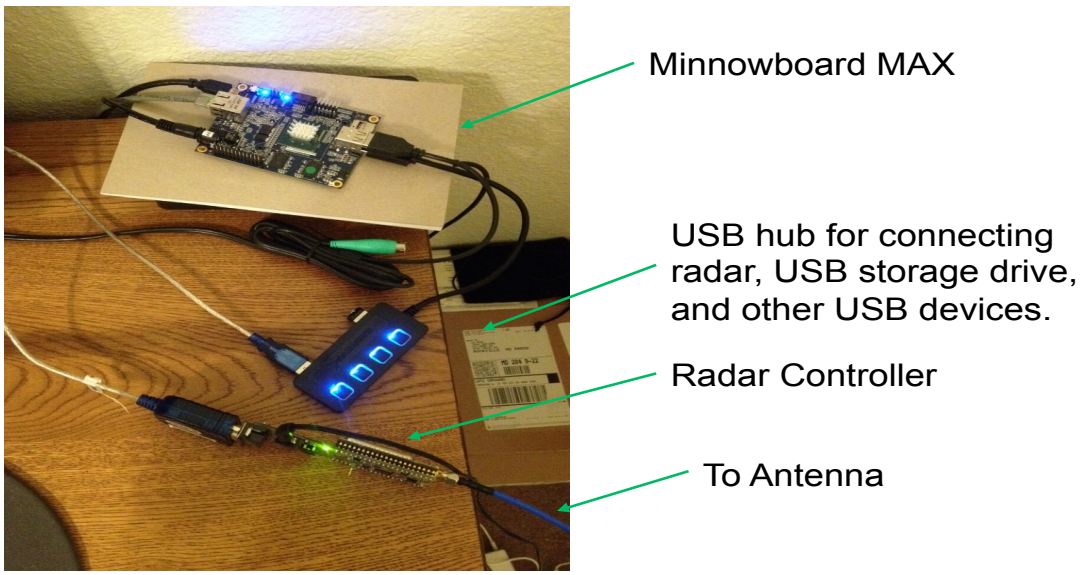

Fig. 13. Battery voltage and regulator output after 1 hour continuously running

We use this setup to detect the same reference target in the same distance as we used LabView to control the radar. We also compare the signal quality and detection results from different setups. It shows that the radar signals have no changes (see Fig. 14). This assures us that we should expect no performance degradations from an embedded control system.

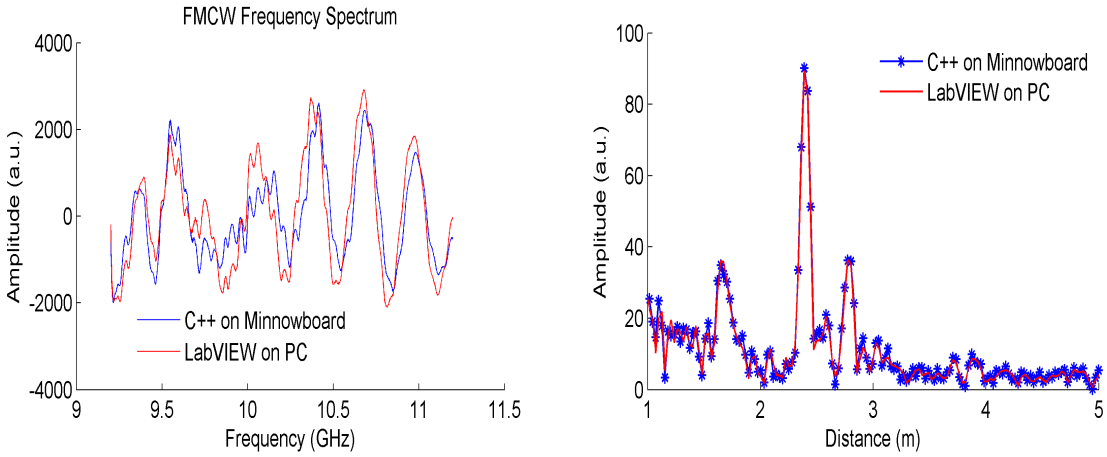

Waveform from frequency sweeps Processed RF waveform

Fig. 14. Comparison of target signals at 2.4 meters away from the radar antenna

The initial concept for the UAV and radar control is shown in Fig. 15. Performance specifications of this control are summarized in the following.

- Controlling API is necessary for autopilot.
- Determine Command & Control (C2) flow: Ground Station ←→ Our enclosure on UAV ←→ Radar and UAV flight control

- A Ground Station with GUI is needed. The radio access path between the UAV platform and the ground station is needed.
- The sensing feature enables the continuous operation of the radar with a non-stop moving platform.

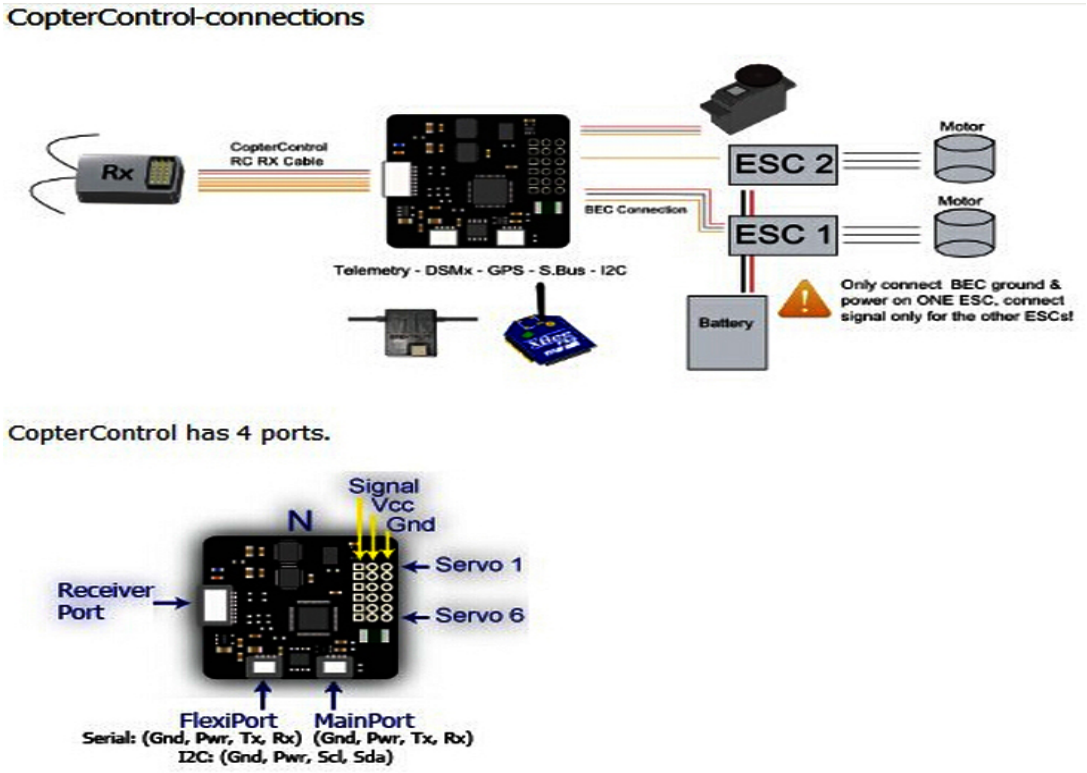

Fig. 15. UAV-radar control concept and design

3.4 Enclosure Design

Our enclosure volume and weight estimation design include the following features:

- The size of enclosure must fit into 5x5.5x2 in^3 payload volume.
- The enclosure includes the radar board, the MinnowBoard, power and data cables, and one 12V battery system.
- Interface: SMA, power plug, USB
- Total enclosure weight: 2.58 lb.

To protect the enclosure and the radar antenna, a commercial grade case is necessary for transport. Fig. 16 shows the imaging radar sensor and its casing design. A modular adaptor is also developed for assembling the CivilEye+Radar system.

Finally, Fig. 17 shows the final design of the airborne imaging radar sensor. This imaging radar sensor can be self-powered or powered by the UAV's battery system. Since it is equipped with a wireless module, radar signals can be transmitted to an adjacent laptop computer when performing field measurements.

Fig. 16. Imaging radar sensor and its case

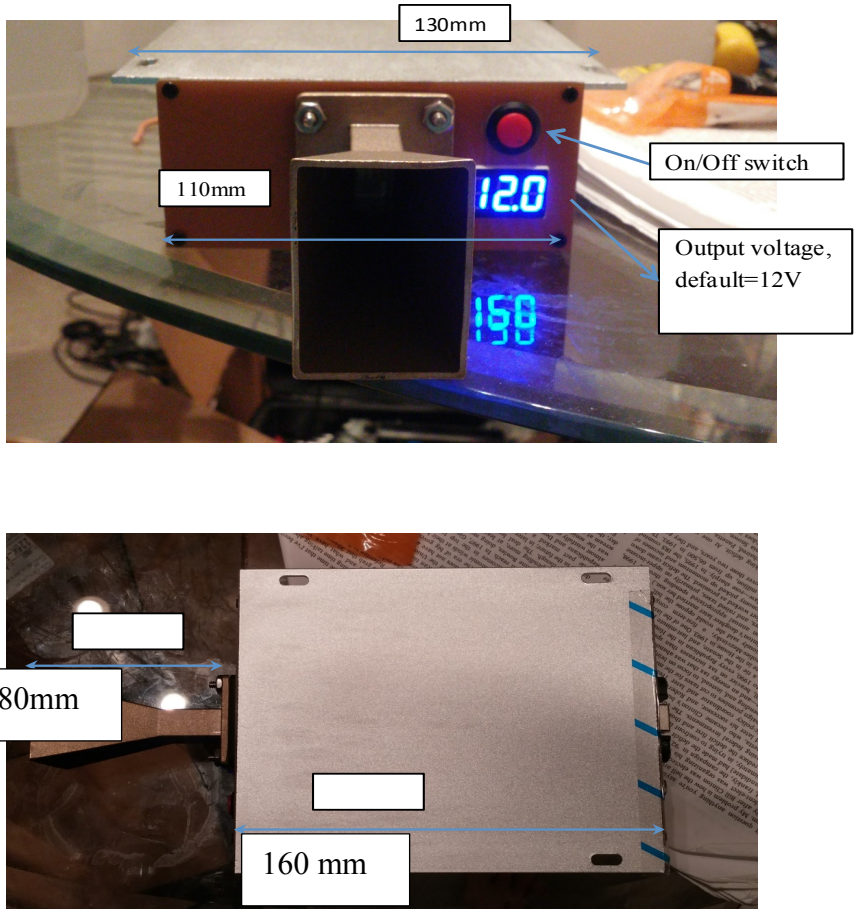

Fig. 17. Casing design of the CivilEye system

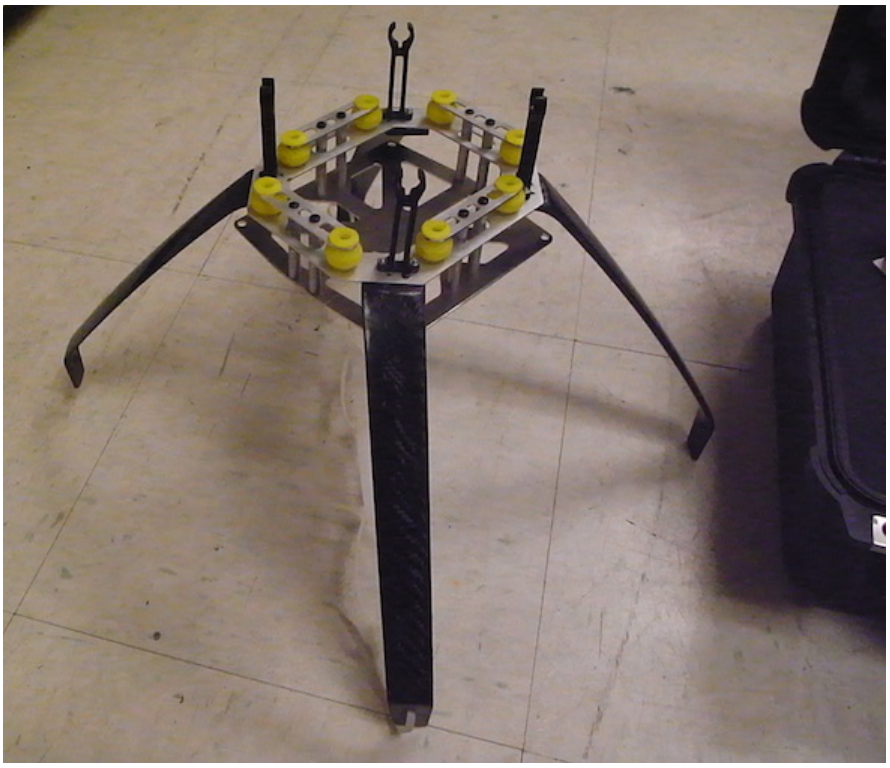

Fig. 18. Modular adaptor for the CivilEye+Radar system

Chapter 4. Development of an Airborne DIC Sensor

In this chapter, design and manufacturing of an airborne DIC sensor is introduced.

4.1 Fabrication of Camera Bar and Camera Selection

One component of creating the sensing payload is to identify the appropriate cameras and design a camera bar to help perform DIC measurement. We have investigated different camera options and identified requirements for both DIC system and the UAV platform, as listed in Table 4.

Table 4: Primary camera requirements for DIC and UAV systems

DIC system requirements	*UAV requirements*
-Monochrome sensor -Large sensor size -Fixed position lens -synchronized trigger -5Mp or greater for 1m FOV	-Low Profile to reduce drag forces -Low weight for reduced power consumption (<3lbs.) -5V output through controller board

There is a large market for industrial monochrome cameras that are designed to be integrated into test fixtures, assembly lines, microscopes and many for fixed position applications. These cameras possess the high quality sensor requirements of a DIC system and are intended to be small, light and easy to integrate. The Meridian MSX-160M is potential candidate for this project that is currently being explored (see Fig. 19). The final camera selection should be made by considering cost/price, weight, sensitivity, resolution, data transfer, etc. The performance specifications for the Meridian MSX-160M are shown in Table 5.

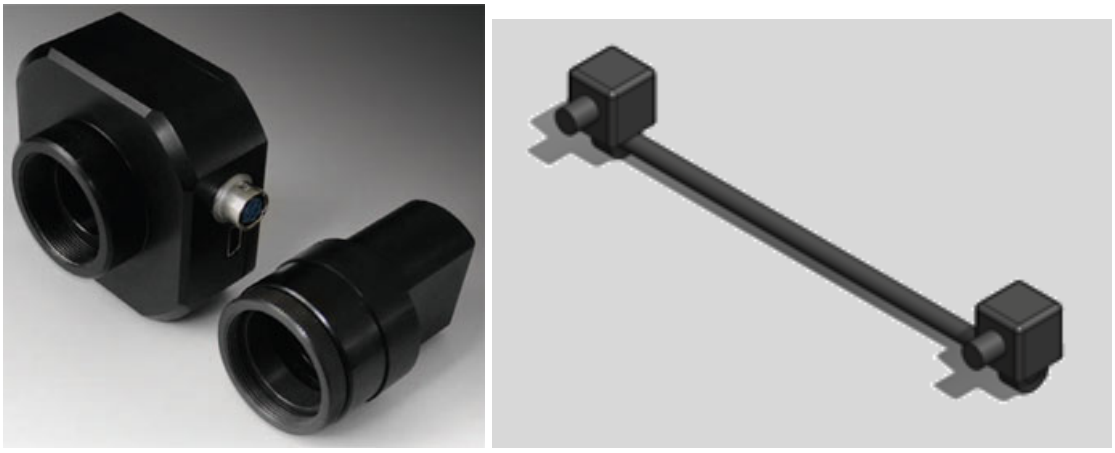

(a) Meridian SMX-160M **(b)** Camera bar design concept

Fig. 19. Meridan cameras and the camera bar design concept

Table 5: Meridian SMX-160M - Key Specifications

Meridian MSX-160M
-6.6Mp - 2208 x 3000 -3.5µm pixel size -USB 2.0 + external trigger port -Monochrome sensor - 10bpp -Supply current 360 mA at 5.0V -3.5oz w/o lens -Includes basic software that can run on Linux OS

Another important design constraint is the camera separation. The cameras relative position needs to be fixed with respect to each other. The camera Bar will have a circular cross-section to allow the cameras to pivot upward the take vertical measurements. Exact dimensions are to be determined. The team is currently analyzing the material selection (e.g. carbon fiber, titanium, aluminum, etc.) and comparing the benefits of each.

After evaluating multiple camera options the UML team has tested the Basler acA1600-20um and acA1600-20gm industrial monochrome cameras (see Fig. 20 and Table 6 for specifications). The cameras contain Sony ACX274 sensors but will each utilize a different port on the MinnowBoard MAX development board. One will be controlled through USB 3.0 and the other through Gigabit Ethernet (GigE). This unique setup allows the full utilization of both high throughput ports and saves the weight of a USB or GigE splitter.

Fig. 20. Basler acA1600-20um(Left) and acA1600-20gm(Right)

Table 6. Basler acA1600 series - Key Specifications

Basler acA1600-20um/gm
-2.0Mp – 1626 x 1236 -4.4µm pixel size -6oz (pair) -Monochrome sensor - 12bpp -Global Shutter -C-mount lenses

Lenses were purchased with the intention of having a working distance and field of view close to that of the radar unit. An 8.5-mm focal length lens at a designated working distance of 1-1.5m will produce a field of view of 835mm and 1256mm, respectively.

Compact lenses with locking focus and aperture have been successfully used in camera experiments thus far. The acquired components for the camera system are specified in Table 7 and together have a total weight of 0.8lbs. With the additional hardware and camera bar, the complete DIC system weighs less than 1.5 lbs.

Table 7. Camera System Weight Update

Item	Weight [oz.]
1x aca1600-20gm	3.20
1x aca1600-20um	2.80
2x 8.5mm lens	3.80
1x MinnowBoard Max	2.12
1x USB cable 0.3m	0.34
1x GigE cable 0.3m	0.34
1x 6-pin hirose(power) 0.3m	0.17
Total Weight	**12.7 oz. - 0.8 lbs.**

Calibration of the stereo camera pair is validated by taking several pictures of the target object prior to inducing stresses/strains. Theoretically the stress/strain for each measurement will be zero but there will always be some level of noise in the system. The strain measured from the stationary system is referred to as the noise floor for the measurement and is a general indicator of the minimum value that can be measured with the DIC system. Fig. 21 shows a test fixture capable of displacing the upper patterned plate in 0.01mm increments along a lead screw attached to a dial indicator. The areas highlighted in green are the surfaces recognized by the DIC software as the area of interest and are recalculated at each image stage. The location of white on black optical targets are also recalculated for at each stage with the purpose of defining a local coordinate system with an x-axis always parallel to the axis of translation.

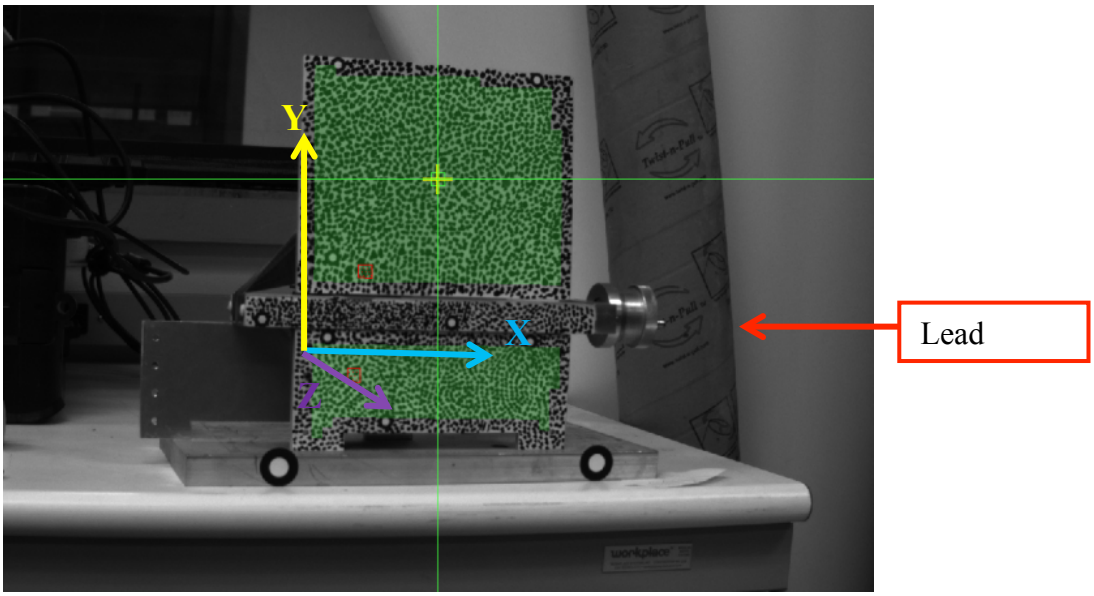

Fig. 21. Experiment structure (Left) and measured noise floor (Right)

The bar and camera mounts are designed to position the cameras to have a working distance of 1.75m from the target surface. This distance was determined to optimize radar performance. Fig. 22 shows the schematic of our camera bar design.

Fig. 22. Schematic of the camera pair with the bar and mounting brackets

During the design phase numerical models were run to estimate the resonant frequencies of the camera bar assembly when attached to the UAV. Part of the design criteria is to ensure that the assembly does not have a resonance within the operating frequency range of the UAV's rotors. In the current configuration, the closest resonance to the UAV's operating range occurs at a frequency of approximately 64.5 Hz [3872.7 RPM]. The most recent estimate of the UAV's operating rotor speed is 4500-6500 RPM. Fig. 23 shows the result of dynamic analysis.

A second enclosure is fabricated at UML to attach a MinnowBoard with an mPCIe expansion board for WiFi connectivity to the camera bar assembly. We use this assembly to conduct laboratory and on-site experiments in preparation for in-flight tests. A third enclosure is designed to attach the camera assembly and a MinnowBoard to the UAV in the event that the radar unit is temporarily unavailable. Fig. 24 illustrates our hardware design.

The estimated weight of the camera system needs to be revised with the updated bar length and camera mounts every time changes to any component are made. Consequently, total weight needs to be updated, as well as the resonant frequency. Table 8 shows the updated system weight. The design process for the integrated systems like the CivilEye system is similar to the one for airplanes.

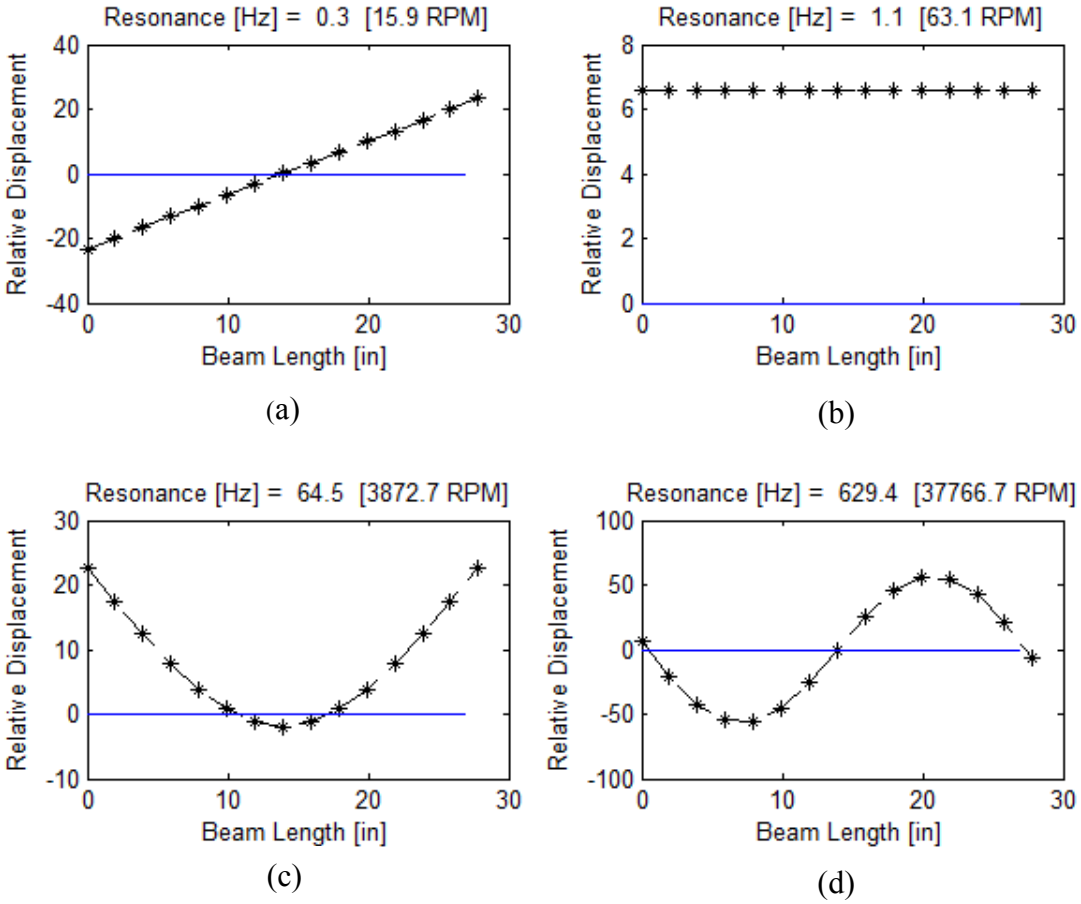

Fig. 23. Rigid body modes (a) & (b) and first and second bendıng modes (c) & (d) of camera bar assembly

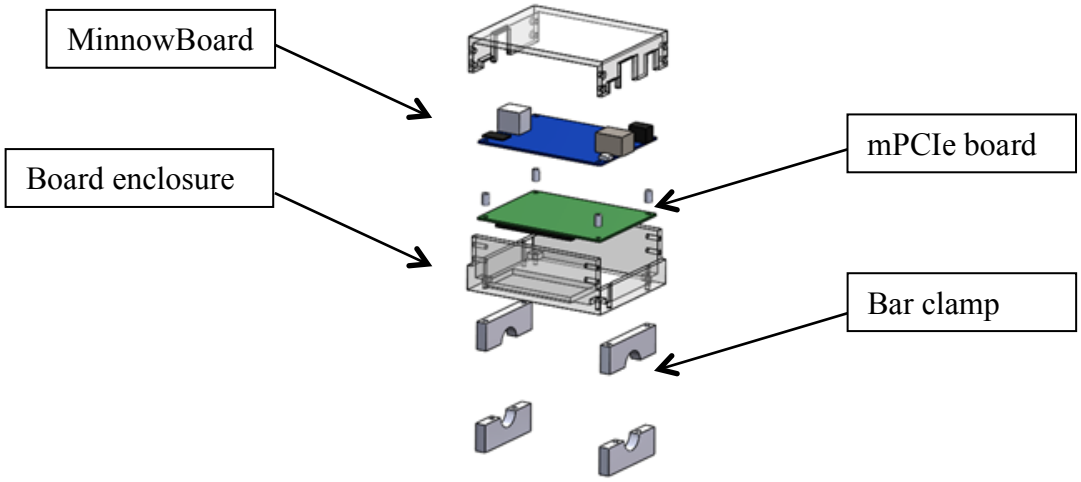

Fig. 24. Exploded view of the standalone DIC system controller hardware

Table 8. Camera System Weight Estimate Update

Item	Weight [oz.]
1x aca1600-20um	2.8
1x aca1600-20gm	3.2
2x 8.5mm lens	3.8
1x 0.7m bar	6.46
6x camera mount fasteners	1.26
2x camera mounts	0.24
1x USB 3.0 cable 0.3m	0.34
1x GigE cable 0.3m	0.34
1x hirose cable 0.7m (triggering)	0.17
Total Weight	18.72 **oz. [1.17 lbs.]**

The final design of an airborne, standalone DIC sensor is manufactured and shown in Fig. 25. The off-UAV prototype contains its own battery pack and can be operated remotely from any computer running Microsoft Windows 7 and with Wi-Fi capabilities. Upon completion of the UAV payload enclosure the camera bar assembly and controller hardware are carried over to the payload assembly and the system draws power from the UAV's battery pack. Integrated CivilEye+DIC system is shown in Fig. 26.

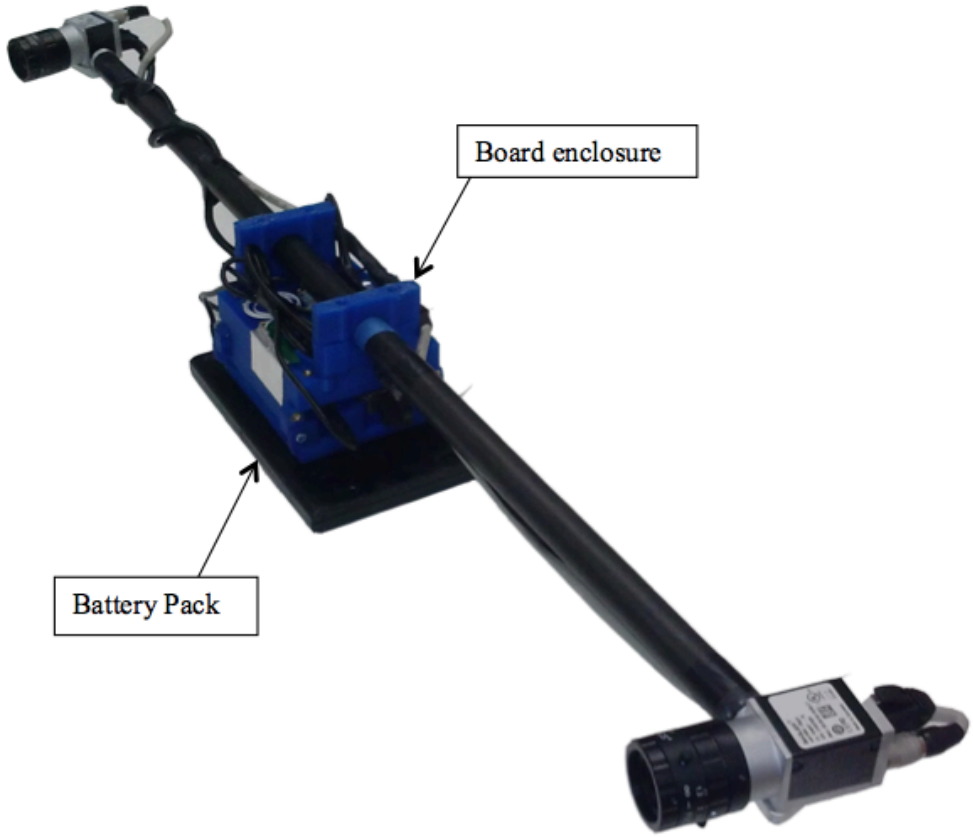

Fig. 25. Standalone DIC image acquisition prototype

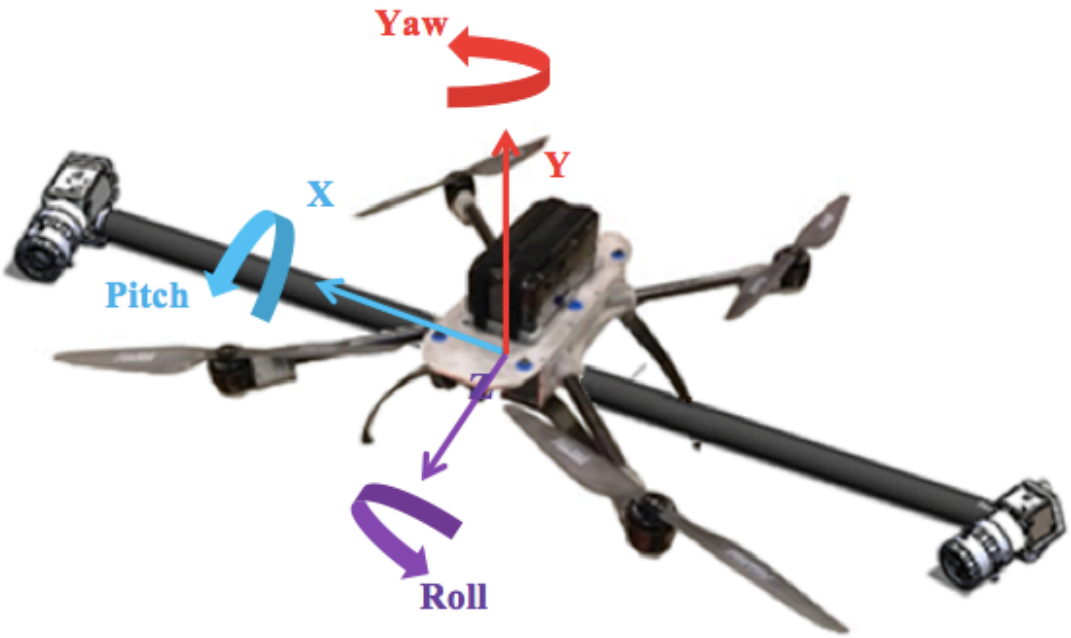

Fig. 26. Integrated CivilEye+DIC system with its local coordinate system

4.2 Onboard Image Triggering and Storage

Synchronization and triggering or the cameras has been successful, along with camera calibration in GOM TRITOP and displacement measurements ARAMIS DIC software. The next step is to optimize the software for the MinnowBoard MAX. Experiments are performed to further determine ways to improve the system for outdoor and unstable environments. As we know, target patterning, lighting, lenses, and working distance can affect the quality of each DIC measurement.

To improve reliability and ease of use, a physical triggering circuit has been implemented between the two cameras. In this configuration sensor parameters can be adjusted and synchronized images can be acquired and saved within the Basler Pylon Viewer application. The Linux version of this application is installed on the MinnowBoard and can currently be accessed remotely from any WiFi enabled Windows workstation. Fig. 27 shows a screen shot of this application.

In the final stage of DIC sensor, we have successfully integrated the DIC sensor with the UAV platform (PSI's Gen4 prototype) as shown in Fig. 28. The payload is designed to be removed and attached as a single unit and without the use of additional tools. Power for the DIC sensor is supplied from the UAV's onboard battery pack. An indoor flight test was performed (see Fig. 29) and noise floor measurements were taken of a pre-patterned foam board to ensure all systems were functioning properly.

The noise floor results for the in-flight measurement are shown in Fig. 30. The measurement results show a displacement range of (-) 0.222 to (+) 0.411 mm. These values are expected to improve as the parameters for the UAV's stabilization control loop are optimized for the inertia of the DIC payload and measurements are made closer to the center of the calibrated measurement volume.

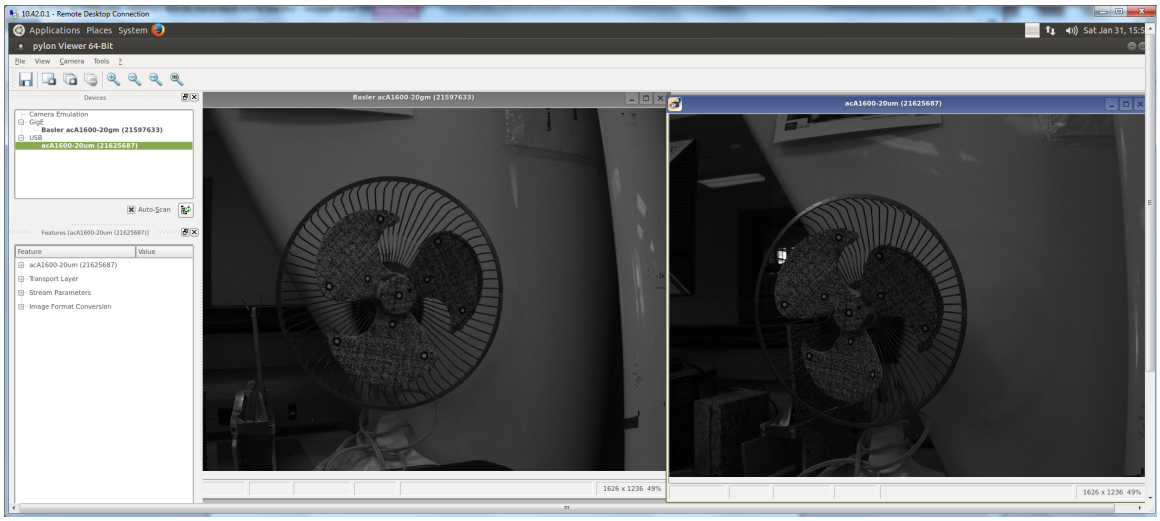

Fig. 27. Basler Pylon Viewer image acquisition GUI

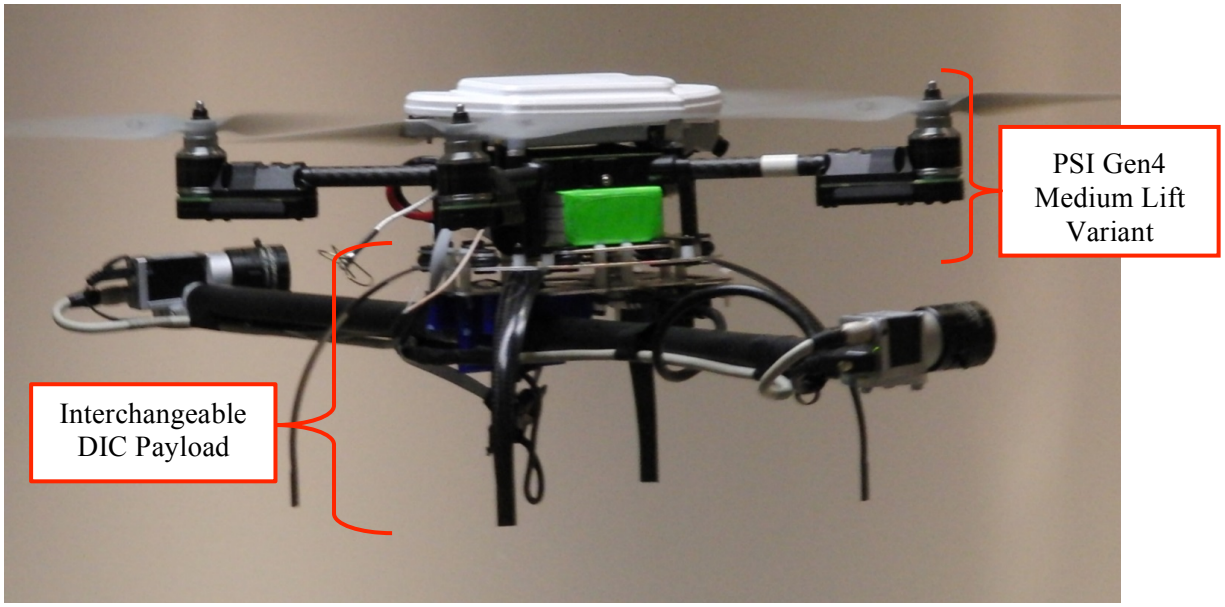

Fig. 28. Hovering CivilEye+DIC system

Fig. 29. CivilEye+DIC system performing in-flight DIC measurements

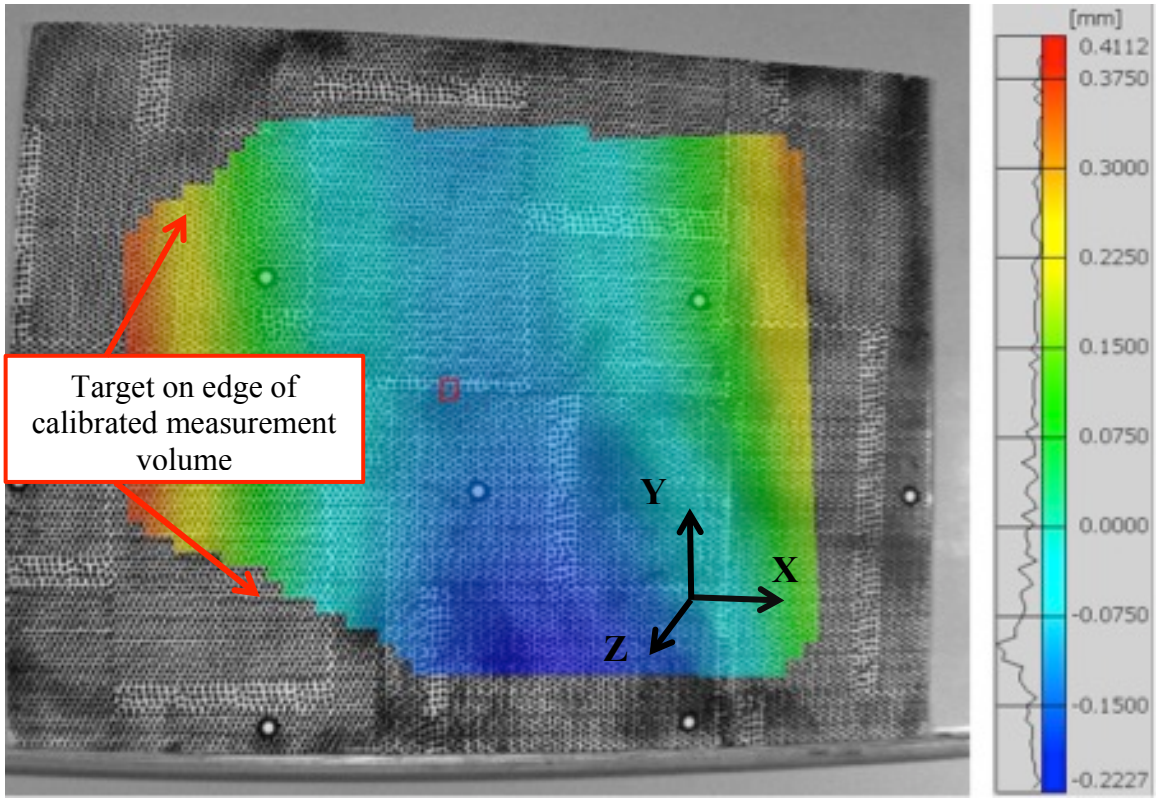

Fig. 30. X-axis displacement noise floor from in-flight DIC measurement

4.3 Benchmark DIC performance to existing certified systems & Perform laboratory test/trials

Several noise floor measurements have been made on Bridge site L-15-002 Plain St. over CSX Railroad. These Measurements were made using the DIC sensor in its

handheld configuration. Fig. 31 calls out the locations of the patterned areas with results for areas C-D displayed in Figs. 32-34, respectively. The noise floor limits for each area are shown in Table 9.

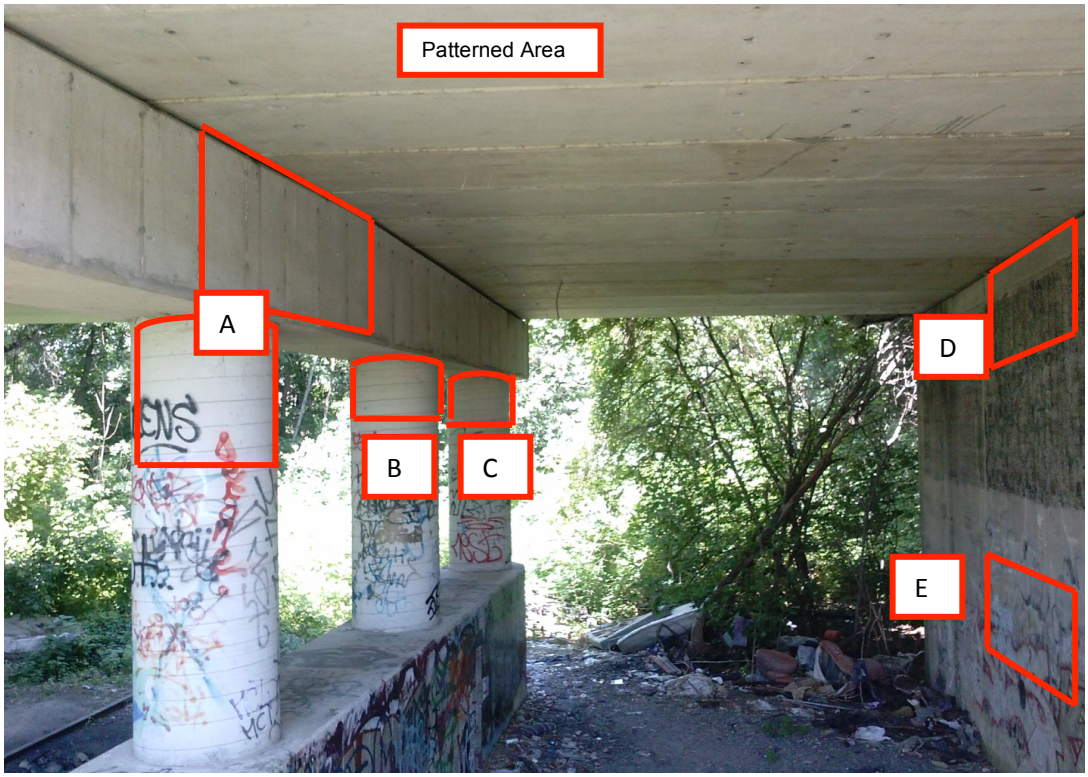

Fig. 31. Patterned locations of L-15-002 Plain St. over CSX Railroad

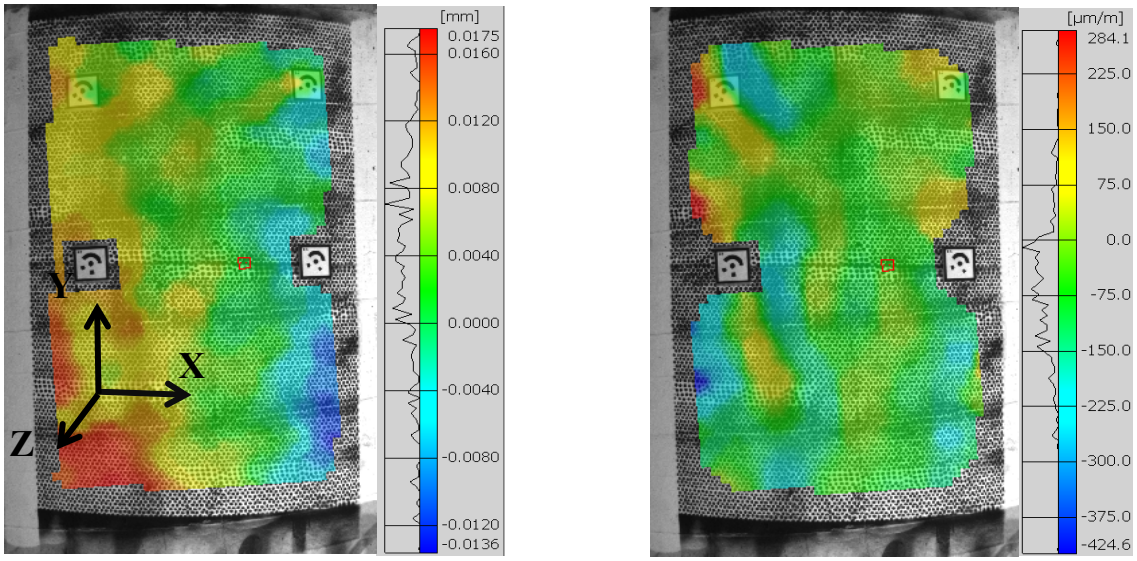

Fig. 32. X-axis displacement (left) and strain (right) noise floor from baseline DIC field measurement; Area [B]

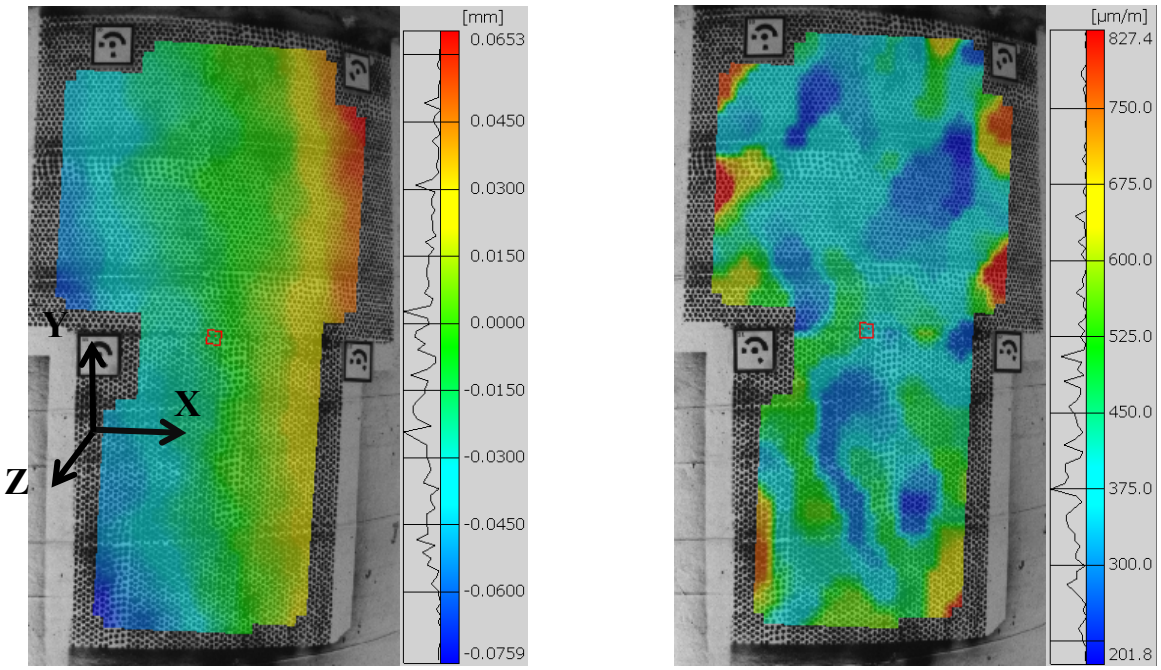

Fig. 33. X-axis displacement (left) and strain (right) noise floor from baseline DIC field measurement; Area [C]

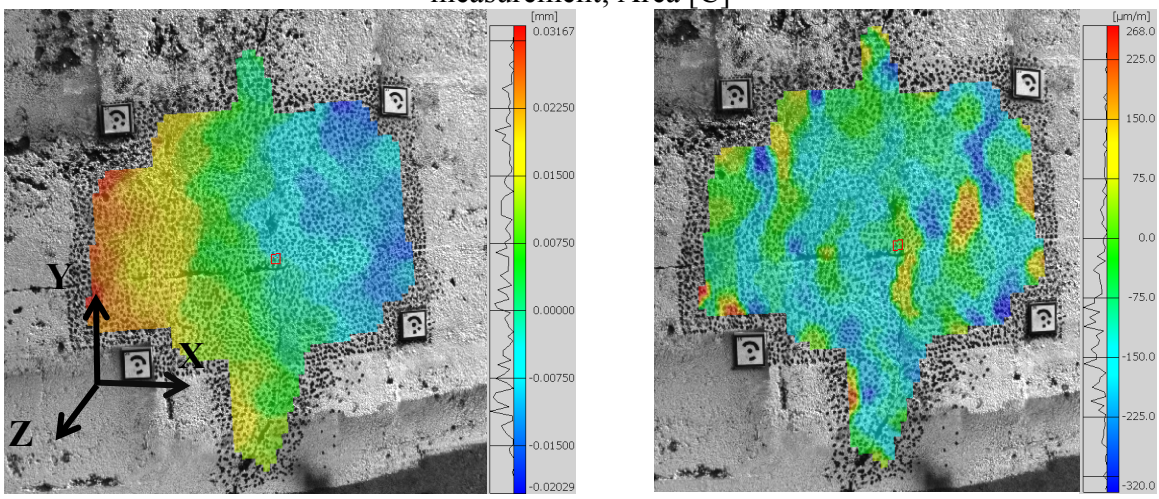

Fig. 34. X-axis displacement (left) and strain (right) noise floor from baseline DIC field measurement; Area [E]

Table 9. Noise floor limits from handheld field measurements

Measured Area	Displacement X [mm]	Epsilon X [µm/m]
B	+0.0175/-0.0136	+284/-424
C	+0.0653/-0.0759	+827/-201
D	+0.0316/-0.0202	+268/-320

Chapter 5. Development of UAV platform and system integration

This chapter reports our accomplishments on the development of UAV platform and system integration.

5.1 Development of UAV motion prediction models

To develop a UAV platform, the motion of UAV must be investigated in order to achieve autonomous operation. We start with the derivation of an efficient coverage path planning algorithm for this particular application. The path planning algorithm generates a reference trajectory that guarantees the optimal inspection of a surface area from the aerial vehicle. The path planning algorithm has to be dynamic by taking into account the real time value of the UAV's battery life. This value determines the End Of Mission (EOM) time that is critical for the safe return of the UAV. The algorithm should also be parameterized by the UAV's velocity.

In our design, the generated path has a snake trail form. The UAV's battery life may not be sufficient for the coverage of an entire surface. Therefore, the path planner must calculate an optimal sub-area that the vehicle can efficiently cover and safely return to the base. The final objective is the implementation of the path planner to the actual vehicle. The path planning algorithm will be integrated to the flight control system. The design objective is for the algorithm to calculate optimal coverage paths in real time and to generate the reference trajectory that the UAV should track accurately.

Milestones in this development are highlighted to demonstrate our design strategy.

1. Quadcopter dynamics (MATLAB simulator): Develop a MATLAB simulator with a visualization module. The simulator will be used for the preliminary validation of the path planner
2. Quadcopter controller: Design a realistic feedback control law that will drive the vehicle.
3. Review different path planning algorithms for coverage
4. Use the simulator to validate the coverage algorithms.
5. Robustify the path planning algorithms in the presence of the external disturbances such as wind gusts.
6. Include the power level's (battery life or endurance) and velocity constraints to optimize the path planning algorithm.
7. Implement the path planning algorithm to the actual vehicle.

To better understand the quadcopter dynamics of UAV, we use a simulation environment to validate the path planning algorithm. This step requires the implementation of the vehicle's Equation of Motion (EoM) to Matlab's SIMULINK environment. The quadcopter is a nonholonomic, nonlinear system with significant dynamic coupling. The vehicle operates in a 3D workspace, thus, six Degrees OF Freedom (DOF) are required to determine its position and orientation in space. Therefore, twelve state equations are needed to determine its motion. The equations of motion map the net external forces (f^B) and moments (m^B) applied to the UAV with respect to the

body frame. The outputs of the systems should be the orientation angles (roll-ϕ, pitch-θ and yaw-ψ) and the position of the vehicle $p^I = [p_n \quad p_e \quad p_d]^T$ in the inertial frame (use the NED convention). There should be four interconnected S-Function blocks, each representing the following group of equations:

$$\dot{\omega}^B = J^{-1}[-\omega^B \times (J\omega^B) + m^B]$$
$$\dot{v}^B = -\omega^B \times v^B + (1/m)f^B$$
$$\dot{\Phi} = \Psi(\phi, \theta, \psi) \cdot \omega^B$$
$$\dot{p}^I = R_B^I(\phi, \theta, \psi)v^B$$

where $\Theta = [\phi \quad \theta \quad \psi]^T$ and

$$\Psi(\phi, \theta, \psi) = \begin{bmatrix} 1 & \sin\phi \cdot \tan\theta & \cos\phi \cdot \tan\theta \\ 0 & \cos\phi & -\sin\phi \\ 0 & \frac{\sin\phi}{\cos\theta} & \frac{\cos\phi}{\cos\theta} \end{bmatrix}$$

$$R_B^I(\phi, \theta, \psi) = \begin{bmatrix} C_\theta C_\psi & S_\phi S_\theta C_\psi - C_\phi S_\psi & C_\phi S_\theta C_\psi + S_\phi S_\psi \\ C_\theta S_\psi & S_\phi S_\theta S_\psi + C_\phi C_\psi & C_\phi S_\theta S_\psi - S_\phi C_\psi \\ -S_\theta & S_\phi C_\theta & C_\phi C_\theta \end{bmatrix}$$

After the UAV's EoM are implemented, the next design step involves the determination of a feedback control law that will autonomously drive the vehicle. In particular, one has to determine the net external forces (f^B) and moments (m^B) as a function of the vehicle's position and orientation such that the latter will fly autonomously. A rendering of the simulation environment can be seen in Fig. 35. The position of the vehicle in the inertial world frame with respect to time can be seen in Fig. 36.

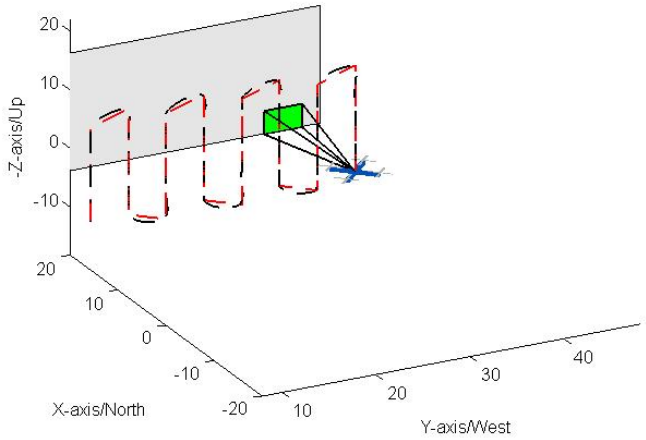

Fig. 35. Visualized environment developed in Simulink for predicting UAV motion. The bridge section under inspection is represented by the light gray area. The quadcopter's reference trajectory is denoted by the red dashed line. The actual trajectory is denoted by the black dashed line. The green rectangular represent the area that is inspected by the onboard sensors.

The preliminary path planner of Fig. 35 is also known as boustrophedon cellular decomposition. The word ‘‘boustrophedon’’ comes from ancient Greek, and literally means ‘‘the way of the ox’’, signifying the pattern in which an ox drags a plow back and forth. The boustrophedon decomposition is similar to the trapezoidal decomposition, but it only considers vertices where a vertical segment can be extended both above and below the vertex.

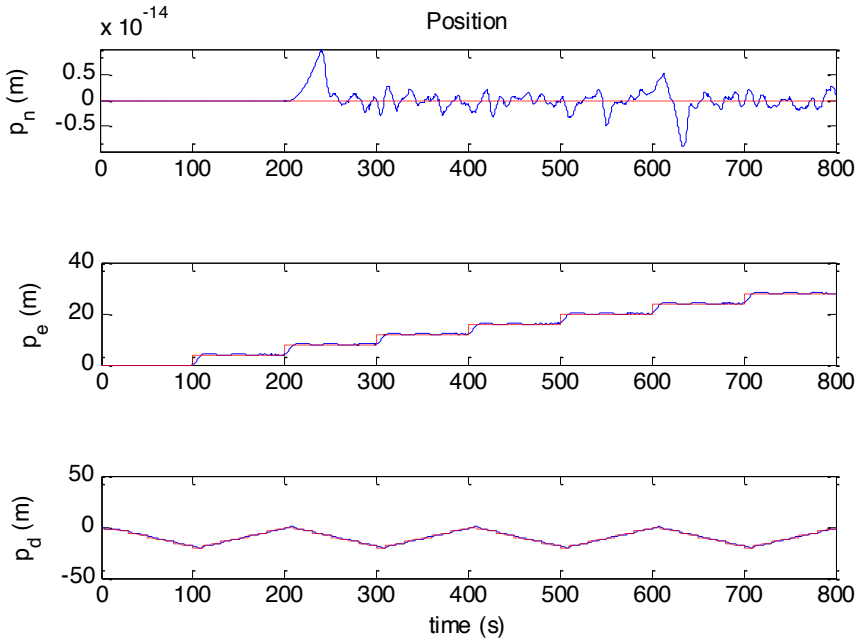

Fig. 36. This figure illustrates the reference (red dashed line) and the actual (blue solid position) position of the vehicle.

To design a realistic feedback control law for the UAV, validation of the localization algorithm developed to estimate the location of the vehicle at GPS denied environments by using two distinct measurement models is needed. When the GPS signal is available, the vehicle uses the position measurement of GPS. If GPS signal is not available, first the vehicle searches a landmark to localize itself. If a landmark is not visible by the front camera, the localization algorithm is relayed to a feature detection estimation module. This module derives position estimates based on the velocity of the vehicle. This localization algorithm is verified with both dense and sparse landmark configuration on the wall. In the dense landmark configuration, landmarks are located on the wall by two meters away from each other on both vertical and horizontal axes. Likewise, in the sparse landmark configuration, they are located on the wall six meters away from each other on the vertical axis and four meters on the horizontal axis.

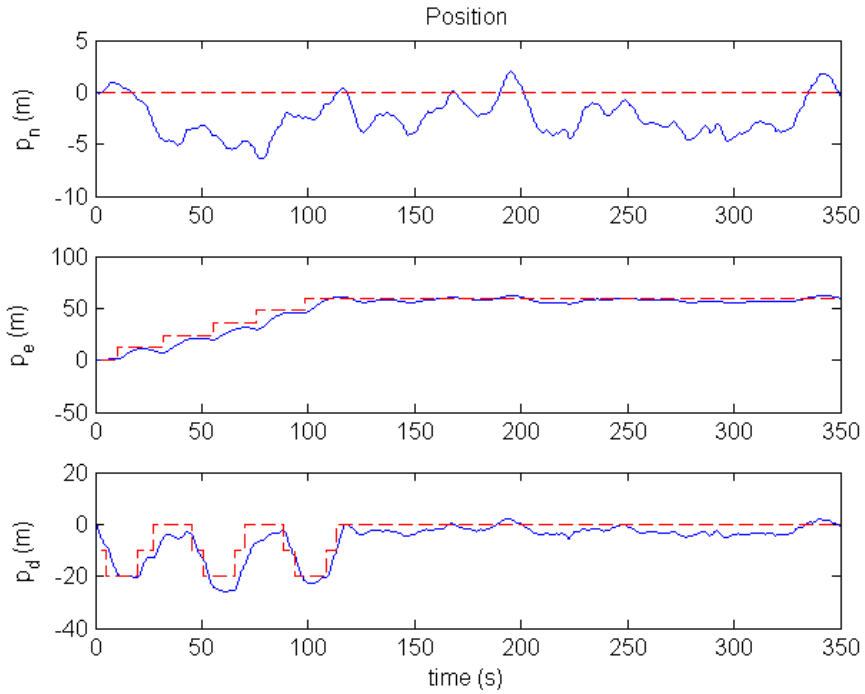

Fig. 37. This Figure illustrates the position estimated (red dashed line) vs. the actual position of the UAV (blue solid line) of dense landmark configuration

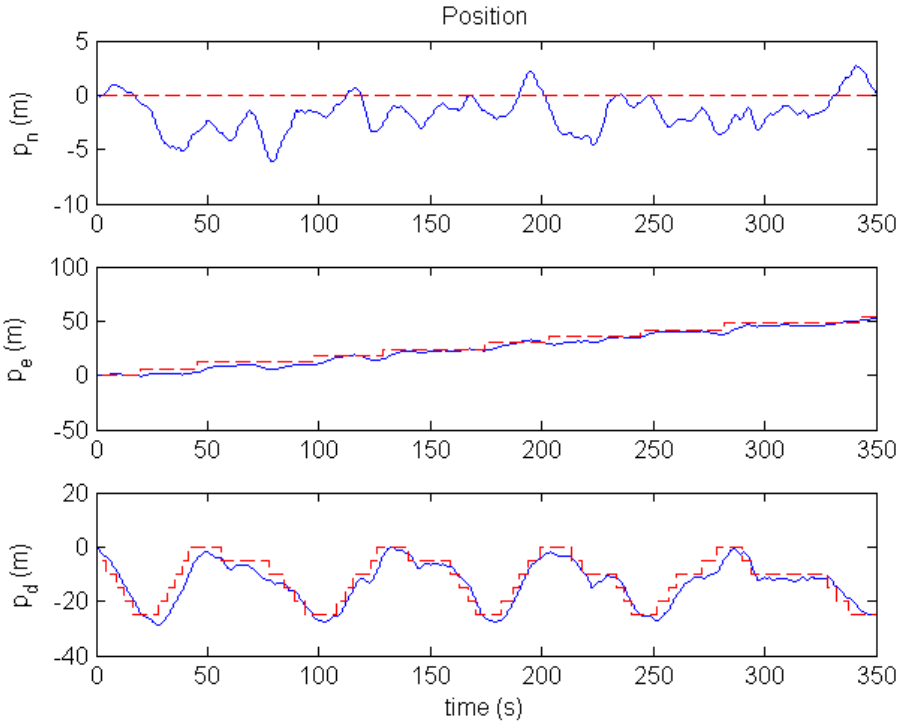

Fig. 38. This Figure illustrates the position estimated (red dashed line) vs. the actual position of the UAV (blue solid line) of sparse landmark configuration

Table 10. RMSE values of the dense and sparse landmark configuration in the North/East/Down directions.

Direction	Dense Landmark Configuration	Sparse Landmark Configuration
North	2.3897	3.3552
East	3.6087	6.8454
Down	3.5710	5.3791

The simulation results were deemed satisfactory. The UAV manages to localize itself even the presence of wind disturbance that is produced by Dryden Gust model. The built-in Simulink function was utilized to include the Dryden Gust Model. The final results are depicted in Figs 37 and 38. Obviously, in the dense landmark, the localization algorithm performs better than sparse landmark configuration. This can be concluded in Table 10.

The operation time of the UAV is inversely proportional to total thrust that is produced by four vertical rotors. In other words, the frequency of the undulation on the vertical movement will decrease the operation time of the quadrotor due to high energy consumption to generate thrust. The precise battery model is crucial to estimate the remaining operation time. In order to achieve that the remaining battery life is derived as:

$$remaining\ battery\ life = initial\ battery\ capacity \times e^{-\alpha \|T\| t}$$

$$\|T\| = \sqrt{T_1 + T_2 + T_3 + T_4}$$

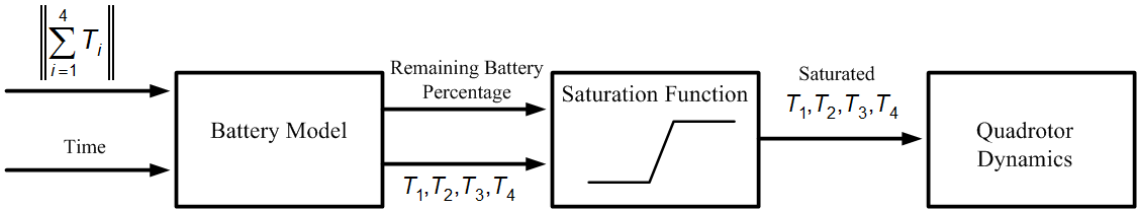

Fig. 39. The developed battery model for UAV.

The control inputs which are T_1, total thrust, T_2 rolling moment, T_3 pitching moment and T_4, yawing moment, are saturated depending on remaining battery life of the vehicle and saturated control inputs are fed to dynamic model of the UAV. The develop battery model was included to simulation as shown in Fig. 39.

After the battery model is included to Simulink model, the next step is to create an emergency scenario that validates the safe operation. In this simulation test, when the remaining battery life drops below a critical level, the UAV should land to home position in order to charge or change the flat battery with a new one. The critical battery level is determined by considering the accomplished and remaining task percentage.

When the emergency scenario is ignored, the preliminary simulation results show that when the battery life goes below the critical level the quadrotor starts to loose

altitude and cannot finish the assigned task. The simulation result is illustrated in Fig. 40. In Fig. 41, it is illustrated that the total thrust produced by propellers is not enough to hold the vehicle at the reference altitude that means that the produced total thrust is less than its weight.

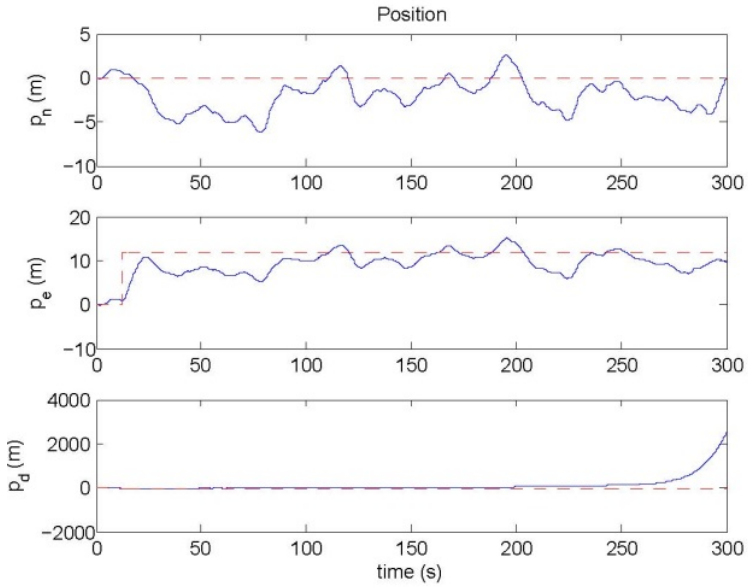

Fig. 40. This Figure illustrates the position estimated (red dashed line) vs. the actual position of the UAV (blue solid line) when emergency scenario is ignored

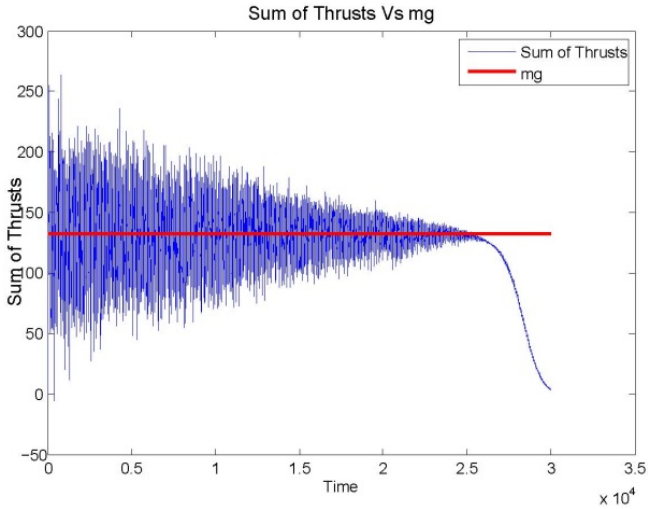

Fig. 41. This Figure illustrates the total weight of the vehicle (red line) vs. the sum of total thrust (blue line) when emergency scenario is ignored

When the emergency scenario is considered, the simulation results show that the UAV returns to its home position in emergency. This result can be concluded in Fig 42. In Fig. 43, it is illustrated that while the weight of the vehicle is compensated it could also produce adequate thrust to follow the generated trajectory.

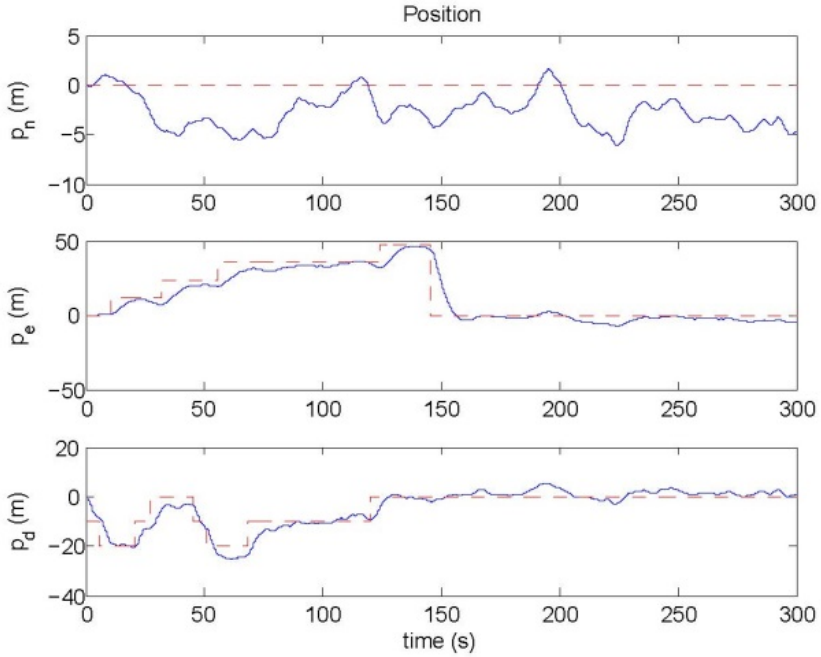

Fig. 42: This Figure illustrates the position estimated (red dashed line) vs. the actual position of the UAV (blue solid line)

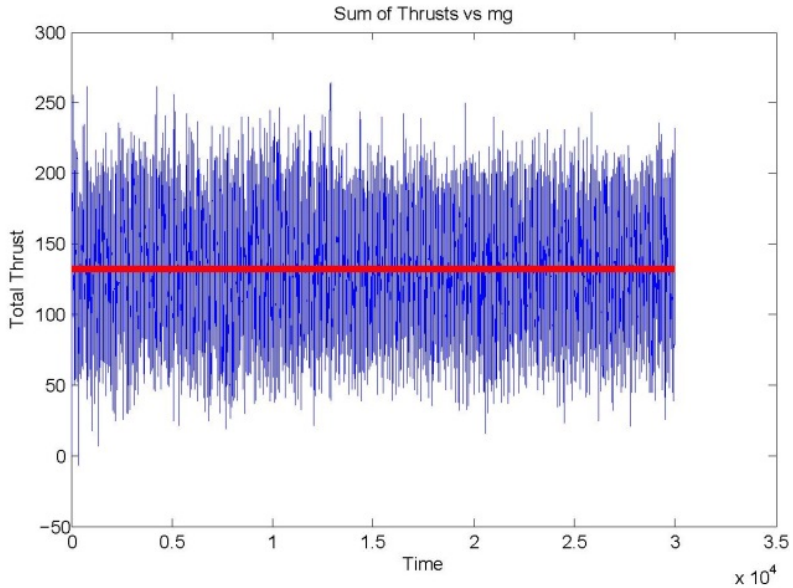

Fig. 43. This Figure illustrates the total weight of the vehicle (red line) vs. the sum of total thrust (blue line) when emergency scenario is considered

The UAV dynamics are illustrated in Fig. 44. To this extent we have derived a simplified mapping that relates the UAV's velocity dynamics with respect to the controller input. In our particular case the controller's input is the position error.

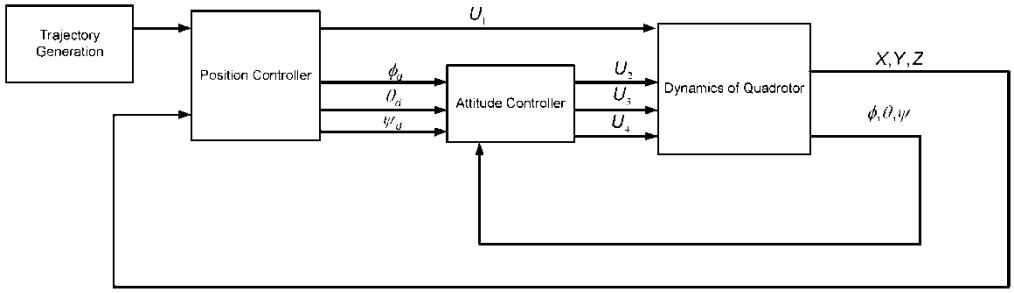

Fig. 44. Block diagram of the UAV dynamics and their interconnections. A simplified mapping of the UAV's velocity with respect to the controller's input, is preferred to represent the above representation.

This mapping is verified by the high correlation between the two signals that we acquired from the UAV's simulator. The two signals as extracted by the simulator are depicted in Fig. 45. On the left hand side of Fig. 45, the original velocity and position error are illustrated (in the North/East/Down coordinates). The right hand side of the same figure depicts the validation results of the input/output mapping. To represent our model we used the following simple Low Pass (LP) filter:

$$V_{k+1} = (1 - \frac{\Delta t}{\tau})V_k + \frac{a\Delta t}{\tau} e_p$$

where Δt is the sampling time, e_p is the position error and τ is the LP filter's time constant. The above mapping was proven to be well suited resulting to minimal Round Mean Square Error (RMSE). The RMSE values are depicted in Table 11.

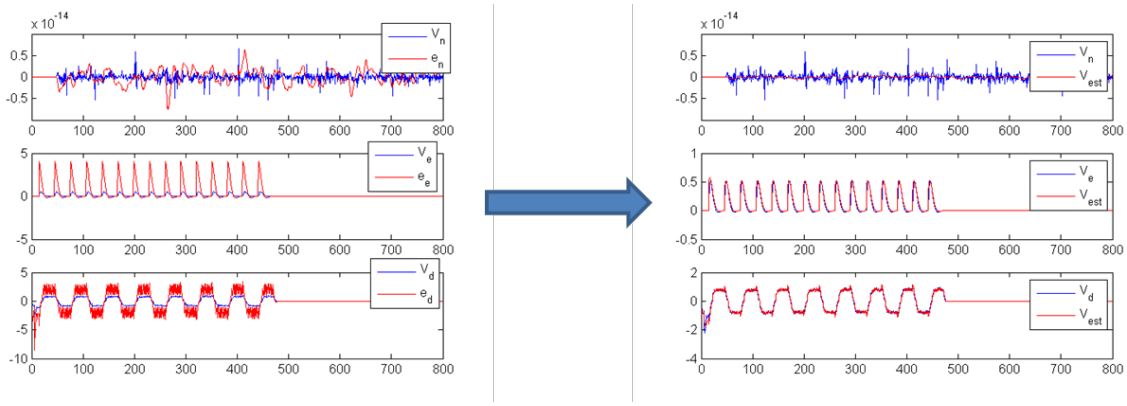

Fig. 45. Mapping of the UAV's velocity with the position error that is injected to the controller. The left graph indicates the actual signals of the position error and velocity, while the right hand side illustrates the output of the identified model.

Table 11. RMSE values of the identified models in the North/East/Down directions

Direction	RMSE (m/s)
North	6.877x10^-16
East	0.0562
Down	0.0849

When the vehicle localizes itself in the absence of landmarks, it relies exclusively to the accuracy of the above model. To this extent, a high fidelity mapping plays critical role to the performance of the localization algorithm.

During its operation the UAV has two distinct measurement models. The first one corresponds to the case that a landmark is located in the LOS of the vehicle. If a landmark is not visible by the front camera, the localization algorithm is relayed to a feature detection estimation module. This module derives position estimates based on the velocity of the vehicle. The noise levels at the second case are significantly higher compared to the estimates using fiducials. The two measurement models are depicted in Fig. 46.

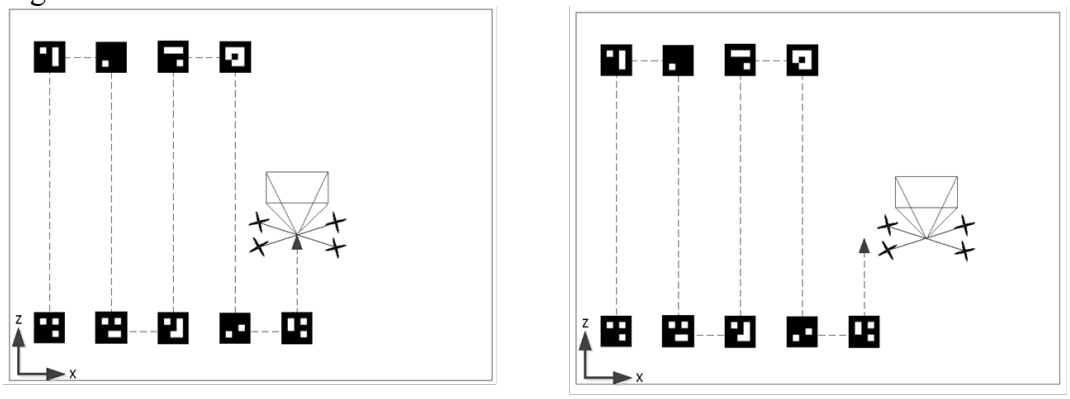

Measurement through Fiducial

$$z_k^1 = p_k + \underbrace{\eta_k^1}_{noise}$$

Measurement fiducial can not be captured

$$z_k^2 = v_k + \underbrace{\eta_k^2}_{noise}$$

Fig. 46. Noise models depending of the occurrence of a landmark in the LOS of the vehicle.

The fiducials markers were successfully implemented to the simulator. The visualization of the vehicle is depicted in Fig. 47.

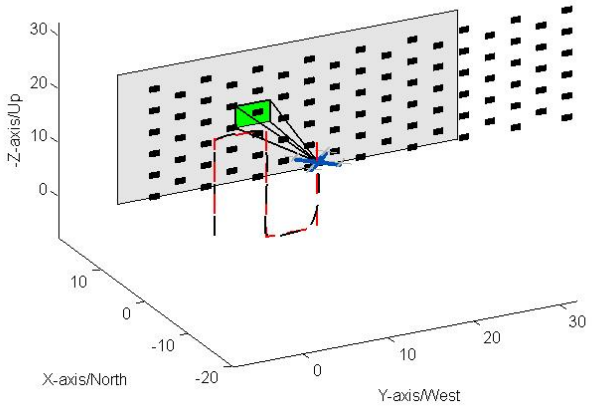

Fig. 47. This figure illustrates the simulator that was used to validate the localization algorithms. The black rectangular shapes denote the fiducial markers.

In the development of UAV motion prediction models, the final deliverable involves the implementation of a Kalman Filter (KF) to derive the UAV's position estimate based on the noisy available measurements. The classical implementation of the KF filter involves tow sequential steps: Prediction and correction. The associated equations are depicted in Fig. 48.

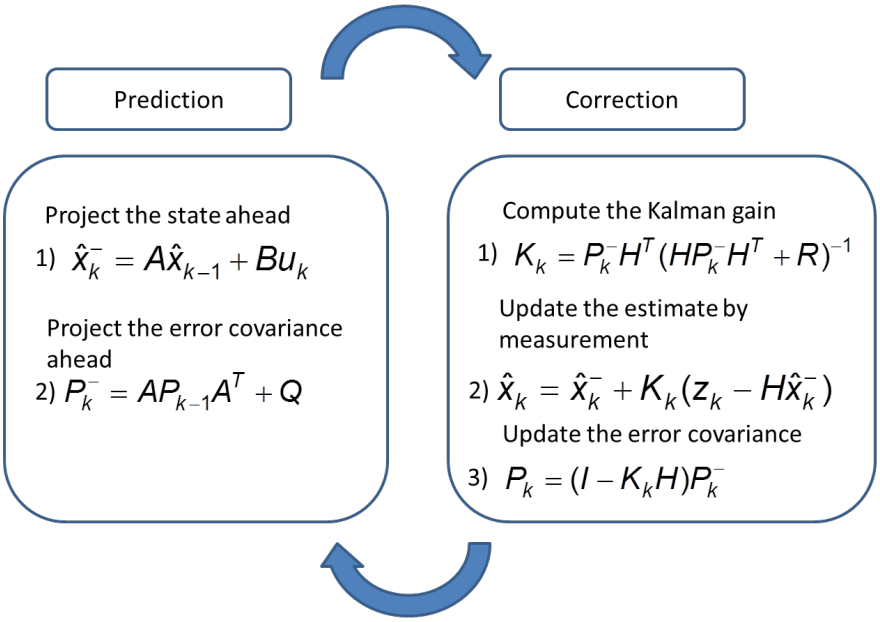

Fig. 48. Prediction and correction steps of the KF algorithm

The process model that had been used is described by the following equations:

$$\begin{bmatrix} p_{k+1} \\ v_{k+1} \end{bmatrix} = \begin{bmatrix} 1 & \Delta t \\ 0 & 1 \end{bmatrix} \begin{bmatrix} p_k \\ v_k \end{bmatrix} + \begin{bmatrix} 0 \\ \Delta t\, \alpha \end{bmatrix} u_k + \begin{bmatrix} 0 \\ \omega_k \end{bmatrix}$$

Depending of the occurrence of a landmark in the LOS, the KF switches between the two measurement models as depicted in Fig. 49.

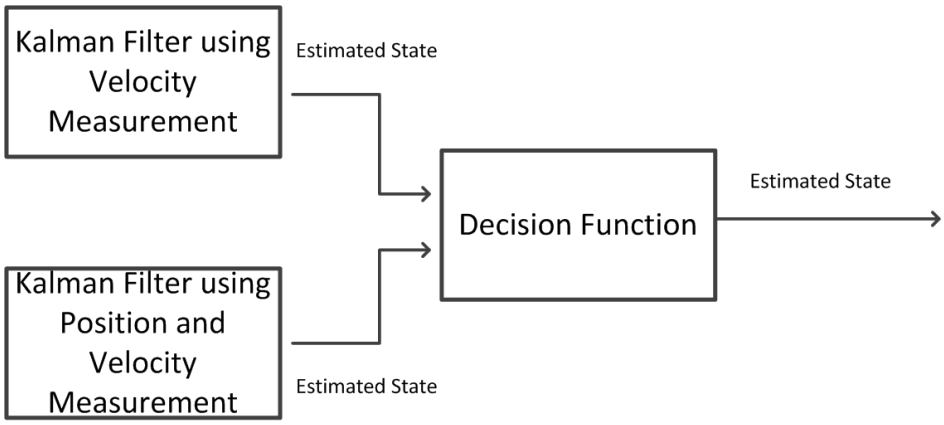

Fig. 49. Switching between the measurement models during the execution of the KF algorithm

The final localization results were deemed satisfactory. The UAV manage to localize itself even in the presence of significant uncertainty while moving without a landmark onsite. The final results are depicted in Fig. 50.

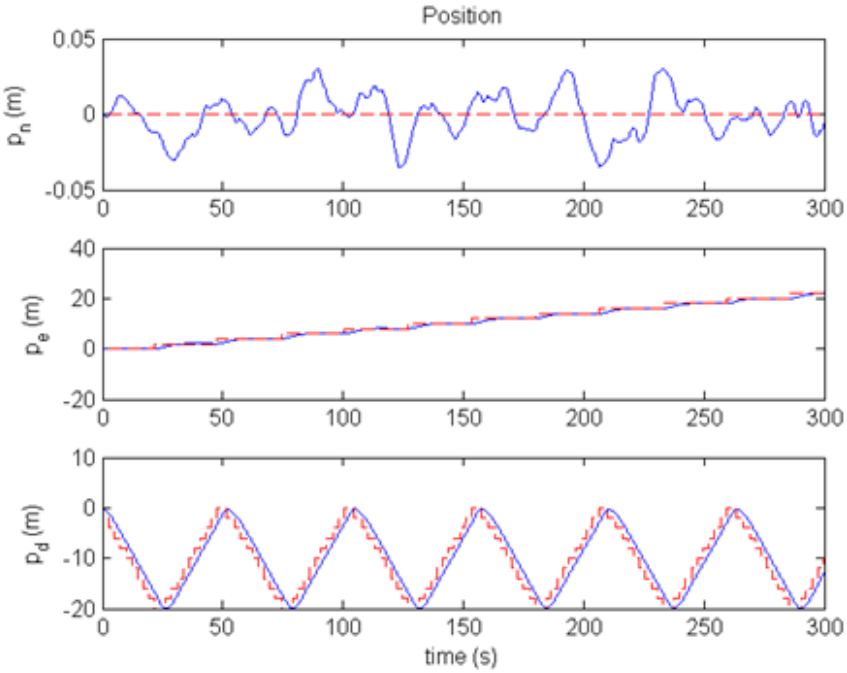

Fig. 50. This Figure illustrates the position estimated (red dashed line) vs. the actual position of the UAV (blue solid line)

5.2 Development of UAV platform

To manufacture the hardware component of a UAV platform, we need to complete the power component analysis in order to select a power system for the vehicle. Fig. 51 shows the test result of different power configurations for the CivilEye system. The final mechanical design of the UAV platform for the CivilEye system is shown in Fig. 52. The electronics schematic of our design is provided in Fig. 53.

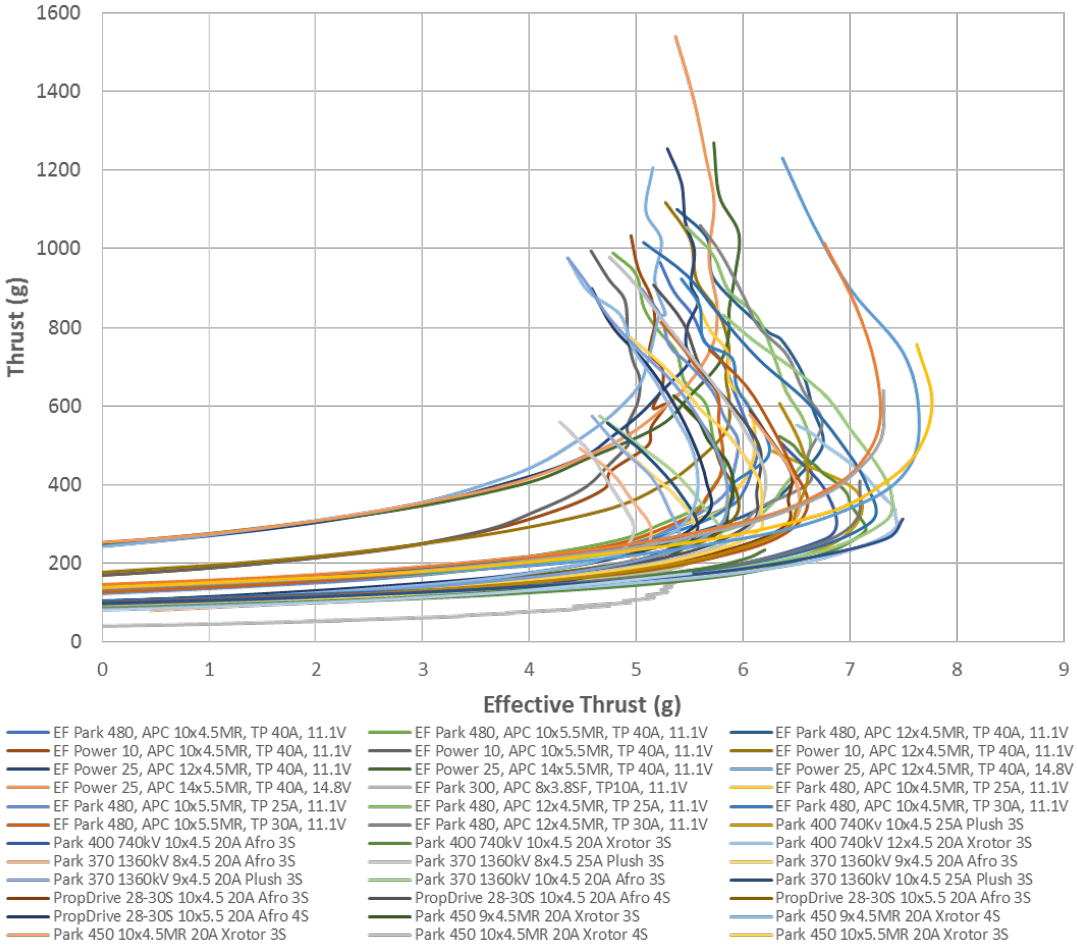

Fig. 51. Power curves for tested power configurations (Prop, Battery, Motor, ESC).

Fig. 52. Final design of the UAV platform for the CivilEye system

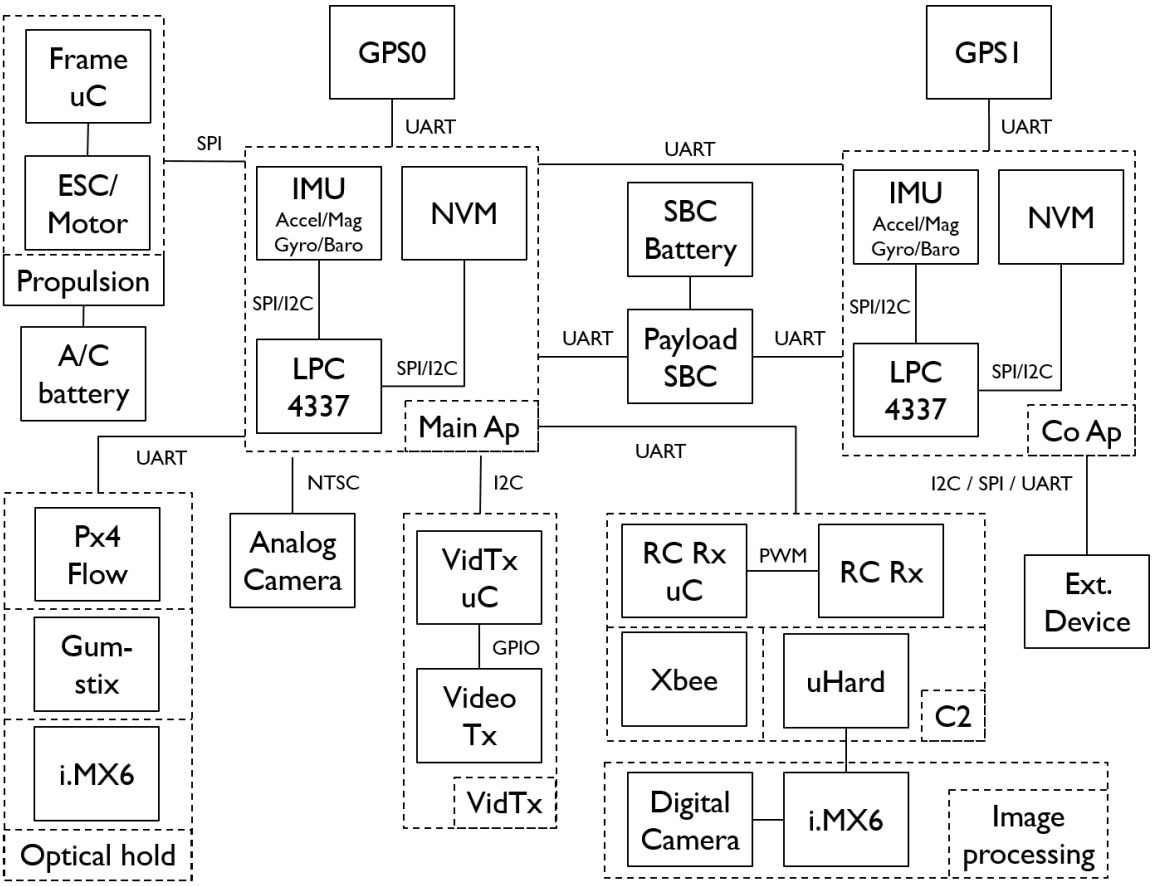

Fig. 53. Electronics schematic of the CivilEye system

Finally, we have developed a family of UAV tailored to infrastructure inspection. These UAV/aircrafts leverage experience from the military InstantEye sUAS. Initially, there are two aircrafts which target payloads of ~0.5-1.5lb and a second system which is optimal for payloads of ~2-3.5lbs. Both aircrafts share the same base electronics but have airframes optimized for operation of different sizes and weights/payloads. The Medium Lift CivilEye can operate with ~1.5lb of payload for ~18 minutes in winds in excess approximately 15 mph winds. The Heavy lift CivilEye is optimized for 2.5lbs of payload for 20 minutes in winds in excess of 15 mph. The InstantEye, Medium Lift CivilEye and Heavy Lift CivilEye are all shown in Fig. 54.

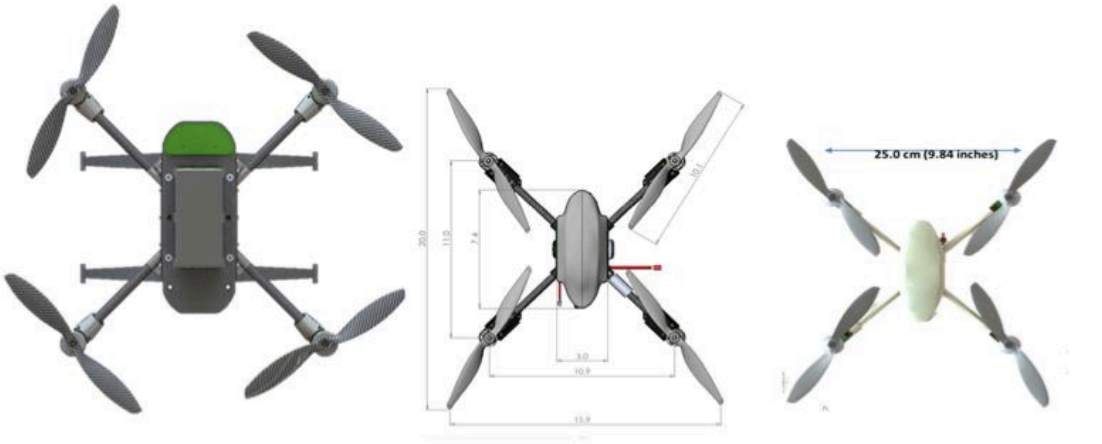

Fig. 54. Left to Right - Heavy Lift CivilEye, Medium Lift CivilEye and military InstantEye.

Specifications of the developed Medium Lift UAV system are summarized in the following:

- Demonstrated flight (hover, hold position, controlled flight) with the medium lift quadcopter.
- Implemented advanced control for stability, gust rejection and non-optimal payload placement. In terms of work completed the following lists the major modules.
  - Stability code – 100%
  - Altitude hold – 80%
  - Navigation/GPS = 80%
  - Payload weight flight controller tuning = 20%
  - Battery meter = 0% complete (not required for evaluation)
  - IMx6 integration = 100%

Specifications of the developed Heavy Lift UAV system are summarized in the following:

- Currently developing the infrastructure for system ID and system calibration = 80%
- Mechanical design for airframe = 80%
- Mechanical design for payload bays and payload interface = 30%
- Prototyping of propulsion elements for bench testing = 100%
- Flight Electronics = 80% (proving out on Medium Lift aircraft)
- Payload mechanical and electrical interface design = 10%
- Power/ Battery (4S battery – floats between 15V-12V as battery depletes)
- I/O USB 2.0 or USB 3.0 for camera system and UART for the radar system

5.3 System integration

In the system integration part of the CivilEye system, we need to develop both hardware and software solutions. Our hardware solution of system integration starts with the development of prototype electronic printed circuit boards (PCBs) for autopilot, hub board, power boards, GPS, video processor, and radio interface.

Regarding our software solution of system integration, we migrate the core software to embedded-able C++ in order to optimize the software for maximum run-time efficiency. We also have advanced the electronics design of the I.MX6 vision processing payload (for the SLAM algorithms). The first phase of the SLAM algorithm processing has been completed with the successful demonstration of the image resample and stretch algorithms using a 5mp camera and computer. A final trade analysis of processors capable of both video compression processing for stabilization and attaching meta-data into a MPEG-2 transport stream has also bee conducted. In our study, we have considered the following solutions in our trade study: Zynq-7000 SoC, TI OMAP 3 series, TI Davinci series, TI OMAP 4 series, Tegra K1, Broadcom BCM3826 (Raspberry pi), and Freescale i.MX6. Among these competing technologies, the Freescale i.MX6 (selected in the point of departure design) is the only processor with all of the following attributes:

- Powerful processing: quad-core ARM A9
- Hardware acceleration for stabilization: Vivante GC2000 GPU which supports OpenGL
- High speed camera connection (4 lane MIPI CSI-2 or USB 2.0): 4 lane MIPI CSI-2
- Parallel camera connection for FLIR integration (either directly or through analog digitizer)
- Available in quantity for future integration onto custom PCB.
- Open source schematics available for faster future integration onto custom PCB.

The i.MX6 on a bench development interface board is shown in Fig. 55.

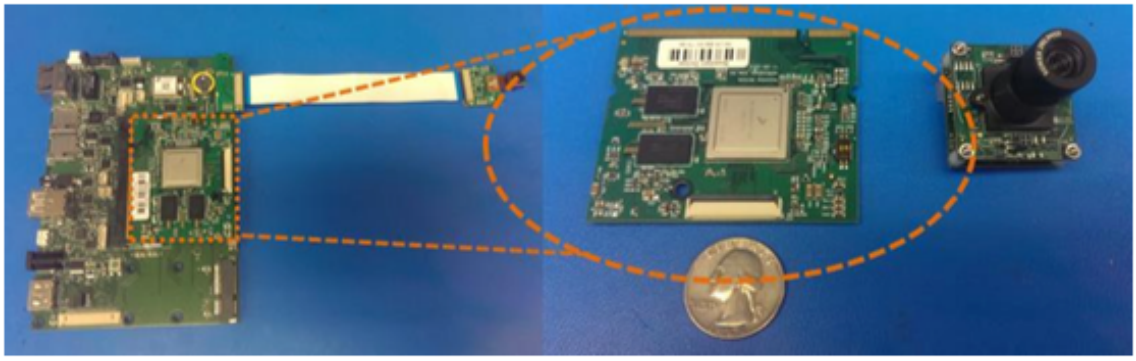

Fig. 55. (left to right) IM6 on benchtop interface board and i.MX6 Board with 12MP camera.

We have advanced the ground control software to prepare for the bridge inspection mission set and workflow. Below is a snapshot of the ground control station / flight

planner that PSI has. Fig. 56 shows an example image taken by the current CivilEye system.

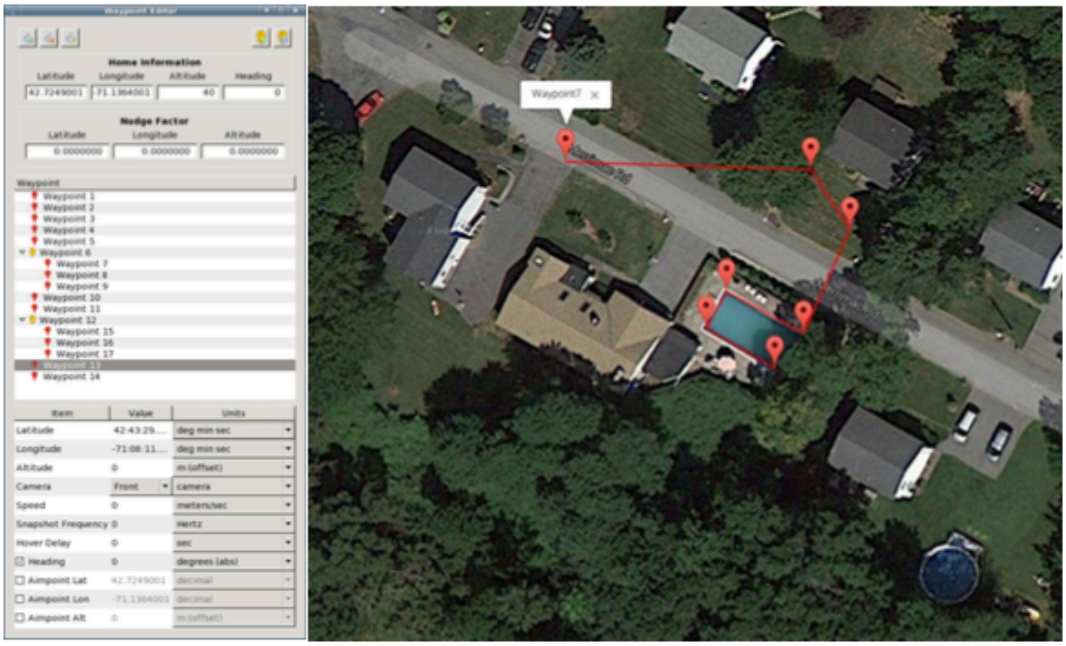

Fig. 56. Screen shot of ground control mission planner with waypoints.

To validate the performance of integrated CivilEye+Radar (Fig. 57) and CivilEye+DIC (Fig. 58) systems, the following tests were carried out.

1) The medium lift vehicle was successfully used to carry the DIC and radar payloads (tested indoors at PSI facility).
2) Waypoint control software has been developed. The software will allow an operator to fly the vehicle with precision, repeatable navigation. This is an important capability that is required for change detection. The software is now being ported to an android operating system for use on a laptop or tablet.
3) The electronic design of the vehicles main control board and hub board has been validated and the limitations are understood.
4) We has conducted preliminary testing of a GPS denied/optical position hold based flight control system from field tests. The system provides the basis for accurate control and navigation in GPS denied conditions.

To validate the performance of the integrated CivilEye system, we have conducted fly tests of the CivilEye+Radar system (see Fig. 59) and the CivilEye+DIC system (see Fig. 60).

Fig. 57. Integrated CivilEye+Radar system

Fig. 58. Integrated CivilEye+DIC system

Fig. 59. Fly test of the integrated CivilEye+Radar system

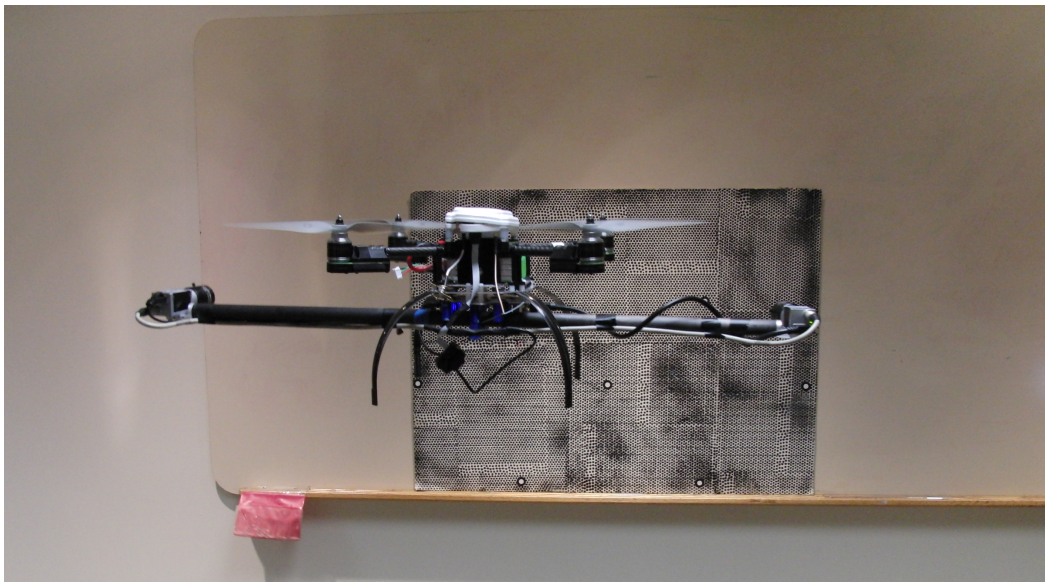

Fig. 60. Fly test of the integrated CivilEye+DIC system

Chapter 6. Development of an Inspection Plan and Decision Support Tool

This chapter reports our approach and research outcomes in the development of an inspection plan and decision support tool.

6.1 Development of an inspection plan

To integrate the developed CivilEye system into the current inspection practice, bridge inspection procedure is used as an example. Fig. 61 shows how the CivilEye system can be integrated into the existing bridge inspection procedure/framework.

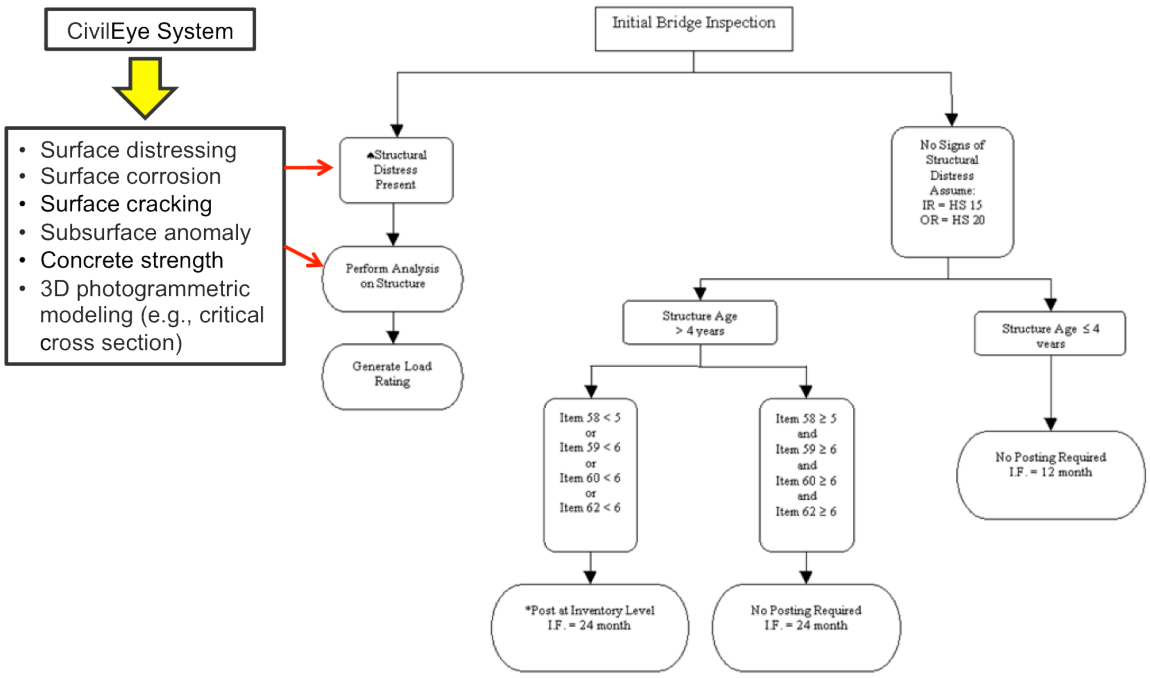

Fig. 61. Integration of the CivilEye system with existing bridge inspection procedure

This integration assists us to identify the value of the developed CivilEye system, as well as to develop an inspection plan using the system. Steps in the inspection plan are listed in the following.

1. Identify a candidate bridge (or other structural systems) from previous inspection results/ratings.
2. Setup up local reference coordinates and boundary coordinates for the operation of CivilEye system.
3. Launch the CivilEye+DIC system to collect video images and DIC images (both surface information).
4. Construct DIC models and photogrammetric models for image/data integration. Meanwhile, identify suspicious locations for subsurface SAR imaging.
5. Launch the CivilEye+radar system to collect subsurface SAR images.

6. Develop the 3D point cloud model of the bridge using 3D photogrammetry.
7. Integrate DIC and SAR images into the 3D point cloud model of the bridge.
8. Use the displacement profiles provided by DIC images to detect **surface cracking**.
9. Use the stress profiles provides by DIC images to detect **surface distressing**.
10. Use the visual image (from videos), DIC and SAR images to detect steel **corrosion**, with or without the leaking of galvanized products on structure's surface.
11. Use SAR images to detect **subsurface anomalies**.
12. Use the correlation between SAR amplitude and the mechanical strength of concrete to predict **concrete strength**.
13. Include the abovementioned information in routine bridge inspection reporting.
14. Include the abovementioned information in the structural analysis (e.g., simplified analysis or numerical analysis) of the bridge, if necessary.

6.2 Development of a decision support tool

The framework of a decision support tool and a strategic plan has been developed, as shown in Fig. 62.

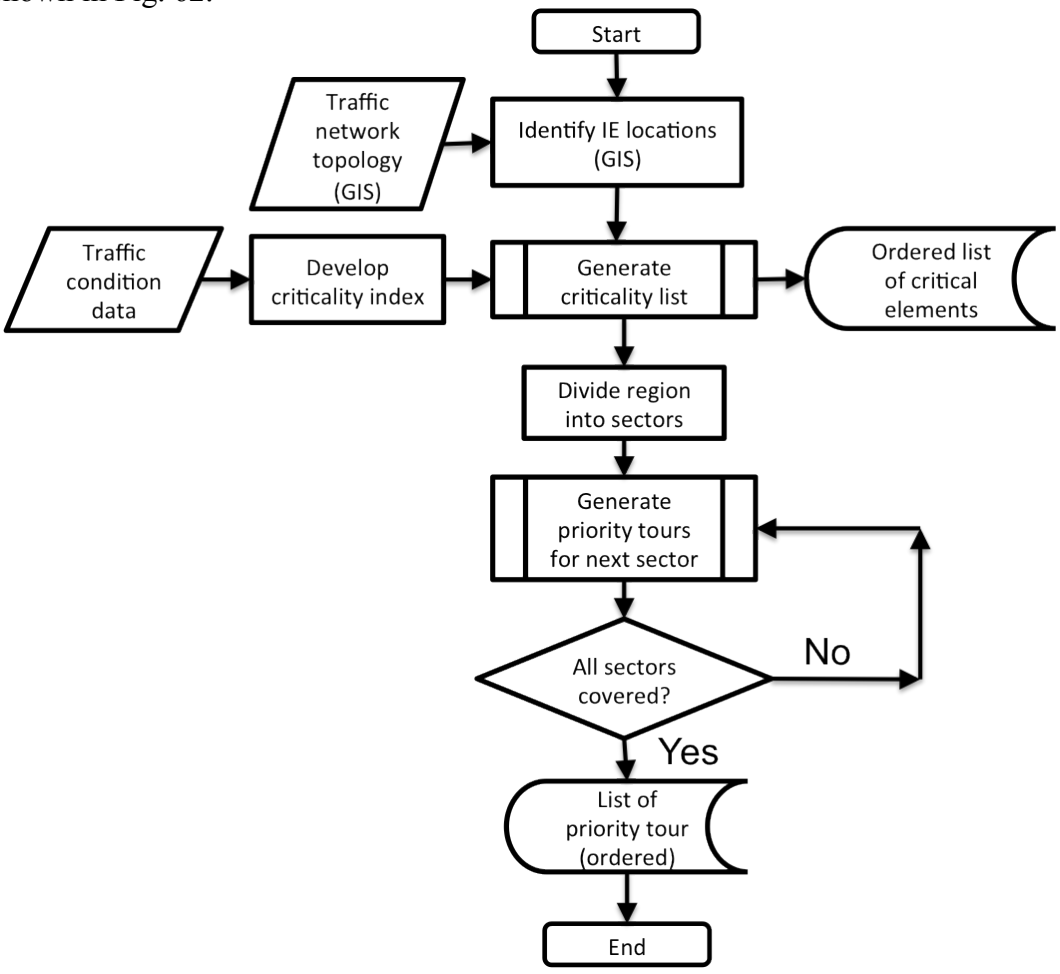

Fig. 62. Framework of the decision support tool and the strategic plan

In Fig. 62, the decision support tool requires the input of traffic condition data that can be either experimentally measured or numerically simulated. Some cities and townships periodically collect traffic information using manual approaches (e.g., traffic counters) or sensors (e.g., infrared). Considering the cost of collecting traffic information, numerical simulation offers an advantage for understanding the pattern and behavior of traffic networks when only limited traffic information available. The following paragraphs describe our traffic simulation approach.

Consider a small arterial road network with three intersections along the arterial, as shown in Fig. 63. The origin-destination (OD) matrix used is shown in Table 11 below for only cars. A commercially available traffic simulator, Aimsun (by Transport Simulation Systems), was used in this study.

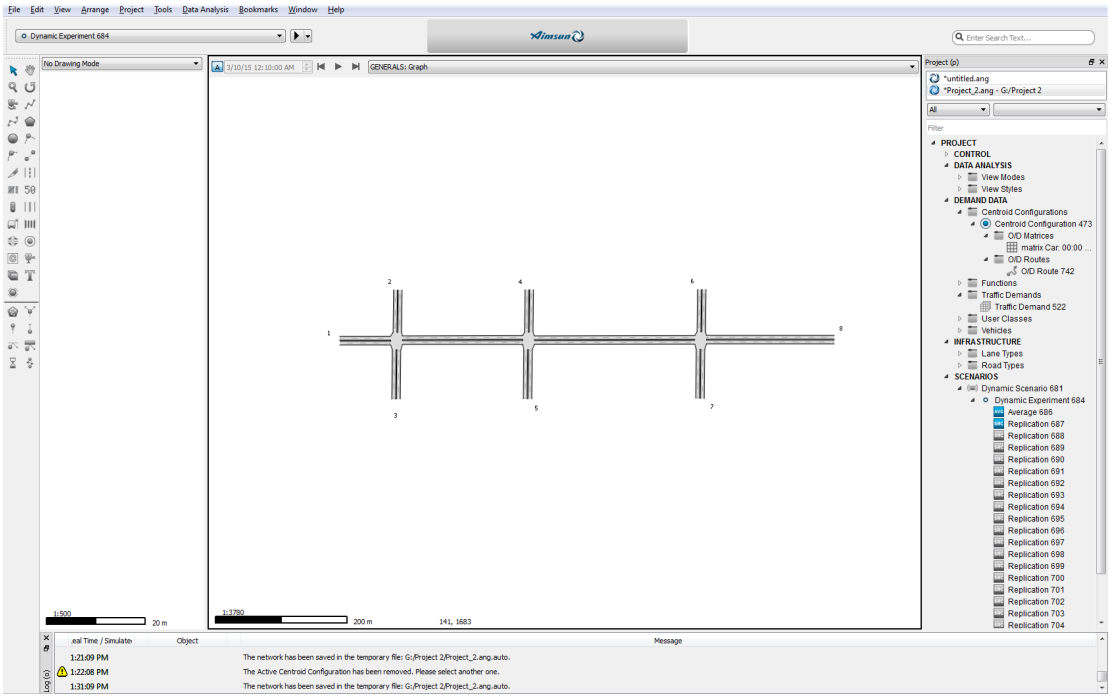

Fig. 63. Model of the 3-arterial network in Aimsun

Table 11. OD Matrix of the 3-arterial network

ID	474-1	475-3	476-2	477-5	478-4	479-7	480-6	481-8	Totals
474-1	0	0	0	0	0	0	0	400	400
475-3	0	0	500	0	0	0	0	0	500
476-2	0	600	0	0	0	700	0	0	1300
477-5	0	0	0	0	240	0	0	0	240
478-4	0	0	0	240	0	0	0	0	240
479-7	0	0	700	0	0	0	600	0	1300
480-6	0	0	0	0	0	500	0	0	500
481-8	400	0	0	0	0	0	0	0	400
Totals	400	600	1200	240	240	1200	600	400	**4880**

In Fig. 63, protected left-turns were designated for traffic from (2) and (7) but restricted for the rest of the approaches. Traffic was added onto the main arterial (1 directly to 8) from the feeder roads (2, 3, 4, 5, 6, and 7). All other network values were kept to their default values in Aimsun. The arterial was simulated twenty times for a period of one hour (12:00 ~ 01:00).

The 3-arterial network was successfully coded and simulated in Aimsun. A summary of the simulation output is shown in Table 12 for the 3-arterial network. For a flow of 4186.9 vehicles in one hour, the average delay time of the 20 simulation is 740.99 seconds for every mile of the network. A reduced speed is also experienced as the average speed of the network is only 15.73 mph. This value takes into consideration having only cars in the network. Therefore, it is also of interest to be more realistic by including other vehicle types to the network. Figs. 64 and 65 show simulated time delay and flow dynamics for cars.

A more comprehensive comparison can be included in future works by altering the traffic volumes. This way, we can simulate how a network behaves when a certain infrastructural system (e.g. a bridge) is closed or partially closed to traffic. Simulated traffic condition data can also be provided to the decision support tool shown in Fig. 62.

Table 12. Summary of simulated traffic network output

Time Series	Value	Standard Deviation	Units
Delay Time Car	740.99	39	sec/mi
Density Car	84.4	N/A	veh/mi
Flow Car	4186.9	N/A	veh/h
Harmonic Speed Car	11.15	7.14	mph
Max Virtual Queue Car	621.3	N/A	vehs
Mean Queue Length Car	54.32	N/A	vehs
Mean Virtual Queue Car	295.02	N/A	vehs
Number of Stops Car	4.68	N/A	
Speed Car	15.73	0.2	mph
Stop Time Car	716.5	38.95	sec/mi
Total Distance Travelled Car	947.18	N/A	mi
Total Travel Time Car	251.58	N/A	h
Travel Time Car	847.53	38.98	sec/mi
Vehicles Inside Car	91	N/A	vehs
Vehicles Lost Inside Car	0	N/A	vehs
Vehicles Lost Outside Car	0	N/A	vehs
Vehicles Outside Car	4186.9	N/A	vehs
Vehicles Waiting to Enter Car	615.25	N/A	vehs

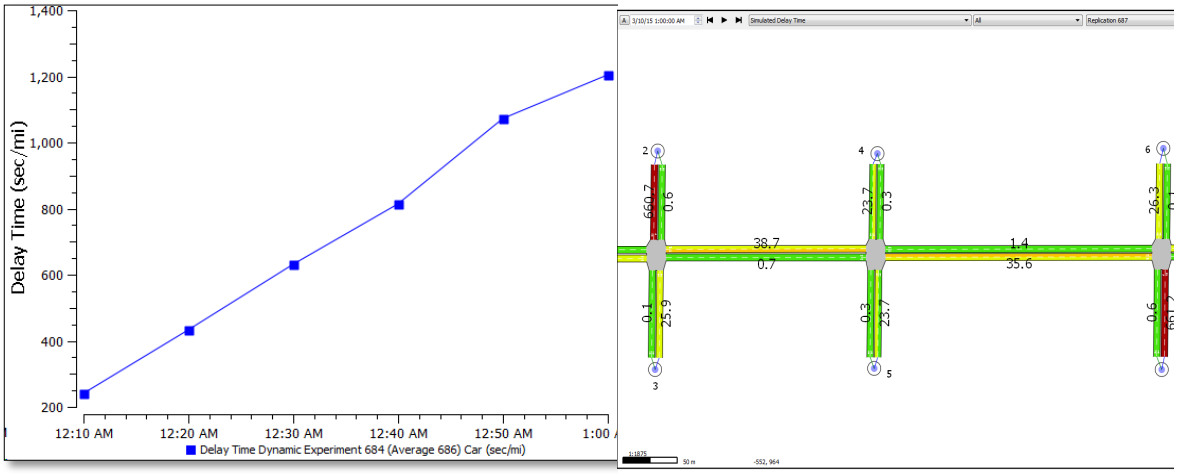

(a) (b)

Fig. 64. Simulated time delay

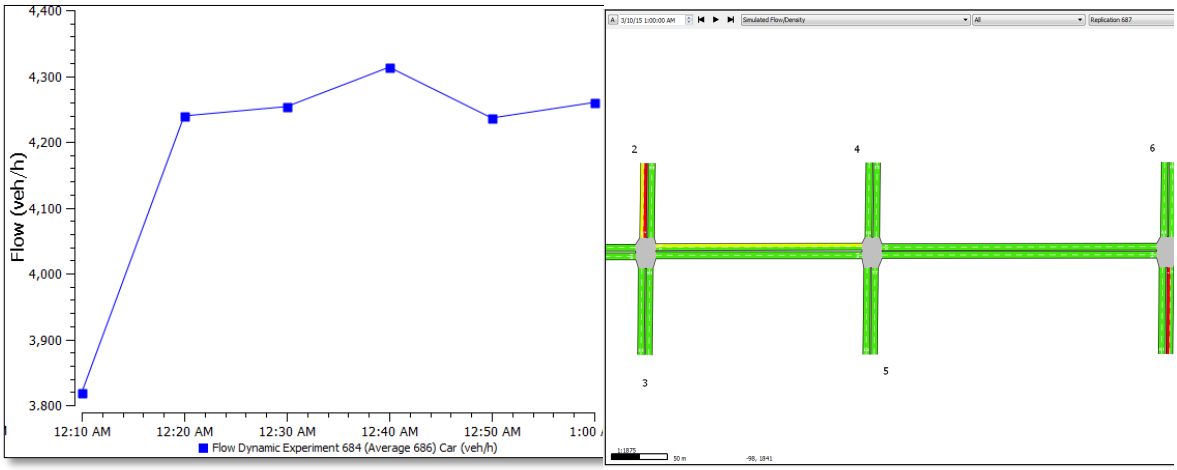

(a) (b)

Fig. 65. Simulated flow dynamics for cars

Fig. 66 illustrates our proposed system-level solution by using the CivilEye system. In Fig. 66, both optical (DIC) and radar (imaging radar) information will be integrated into the decision support tool in an inspection plan for inspecting various defects/damages. The platform for image integrating is proposed to be 3D point cloud models that can be processed using cloud computing to allow end users to download integrated 3D point cloud models onto their mobile devices.

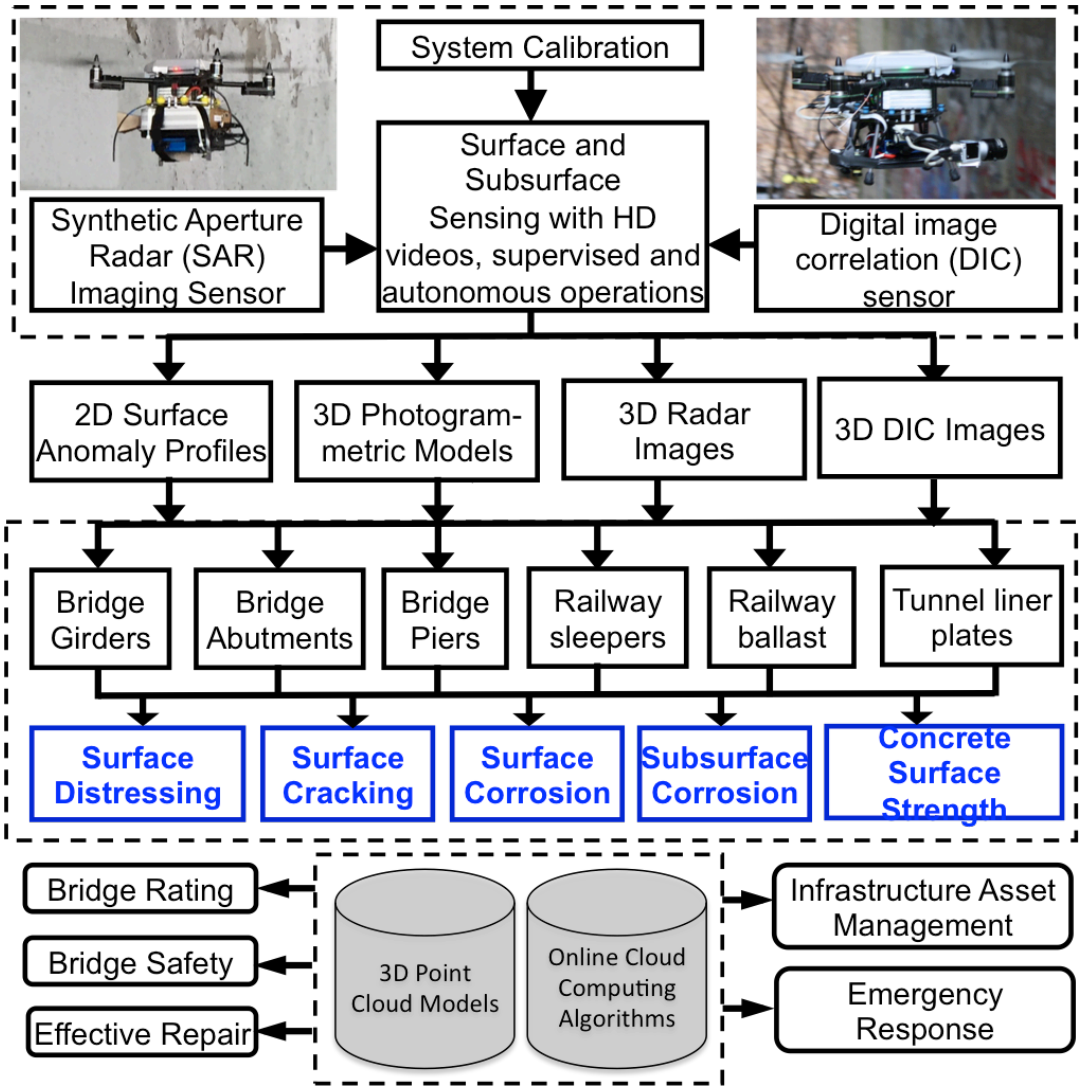

Fig. 66. System-level solution of the CivilEye system

Chapter 7. Laboratory and Field Validations

In this chapter, we report our laboratory and field validations of the CivilEye system, using DIC and imaging radar sensors.

7.1 DIC Laboratory Tests

The laboratory tests performed provide insight about the CivilEye+DIC system's ability to monitor surface crack growths in stable and semi-stable environments, the usable scanning area, and error associated with positioning inaccuracy. Table 13 summarizes the tests performed and the investigated factors for a comparison at a glance.

Table 13. Overview of laboratory experiments

Experiment	Factors Investigated
Displacement accuracy test	Validate ideal theoretical displacement accuracy
Strain accuracy and field of view test	Confirm valid measurement area theorized upon new lens and sensor configuration
UAV positioning error test	Investigate potential errors induced from likely less than ideal measurement conditions
Large area scans using stage stitching techniques	Explore feasibility of large area measurements

7.1.1 Displacement Accuracy Test

Once calibrated, the quality of the measurements recorded using the stereo camera pair was validated by taking several pictures of a target object prior to inducing displacements/strains. Theoretically the measured value is supposed to be equal to zero, but there will always be some level o f noise in the system, which can affect the accuracy of the measurement. As a result, non-zero values will characterize the result of the measurements. It easy to understand, that the smaller these values will be, the better the accuracy of the measurement will be. The initial values measured from a stationary system not subjected to deformations or stresses are referred to as the noise floor for the measurement. These noise floor values are a general indicator of the minimum value that can be measured with the DIC system as it is configured. Fig. 67 shows a test fixture capable of displacing the upper patterned plate in 0.01mm increments by means of a lead screw attached to a dial indicator. This system will also be used in later tests for evaluating the accuracy of the system in detecting sub-millimeter displacements and the associated strains. The areas highlighted in green are the surfaces recognized by the DIC software as the area of interest (i.e. the areas in which the computation of displacements and strains are performed) and are recalculated at each image stage from an initial stage used as reference. The locations of the white on black optical targets visible in Fig. 67 are also recalculated at each stage with the purpose of defining a local coordinate system with an x-axis always parallel to the axis of translation.

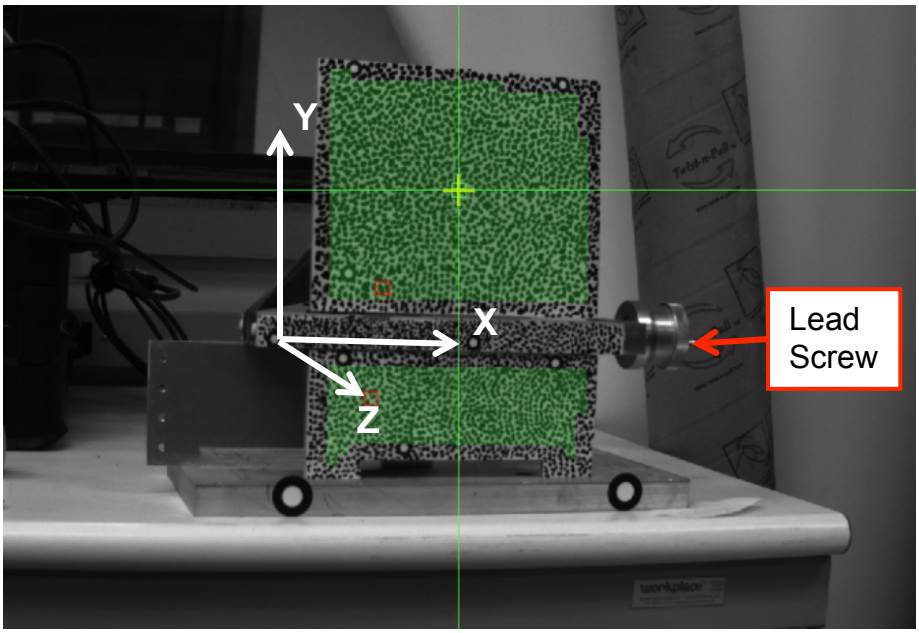

Fig. 67. Experiential structure for inducing known displacements

The noise floor of a measurement in the X and Y direction (the plane perpendicular to the cameras in Fig. 67) is typically +/- 1/300 of the effective pixel size on the target. For an 835mm field of view each of the 1626 vertical lines of resolution on the camera occupies 1.95mm on the target. A noise floor of +/- 0.006mm should be expected under ideal conditions. Fig. 68 displays the noise floor for the test fixture with the cameras fixed to a tripod and shows a displacement range of (-) 0.0028 to (+) 0.0031 mm, comparable with the theoretical one.

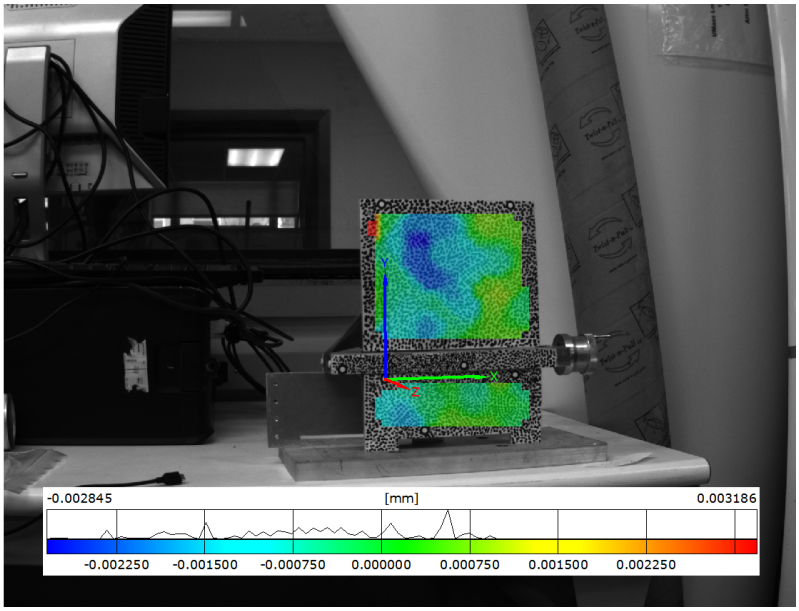

Fig. 68. Noise floor with cameras fixed to tripod

Another series of measurements were taken to investigate the effects of instability on the cameras (e.g. vibrations, unwanted displacement, etc.). During the image

acquisition the camera bar was held by hand; therefore subjecting the system to random movements. The variation in the positioning of the cameras can be estimated by viewing the displacement of the structure as a whole within the ARAMIS software. As shown in Fig. 69, the software assumes the cameras are stationary and that the test article is in motion with respect to the global coordinate system. During this experiment the camera's position was assumed to vary up to 4 cm in the Z direction and 7 cm in X and Y. As can be observed from results shown in Fig. 69, the measurement noise floor is extremely affected by the relative motion between the cameras and the test object. Values in the range – 77.08; +88.71 mm are observed. As shown in Fig. 70, when a rigid body correction is performed and the displacement is calculated in reference to a local coordinate system represented by the markers on the structure Fig. 70, the measurement has a noise floor range of (-) 0.00562 to (+) 0.00893 mm of in-plane displacement, on the same order of magnitude of the noise floor evaluated for the cameras over a tripod case.

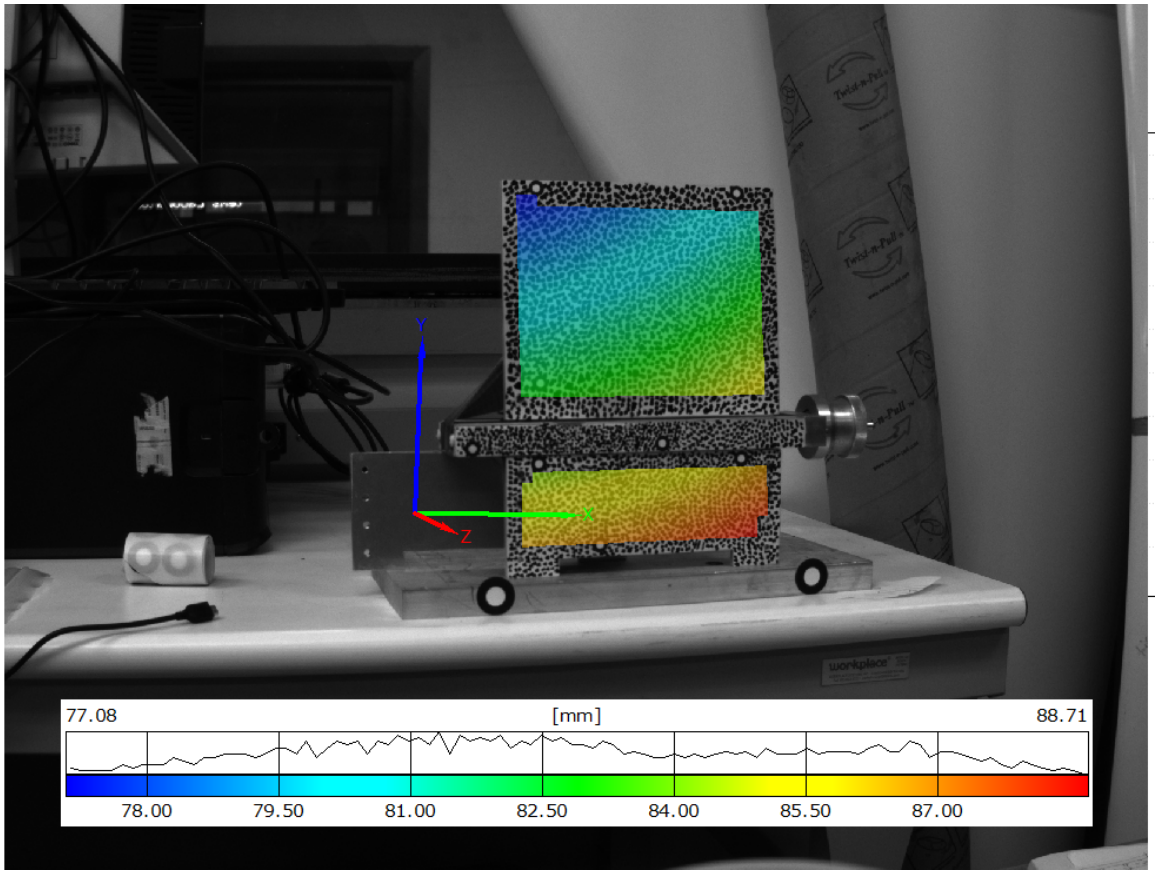

Fig. 69. Euclidean distance of test structure facets before rigid body correction

One of the advantages of the DIC system is its ability to identify cracks smaller than that can be identified by the human eye. To evaluate the capacity of the proposed CivilEye+DIC system in accurately measuring displacements, several well-known in-plane displacements were applied to the test object of Fig. 67, and data were recorded as the cameras stand over a tripod and were handheld. Fig. 71 shows the measured displacements of the upper plate of the test fixture as it is displaced along the lead screw.

The test shows the system's ability to identify the creation and growth of cracks in the 0.01; -0.1mm range.

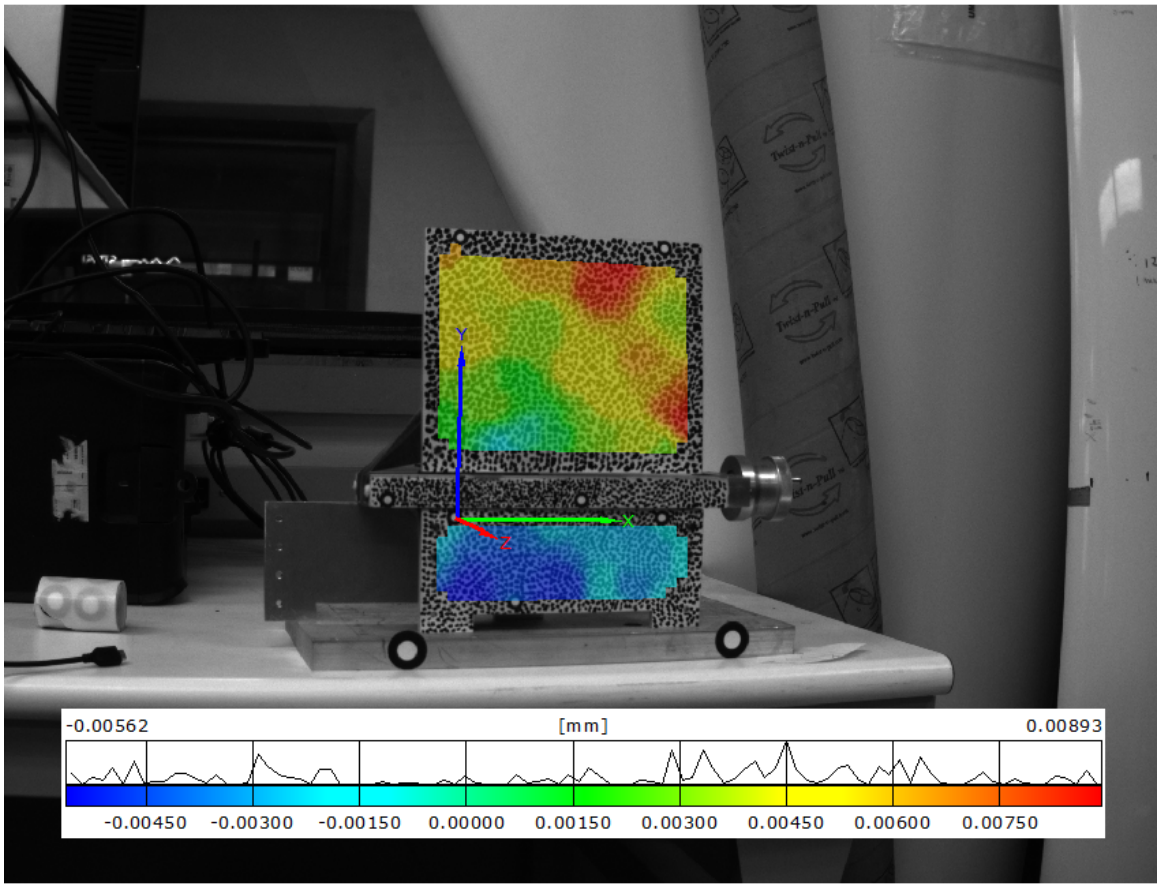

Fig. 70. Noise floor with cameras held in hand

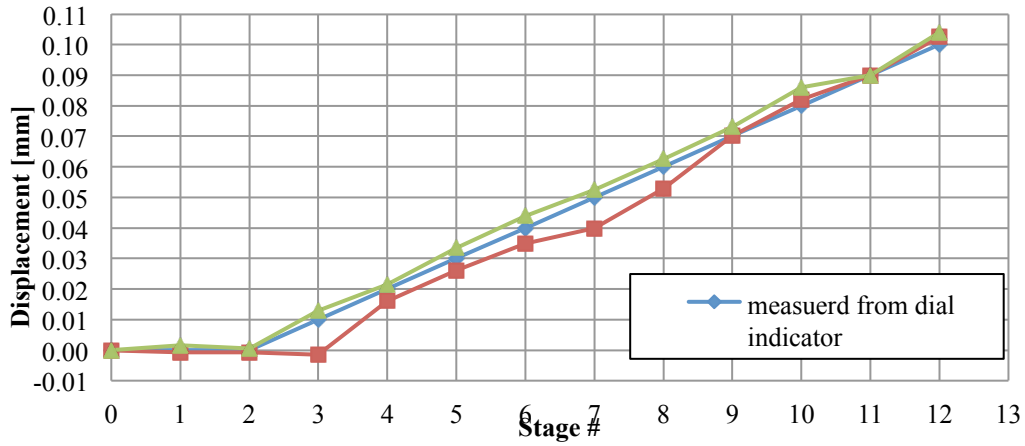

Fig. 71. Comparison of measured displacement results

7.1.2 Strain Accuracy and Field of View Test

The system, in its current configuration it is capable of measuring a 1.4 X 1.0m area in a single stage when positioned 1.75 m from the target surface. Fig. 72 shows the noise floor for in-plane surface strain overlaid on the measured surface. The measurement results show a strain range of (-) 53.7 to (+) 52.2 µm/m, comparable with the expected one, which is approximately +/- 50µm/m. These results confirm the usable measurement area with the newly developed wide-angle (8.5mm focal length) lens and camera configuration.

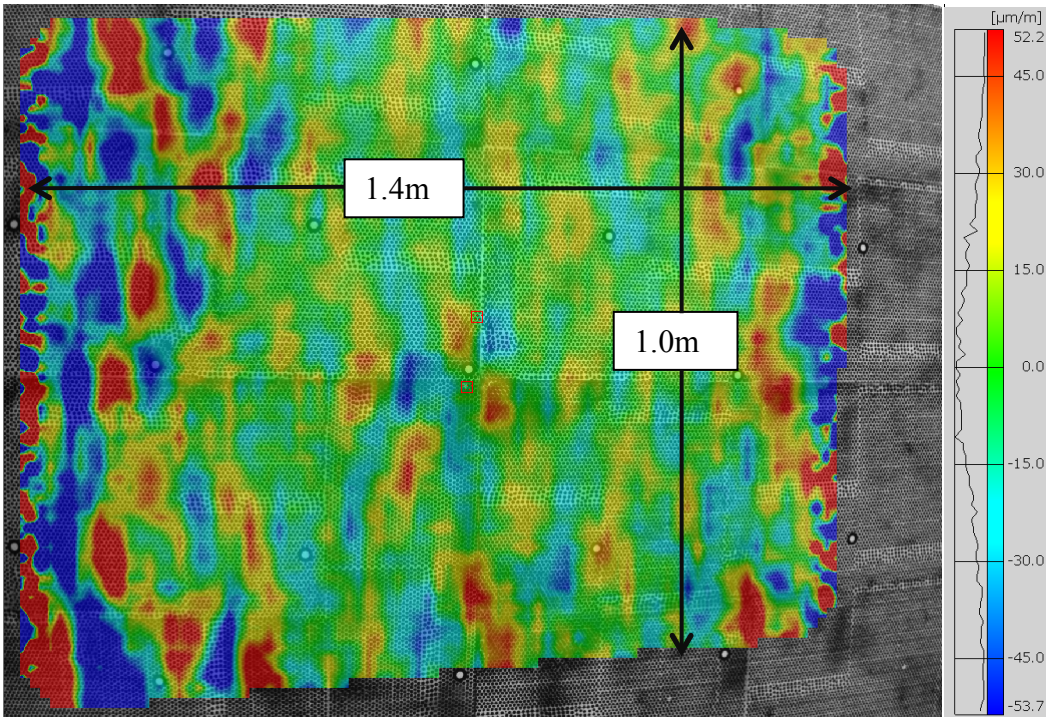

Fig. 72. Calibrated measurement area noise floor for strain

7.1.3 UAV Positioning Error Test

From measurement to measurement there will be some variation in the UAV's position relative to the target surface. To determine what effects this might have on results, measurements were taken of a 609.6 x 571.5 x 12.7 mm aluminum plate (Fig. 73) while the camera system was subjected to various translations and rotations on all the six degrees of freedom shown in Fig. 74). The measurements were repeatedly taken over a 48-hour period in a temperature and humidity controlled environment (+/-0.4 ºF, +/- 1.5%).

From the data reported, it is observed that extreme positive and negative pitch caused the noise floor for both strain and displacement to increase by an order of magnitude. Severe misalignments in pitch from the UAV are highly unlikely as the vehicle would no longer be stationary if rotated to such a degree. For these reasons, it should be recommended that the cameras were properly oriented when attached to the

UAV during measurement phases to prevent such issues. When scanning areas of more complex geometry (e.g. columns, junctions, etc.) a more intensive pre-test calibration can be performed to further reduce the possibility of additional errors.

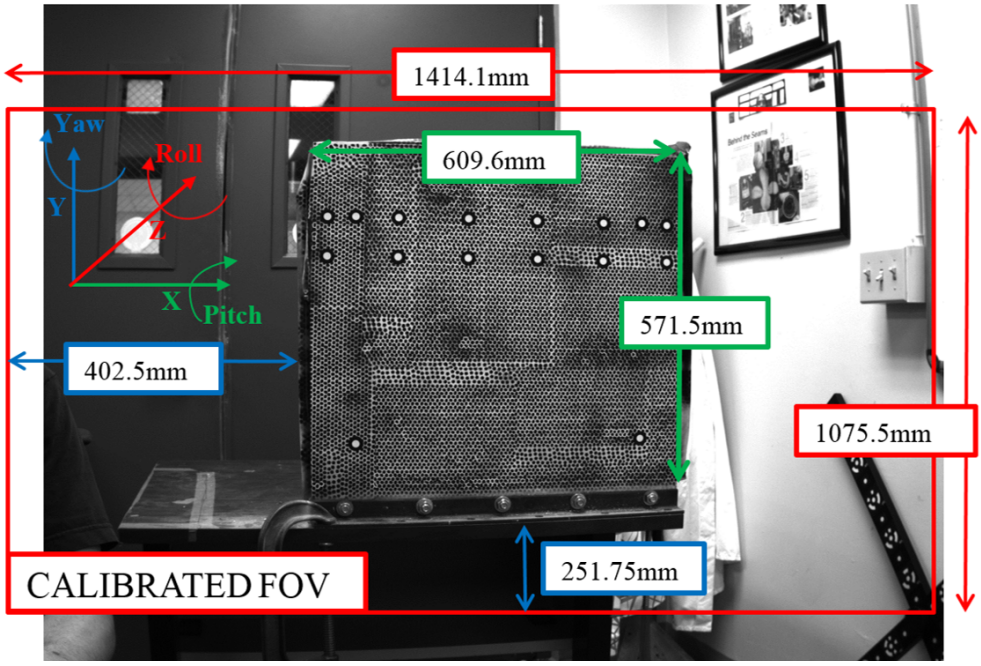

Fig. 73. 609.6 x 571.5 x 12.7 mm aluminum test plate

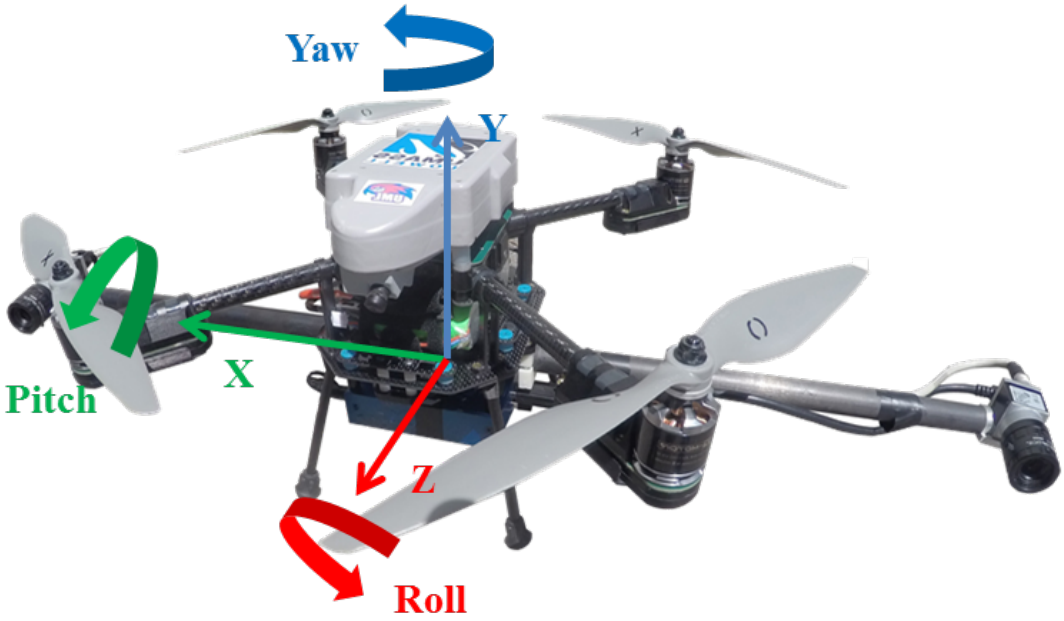

Fig. 74. UAV local coordinate system

7.2 Field Tests

The proposed CivilEye system has been evaluated by performing in-situ measurements on two in service bridges in the City of Lowell, MA. Test locations include those of previous work and new target areas with updated patterns for the CivilEye+DIC system and the CivilEye+Radar system. The individual inspection locations are detailed in the succeeding sections and follow the naming convention below:

Area ### - ###
↑ ↑
Bridge Number Area Number

Bridge Numbers:
#1 Lincoln Street Bridge
#2 Plain Street Bridge

7.2.1 Candidate Bridge: #1 Lincoln St. Bridge

A photograph of the Lincoln St Bridge is shown in Fig. 75. Additional details regarding this bridge are provided in Table 14.

Fig. 75. Bridge site # 1, L-15-074 Lowell Connector over Lincoln St.

Table 14. Bridge site L-15-074 Lowell Connector over Lincoln St. general information

City:	Lowell
Structure No.:	L15074-2HC-DOT-NBI
Facility Carried:	Lowell Connector
Feature Intersected:	Lincoln St.
Functional Class:	Freeway
Year Built:	1960
Year Rebuilt:	N/A
Structure Type:	Steel Stringer
Deck Type:	Concrete Cast-in-place
Br. Dept. No.:	L-15-074

The Lincoln St Bridge was selected for monitoring because it:

- Is easy to access, no lane closure required
- Has visually identifiable signs of degradation, spalling and corrosion
- Large expansion joints on bridge walls seasonally undergo fluctuating displacements and easily accessible
- Is at the end of the average bridge design life (56 years)
- Possesses a common construction type, steel stringers with cast-in-place concrete deck

7.2.2 Candidate Bridge: #2 Plain St. Bridge

A photograph of the Lincoln St Bridge is shown in Fig. 76. Additional details regarding this bridge are provided in Table 15.

Fig. 76. Bridge site #2, L-15-002 Plain St. over CSX Railroad

Table 15. Bridge site L-15-002 Plain St. over CSX Railroad General Information

City:	Lowell
Structure No.:	L15002-2N4-DOT-634
Facility Carried:	Plain St.
Feature Intersected:	CSX Rail Road
Functional Class:	Urban Minor Arterial
Year Built:	1993
Year Rebuilt:	N/A
Structure Type:	Prestressed Concrete Box Beam
Deck Type:	Concrete Precast Panels
Br. Dept. No.:	L-15-002

The Plain St. Bridge was selected for monitoring for the following reasons:

- Is easy to access, abandon railroad tracks under the bridge
- Cap and column sections provide a variety of geometry for the UAV to maneuver around while not flying across free flowing traffic.

- Is somewhat young in its designed lifespan (23 years)
- Possesses a common construction type, prestressed box girder

Within this work five areas were selected for monitoring on the Plain Street Bridge.

7.2.3 Monitoring Areas on All Bridges

A brief description of each monitoring area and its reason for selection are overviewed in Table 16.

Table 16. List of selected bridge monitoring areas

Monitoring Area	Observed Feature	Reason for Selection
1-1	Retaining Wall	Large Vertical Crack
1-2	Retaining Wall	Joint of Abutment and Retaining Wall
1-3	Abutment	Serious Spalling
1-4	Deck Underside	Corroded Internal Rebar
1-5	Abutment	Cracks in Abutment
1-6	Abutment	Corroded Internal Rebar & Cracks
1-7	Retaining Wall	Large Vertical Crack
1-8	Retaining Wall	Joint of Abutment and Retaining Wall
2-1	Abutment	Seam Between Retaining Walls
2-2	Abutment	Seam Between New and Old Abutment, Cold Joint
2-3	Deck Underside	Seam Between Box Girders
2-4	Bridge Pier	Vertical Crack
2-5	Abutment	Seam Between New and Old Abutment, Cold Joint
2-6	Abutment	Vertical Crack
2-7	Bridge Pier	Round surface, Possible Hairline Cracks Across Casting Line
2-8	Bridge Pier	Round surface, Possible Hairline Cracks Across Casting Line
2-9	Bridge Pier-Cap	Large Scan Area With Varying Geometry

7.2.3 Expansion Joint Monitoring

Inspected areas from previous work required a variety patterns to match the different test conditions caused by the variation in camera positions relative to the different inspection areas. Though the dot size of these patterns did not align with the specifications for the camera system used in this study; the optical targets adhered to the surfaces of the Lincoln St. Bridge were sufficient for this study.

As a reference to the accuracy of the DIC measurements, parallel brackets were adhered to opposing sides of the expansion joint between areas 1-2 and 1-8 (as shown in Fig. 77) and their changes in distance were measured using a 0.001-in. increment dial

caliper. Between May 11, 2016 and June 23, 2016 a contraction of 1.244 mm was physically measured between the two brackets.

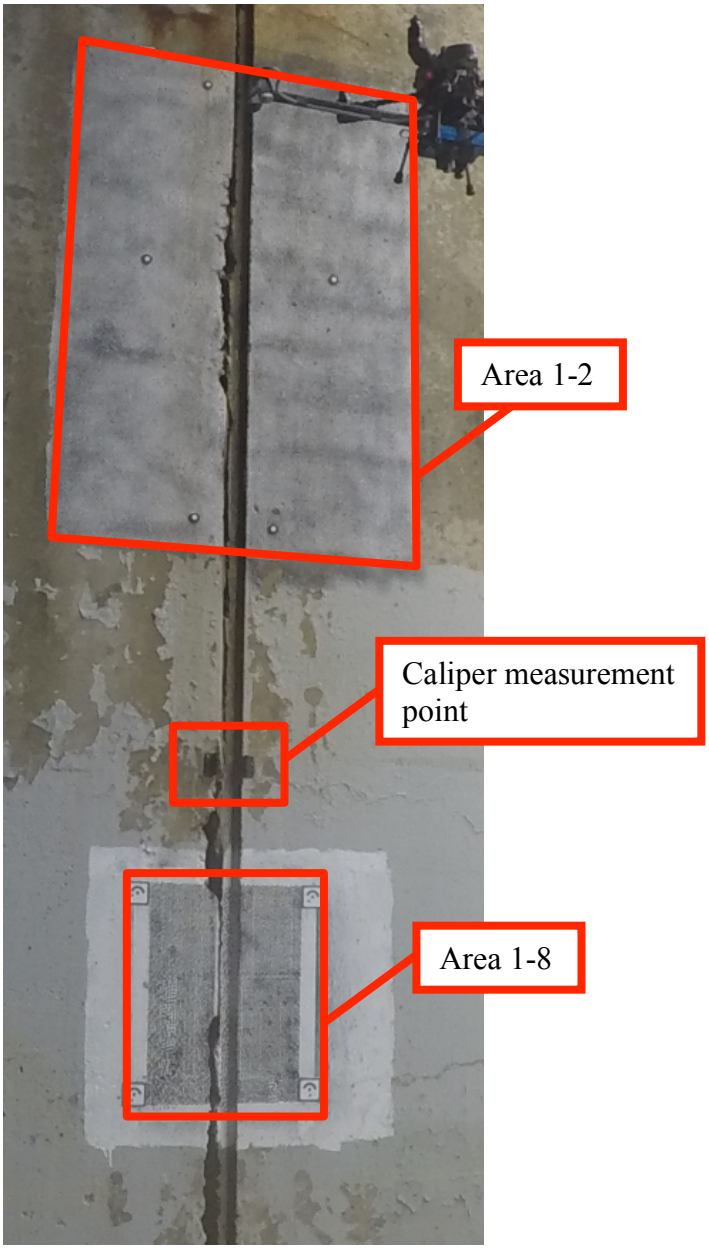

Fig. 77. Measurement locations along expansion joint at bridge site # 1, L-15-074 Lowell Connector over Lincoln St.

This direction of displacement is to be expected with an overall warming of the bridge occurring between the two measurements. Thus expanding the concrete structures and causing the joint to contract. The temperature profiles for each measurement date and time of each measurement are given in Fig. 78 for additional reference. The given temperature measurements were recorded form a nearby airport (Lawrence Municipal, North Andover, MA) and do not account for the direct solar heating of the bridge surface.

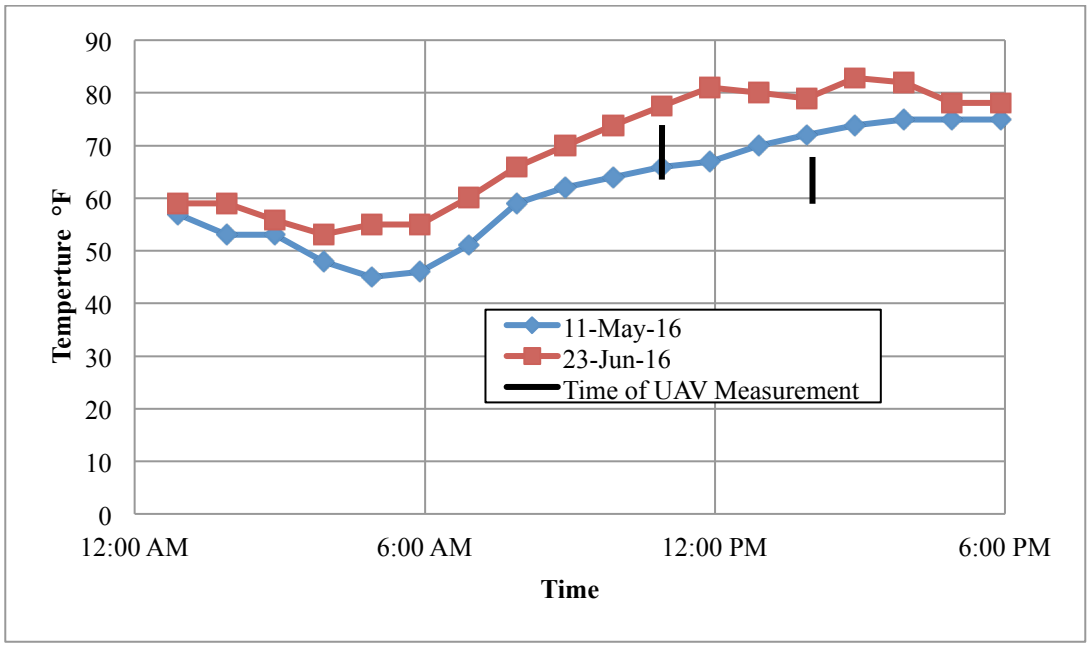

Fig. 78. Temperature profiles for measurement dates May 11, 2016 vs. June 23, 2016 as recorded from Lawrence Municipal Airport

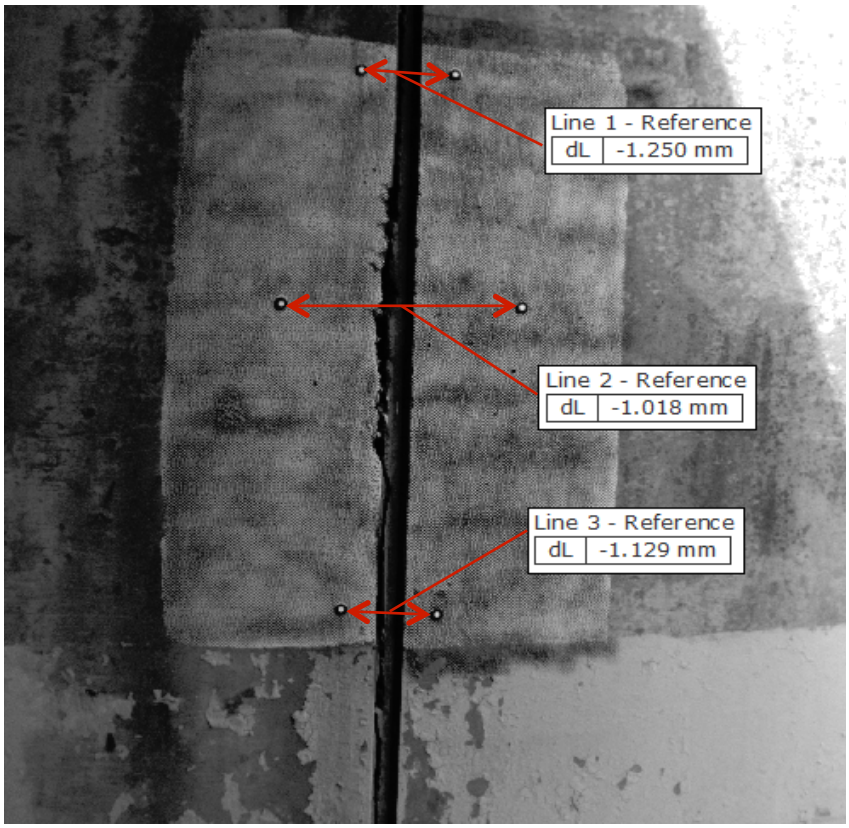

Fig. 79. Monitoring Area 1-2, Expansion joint displacement measured with 3D point-tracking. Monitoring period May 11, 2016 to June 23, 2016

The resulting displacements measured from the UAV using 3D point tracking are shown in Fig. 79. The displayed measurements are the absolute distance difference in 3D space between the point pairs as shown. Averaging the three displacement values results in a contraction approximation of 1.132 mm, as shown in Fig. 80, which is a 9.022% difference from the value measured from the calipers.

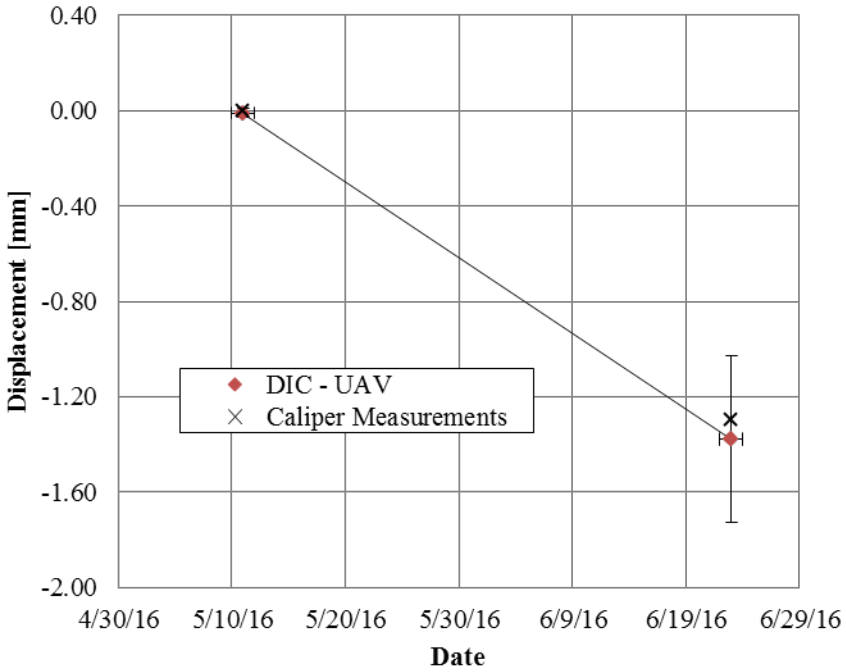

Fig. 80. Monitoring Area 1-2, Averaged extensometer displacement results from 3D point tracking measurements. Monitoring period May 11, 2016 to June 23, 2016

Area 1-8 was patterned specifically for the camera configuration used for the UAV payload and also utilizes optical target points which are measured in the same method as those used at Area 1-2. The four targets (shown in Fig. 81) were used to identify two optical extensometers (Lines 1 and 2) and define a local coordinate system for the inspection area. When collecting full field CivilEye+DIC data, defining a local coordinate system can be used to acquire horizontal displacement values from arbitrary full-field data points, this method is utilized for Lines 3-5 as shown in Fig. 81. The displacement results of the measurements performed along the expansion joint from May 11, 2016 to June 23, 2016 are given in Table 17.

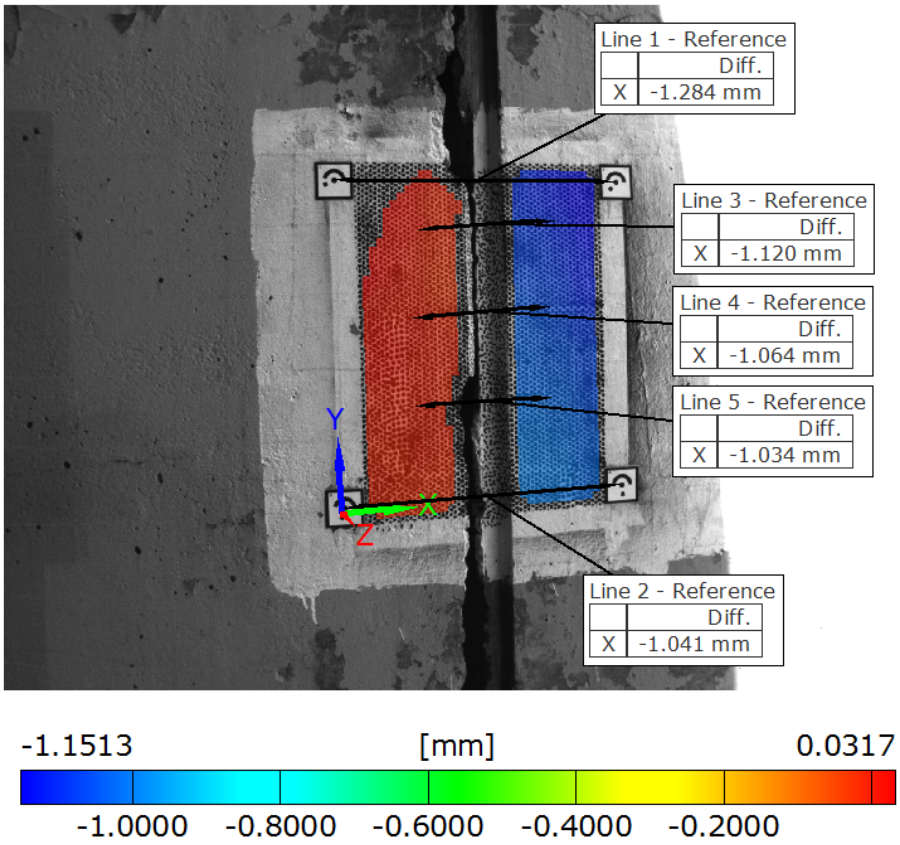

Fig. 81. Monitoring Area 1-8, Expansion joint displacement measured with 3D point-tracking and full field data. Monitoring period May 11, 2016 to June 23, 2016

Table 17. Expansion Joint displacement measurements May 11, 2016 to June 23, 2016

Technique	Target Area	Data Acquisition Environment	Displacement [mm]	% Difference From Caliper
Caliper	1-2 / 1-8	Hand Measurement	-1.244	0.000
Optical Targets	1-2	In-flight	-1.132	9.022
Optical Targets	1-8	In-flight	-1.383	11.168
Full Field Points	1-8	In-flight	-1.121	9.906
Optical Targets	1-8	Handheld	-1.163	6.524
Full Field Points	1-8	Handheld	-1.070	13.980

From data summarized in Table 17, it is observed that the maximum error in the compared measurements is nearly 10%, and the same errors characterize both the measurements performed as the DIC system is attached to the UAV or handheld. This can be considered a further demonstration of the low impact the UAV has on the measurements. Indeed, from the analysis of those data, it is suggested that the principal causes affecting the measurements accuracy are parameters like the lights and shadows, rather than the movement of the cameras.

7.2.4 Long Term Monitoring at Lincoln St. Bridge

The first bridge utilized for the long term monitoring study is the Lowell Connector over Lincoln St. Bridge. The 56-year-old concrete cast-in-place bridge is close to its designed lifespan with obvious signs of degradation, spalling, and corrosion. It also has large expansion joints on its walls that are undergo regular thermal expansion and contraction. Four locations targeted at monitoring two expansion joints and a large pre-existing crack were continuously monitored over the course of 10 months. The location and designation of each target area monitored in the study are highlighted in Fig. 82.

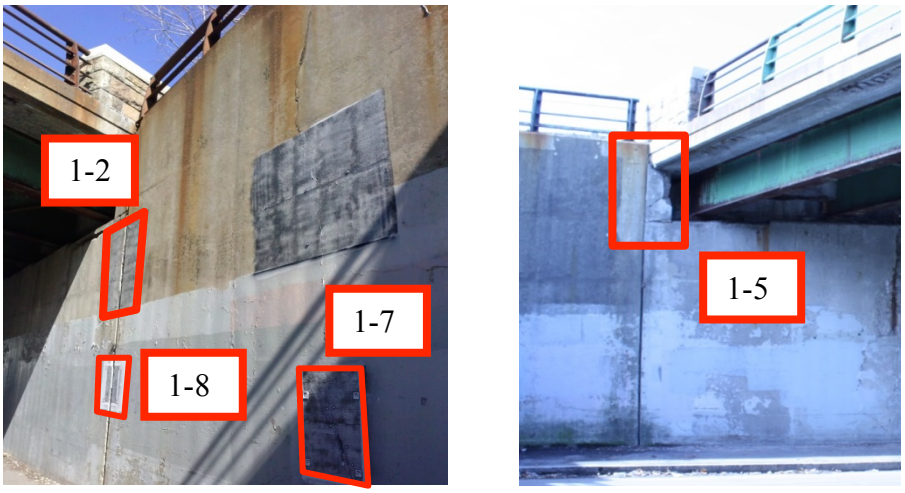

Fig. 82. Inspection areas at bridge site #1 – Lowell Connector over Lincoln St.

To supplement the measurement timeline the stereovision system would be positioned by hand to acquire measurements if the UAV was between prototype phases or otherwise unavailable. This allowed for a combined eight measurements to be performed on areas 1-7 and 1-8 over the 10-month period. While for areas 1-2 and 1-5 three measurements were performed with the assistances of the UAV. The measurement dates and method of positioning the stereovision payload are detailed in Table 18.

Table 18. Measurement dates and camera positioning method for Lincoln St. Bridge

		Measurement Dates								
		0 (Ref)	1	2	3	4	5	6	7	8
Lowell Connector over Lincoln St.	1-2	5/11/16	6/23/16	10/18/16						
	1-5	5/11/16	6/23/16	10/18/16						
	1-7	1/7/16	2/1/16	2/17/16	4/11/16	4/21/16	5/11/16	6/16/16	6/23/23	10/18/16
	1-8	1/7/16	2/1/16	2/17/16	4/11/16	4/21/16	5/11/16	6/16/16	6/23/23	10/18/16

Measurement Condition		
UAV	Handheld	Both

7.2.5 Lincoln St. Bridge Expansion Joints

Inspections performed at area 1-2 utilized optical targets previously placed as individual pairs on opposing side of the expansion joint. Fig. 83 shows the portion of the joint investigated with the three extensometer lines used for calculating the relative motion of the two concrete abutments. For area 1-2 all measurement images were acquired using the UAV to position the cameras. The target area is approximately 10 feet above ground level.

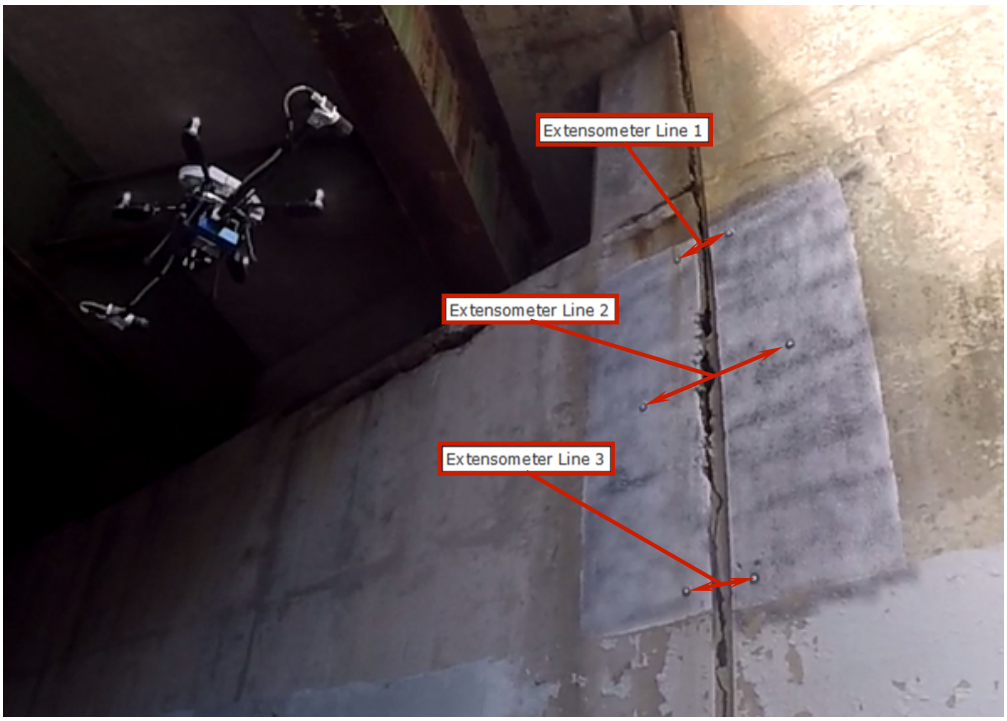

Fig. 83. Monitoring Area 1-2, Extensometer locations across expansion joint

To further validate the accuracy of the measurements performed using the proposed CivilEye+DIC systems, a back-to-back comparison with a 0.001-in graduation dial caliper has been performed by comparing the discrete displacement recorded from the images. Fig. 84 shows the results from the individual optical extensometers compared with caliper measurements over a monitoring period of six months. For these results each point represents the average of five measurement stages taken at each date and the error bars shown are the standard deviation ranges of those results.

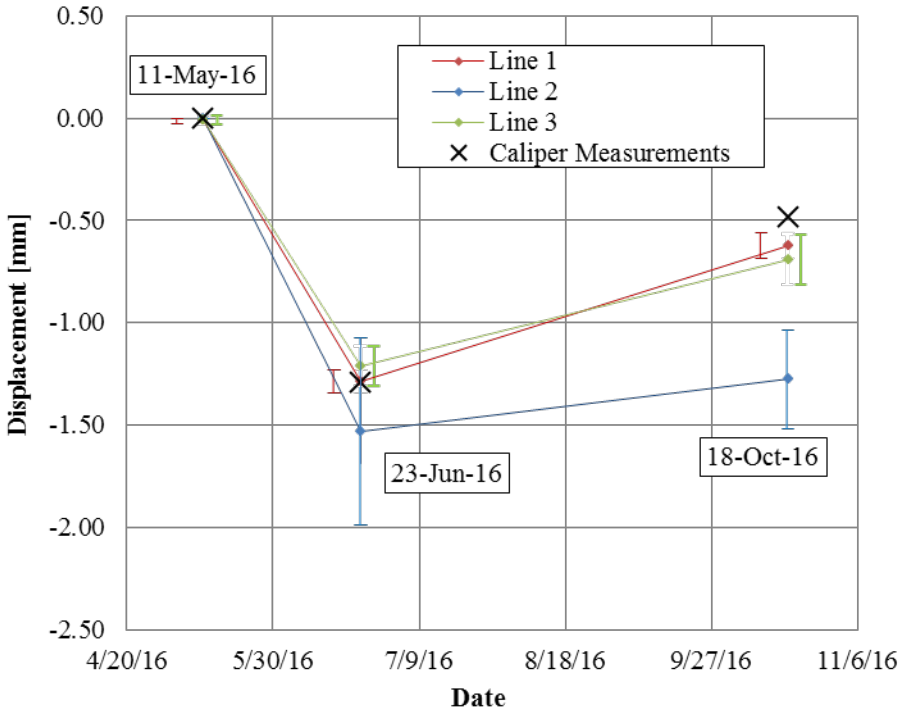

Fig. 84. Monitoring Area 1-2, averaged displacement results from individual optical extensometers. Monitoring period May 11, 2016 to October 18, 2016

Despite the limited number of available measurements, an excellent agreement is observed between the displacement recorded using the CivilEye+DIC system and the caliper. In particular, the average relative error between the data measured using the CivilEye+DIC system and the caliper is equal to 15%, consistent with previous results. For extensometer line two at area 1-2 the higher discrepancy between CivilEye+DIC and caliper measurement is partially the result of an interfering shadow as previously described. These results imply that the CivilEye+DIC system can measure the relative displacement of a point with accuracy comparable to that of traditionally used instrumentation over a wide area, a further demonstration of the validity of the proposed approach.

Area 1-5 (shown in Fig. 85) is located across Lincoln St. opposing area 1-2. Similarity; data from this inspection area is collected by measuring the changes in relative position between optical targets placed on across the expansion joint (see Fig. 86) and a large (~2-5mm) local crack. Flight inspections of the crack and joint widths were performed at three dates (May 11th, 2016, June 23rd, 2016, and October 18th, 2016). These results show a similar trend to the activity measured at area 1-2, a contraction at the joint during the transition from spring to summer followed by an expansion during the transition from summer into fall. The error bars shown in Fig. 87 represent the standard deviation range for five measurements taken at each of the 3 extensometer lines. It is presumed these displacements are primarily resulting from the thermal expansion and contraction of the concrete abutments.

Fig. 85. UAV inspection being performed at monitoring area 1-5, Test date June 23, 2016.

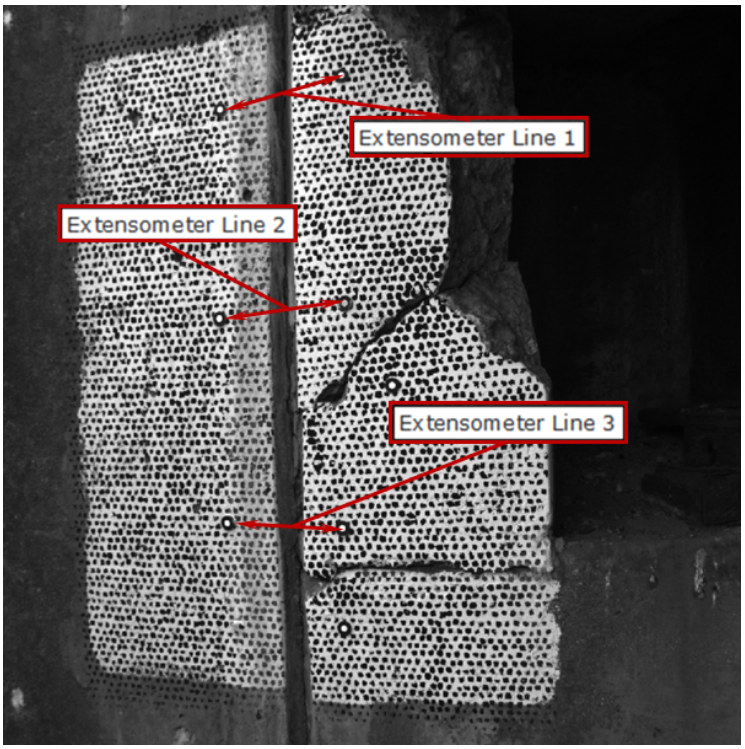

Fig. 86. Monitoring Area 1-5, Extensometer locations 1-3 across expansion joint

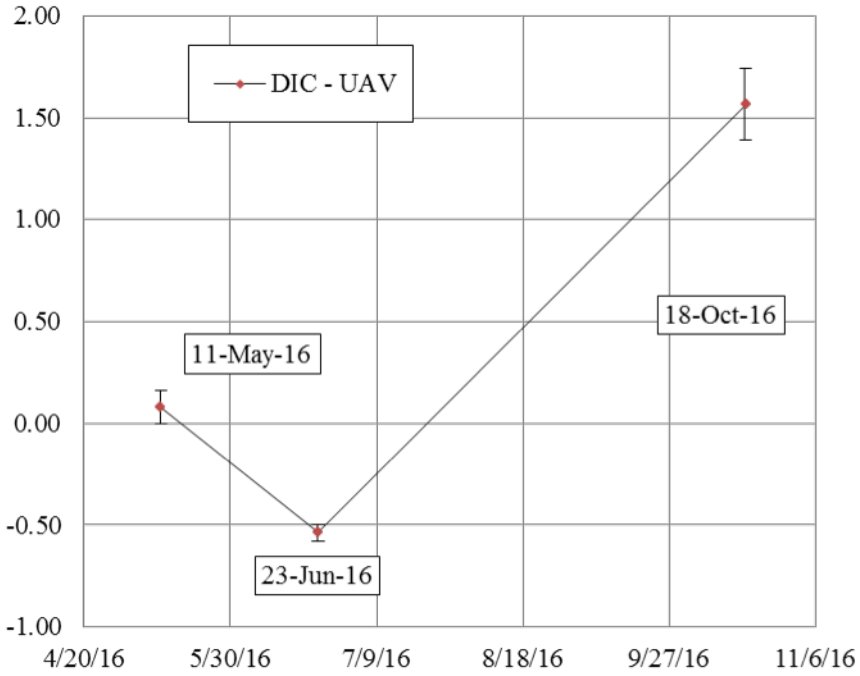

Fig. 87. Monitoring Area 1-5, averaged extensometer displacement results from multiple 3D point tracking measurements. Monitoring period May 11, 2016 to October 18, 2016

The measurement dates and camera positioning method (UAV) for area 1-5 are in line with that of area 1-2. Similarly the trends of expansion and contraction for the two joint are in agreement. Though the magnitudes of each displacement are unique to each location, both undergo a clear contraction from May 11, 2016 to June 23, 2016 then an expansion between June 23, 2016 and October 18, 2016.

As previously shown, area 1-8 is located below area 1-2 along the same abutment expansion joint. Due to the accessibility of this inspection area a total of nine inspections were performed over a period of 285 days. Three of the inspections utilized the UAV (as shown in Fig. 88) while the additional six were performed with the payload being held by an inspector and powered by an external battery pack. A screenshot of the full-field displacement profile is shown in Fig. 89.

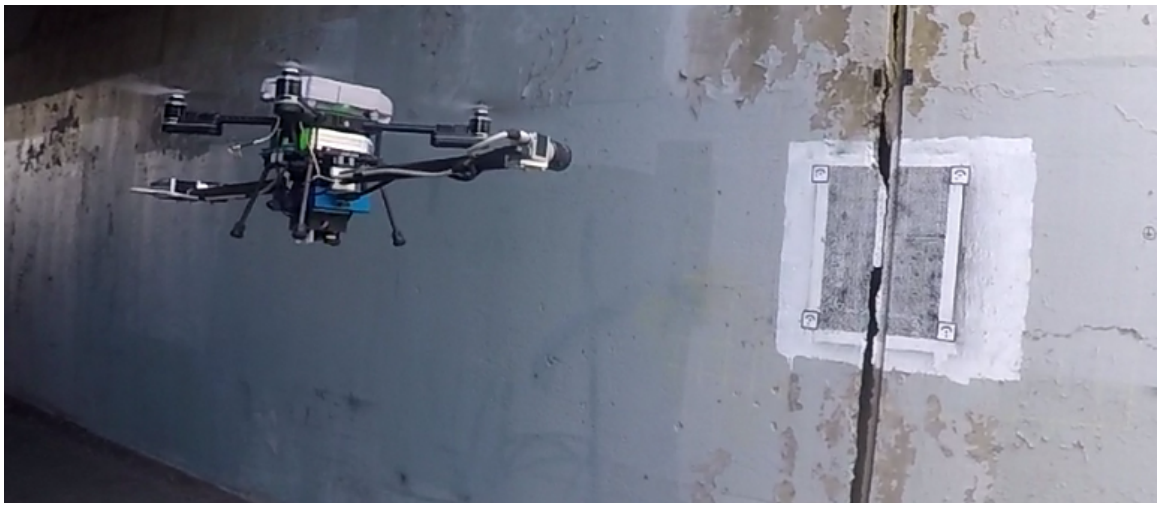

Fig. 88. UAV inspection being performed at monitoring area 1-8, Test date June 23, 2016.

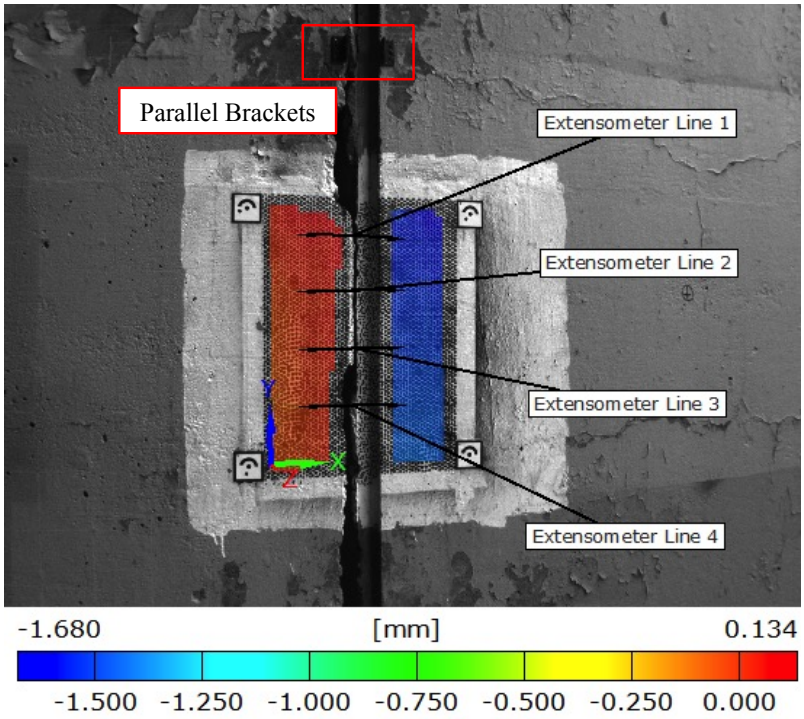

Fig. 89. Monitoring Area 1-8, full-field X-displacement contour plot and extensometer locations. Monitoring period January 7, 2016 to June 16, 2016

For the long-term monitoring of the expansion joint at area 1-8 full-field data was generated. When full-field data is collected, any pair of points may be selected to create an optical extensometer. The timeline of expansion and contraction at the joint was estimated and plotted in Fig. 90 from the extensometers as shown in Fig. 89.

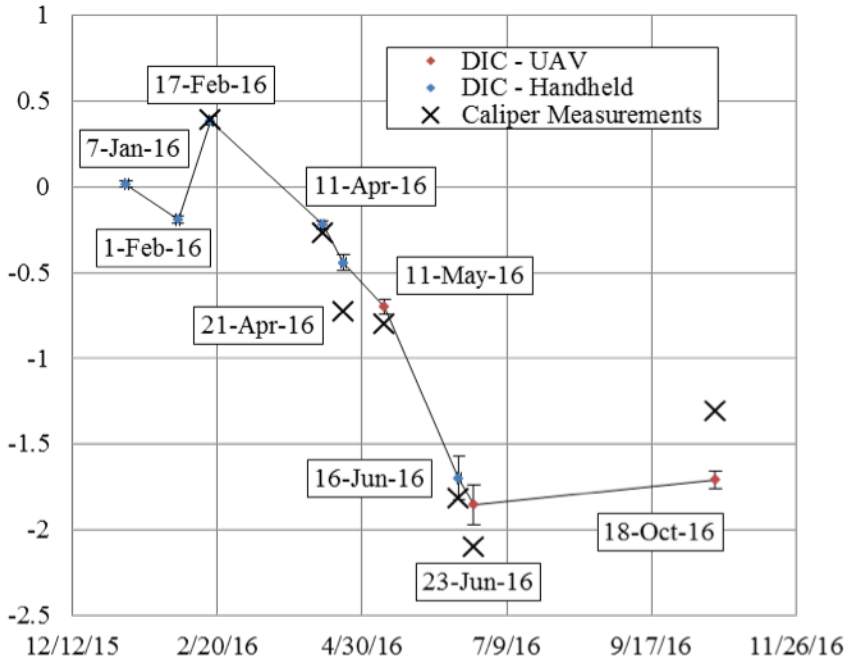

Fig. 90. Monitoring Area 1-8, averaged extensometer displacement results from CivilEye+DIC measurements. Monitoring period January 7, 2016 to October 18, 2016

It is noted that there is average error of 17.12 % between the displacements measured using CivilEye+DIC and what was measured with dial calipers. However it is also noted that these differences are each less than 1 mm in magnitude and that the measurement system is still highly capable of achieving a level of accuracy relevant to infrastructure monitoring.

7.2.5 Lincoln St. Bridge Surface Cracks

In addition to the optical targets placed for monitoring the activity across the expansion joint, target points were placed on opposing sides of larger (~ 2-4 mm) cracks located along the adjacent wall. The resulting extensometer lines are shown in Fig. 91. The displacements measured across extensometer lines 4 and 5 are an order of magnitude below those recorded from lines 1, 2 and 3 and are presented in Fig. 92.

The crack measurements performed at area 1-5 were acquired using the UAV to position the camera pair and the data was extracted from the same images used to determine and expansion and contraction of the expansion joint. Similar to the expansion joint, the cracks separating the concrete section show an activity pattern of a contraction followed by an expansion through the three measurements.

In conjunction with the expansion joint at area 1-8, area 1-7 has was monitored for nearly 10 months to assess the capabilities of the proposed CivilEye+DIC system in characterizing the activity of micro-cracks over time and their expansion rate. These

measurements were a collaboration of both hand held and UAV (shown in Fig. 93) based inspections as outlined in Table 18. Fig. 94 shows the extensometer locations utilized for long term monitoring and the full-field X-displacement contour plot representing the surface activity shift between January 7, 2016 and April 21, 2016.

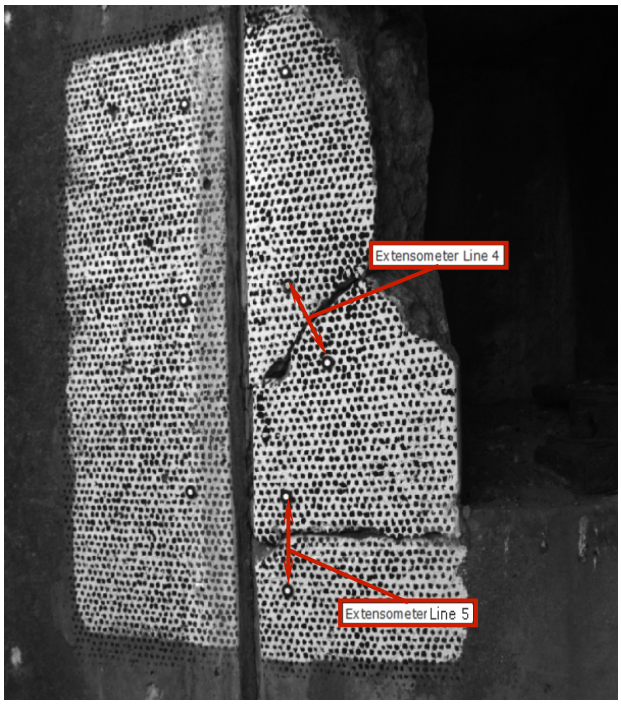

Fig. 91. Monitoring Area 1-5, extensometer locations 4 and 5 across large cracks

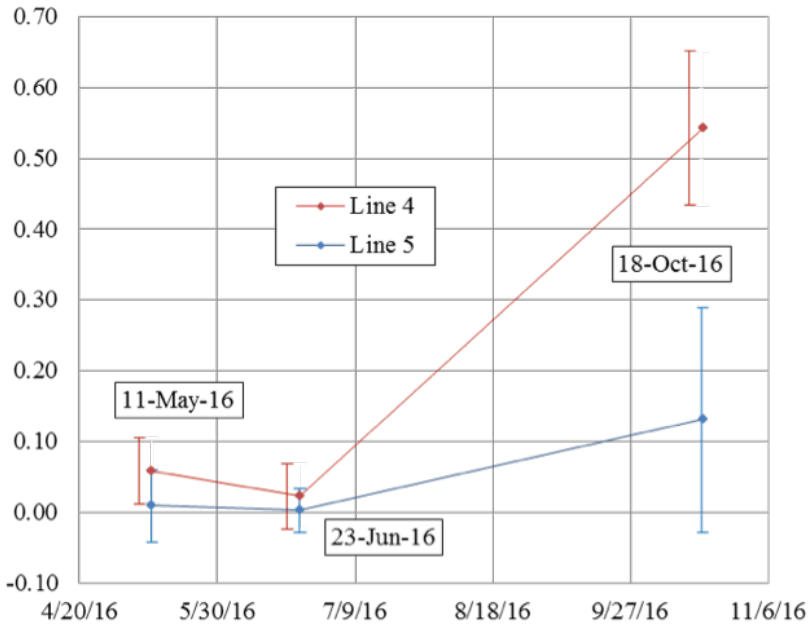

Fig. 92. Monitoring Area 1-5, averaged extensometer displacement results from 3D point tracking measurements. Monitoring period May 11, 2016 to October 18, 2016

Fig. 93. UAV inspection being performed at monitoring area 1-7, Test date June 23, 2016.

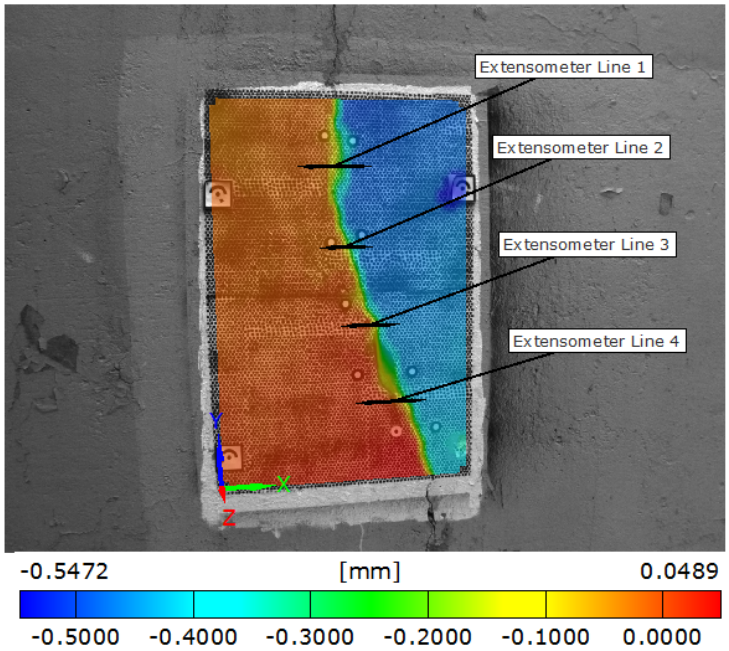

Fig. 94. Monitoring Area 1-7, full-field X-displacement contour plot and extensometer locations. Monitoring period January 7, 2016 to April 21, 2016

Fig. 95 shows the change in the length of the four considered extensometer lines over time and the associated error evaluated as the average of the five images recorded in each measurement. The monitoring activity to which the plot refers to has been performed between January, 7th and October, 18th 2016.

The results show that the crack tends to contract through the whole winter period and the beginning of the summer, while an opposite trend is shown in the warmest months. In particular, it should be pointed out that the first five measurements (until April, 21st) were performed using a handheld configuration, while the others were

performed using the CivilEye+DIC system. From an analysis of the recorded data, it is possible to observe that the system is able to detect displacement as small as $9 \cdot 10^{-5}$ m and that the accuracy of the measurements performed as the UAV is employed is not dissimilar from that of the measurements performed with the handheld configuration.

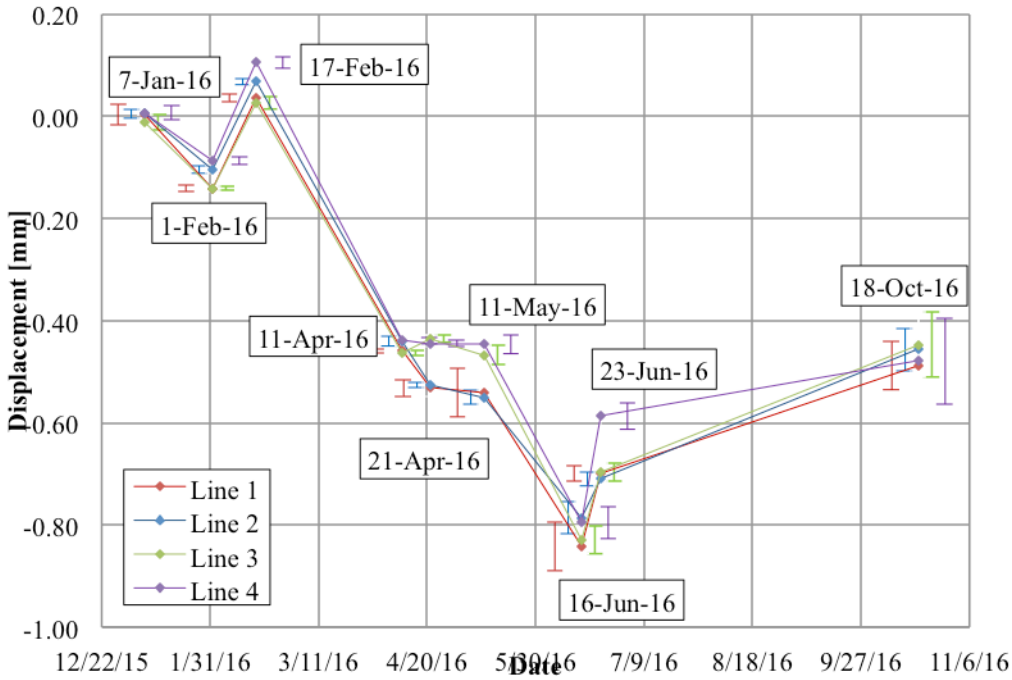

Fig. 95. Monitoring Area 1-7, averaged displacement results from individual optical extensometers. Monitoring period January 7, 2016 to October 18, 2016

7.2.6 Long Term Monitoring at Plain St. Bridge

The second bridge site (DOT designation L-15-002) has an abandoned CSX railroad track running below it. It is a 23-year-old prestressed concrete box girder bridge. It has several areas characterized by sub-millimeter crack activity. The two investigated areas detailed in this chapter, together with their relative positions on the bridge and additional inspection locations detailed in Fig. 96 and the inspection timelines are detailed in Table 19.

Fig. 96. Inspection areas at bridge site #2 – Plain St. over CSX Railway

Table 19. Measurement dates and camera positioning method for Plain St. Bridge

		Measurement Dates									
		0 (Ref)	1	2	3	4	5	6	7	8	9
Plain St. Over CSX Railway	2-5	11/30/15	1/7/16	2/1/16	2/17/16	3/10/16	4/11/16	4/21/16	4/16/16	5/11/16	10/18/16
	2-6	2/1/16	3/10/16	4/21/16	6/23/16	10/18/16					
	2-7	11/30/15	1/7/16	2/17/16	4/11/16	4/21/16	6/16/16				
	2-8	11/30/15	1/7/16	2/17/16	4/11/16	4/21/16	10/18/16				
	2-9	2/1/16	3/10/16	4/21/16	6/23/16	10/18/16					

Measurement Condition		
UAV	Handheld	Both

7.2.7 Plain St. Bridge Surface Cracks

Long term monitoring was performed at area 2-5 documenting the activity across a vertical hairline crack on the bridge abutment. Due to the ease of accessibility both handheld and UAV inspections (as shown in Fig. 97) were performed. Fig. 98 shows the extensometer locations utilized for long term monitoring and the full-field X-displacement contour plot representing the surface activity shift between November 30, 2015 and April 11, 2016.

As usual, for each of the considered measurements, five image pairs were acquired to allow for post-processing averaging. Furthermore, in the data plotted in Fig. 99, only those recorded on March 10th and October 18th were measured using the CivilEye+DIC system, while the others were acquired as the system was held in hand by the inspector.

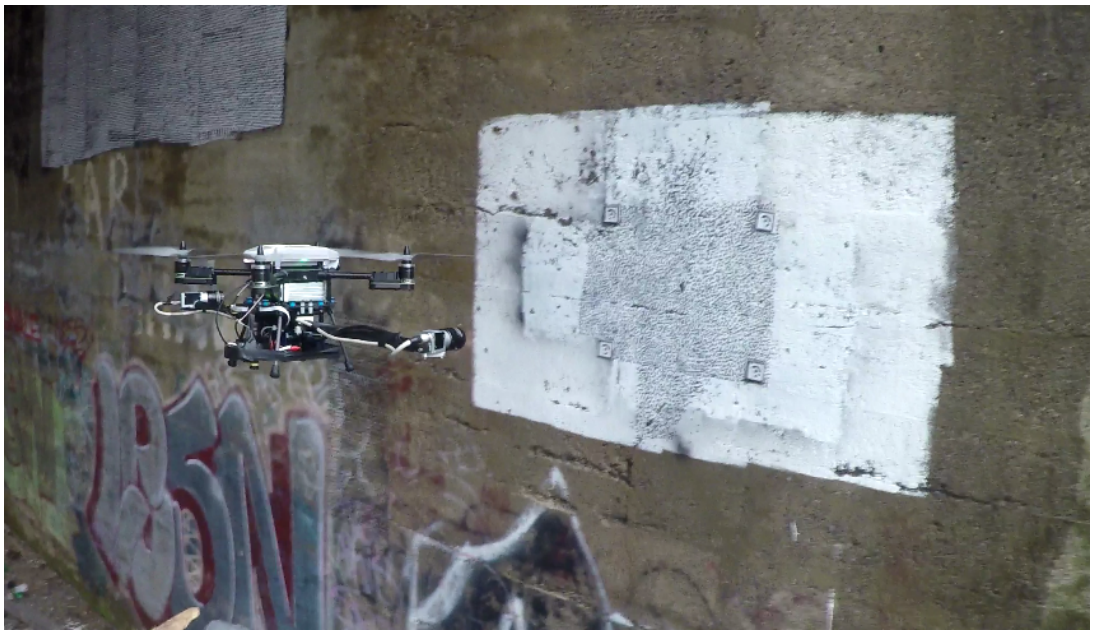

Fig. 97. Flight inspection in operation at area [2-5] at bridge site L-15-002 Plain St. over CSX Railroad

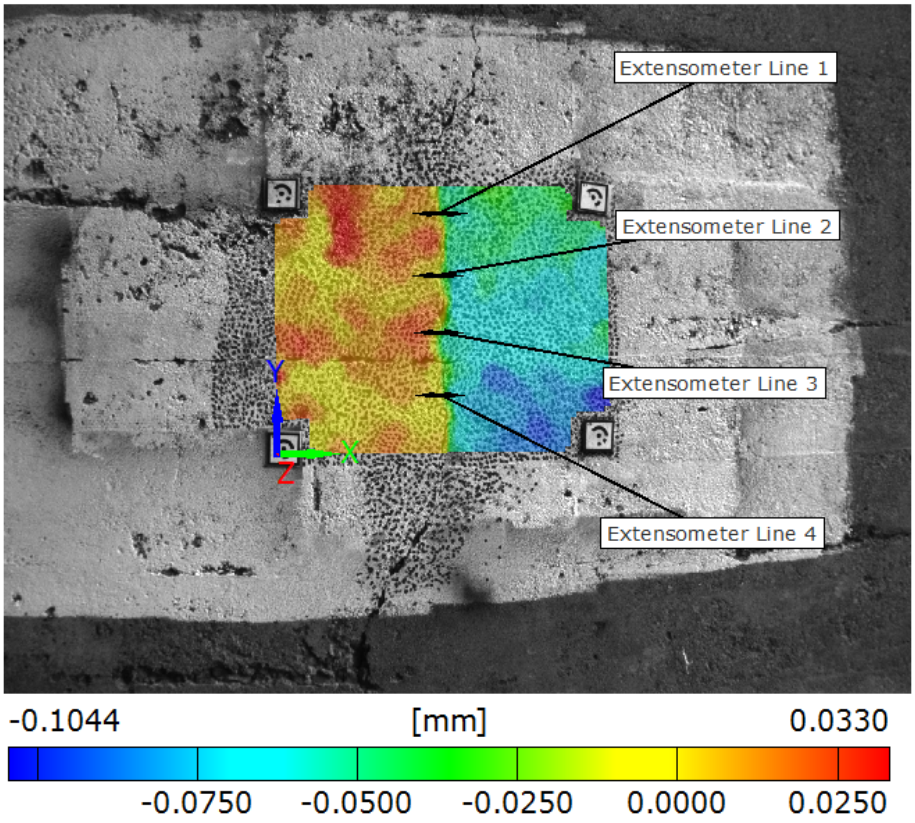

Fig. 98. Monitoring Area 2-5, full-field X-displacement contour plot and extensometer locations. Monitoring period November 30, 2015 to April 11, 2016

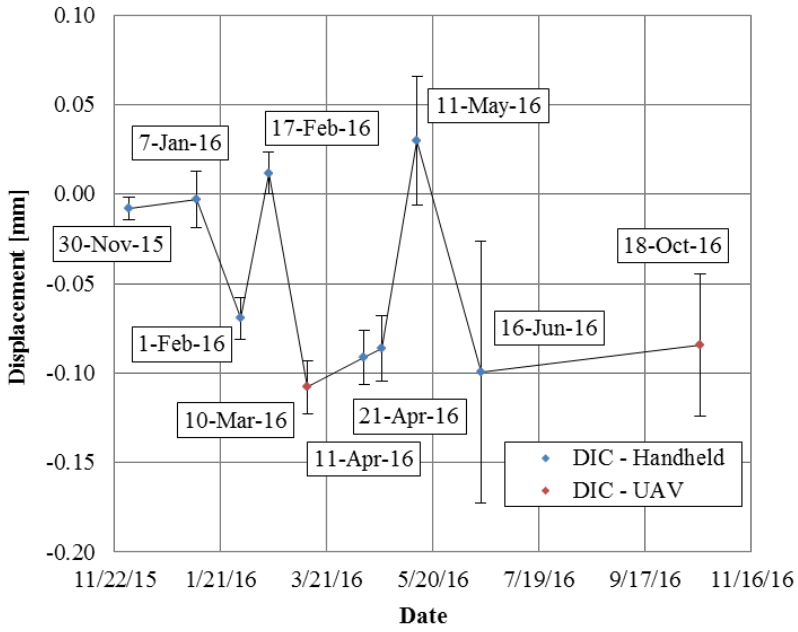

Fig. 99. Monitoring Area 2-5, averaged extensometer displacement results from CivilEye+DIC measurements. Monitoring period November 30, 2015 to October 18, 2016

The second is the inspection of a vertical crack on a section of the abutment right below the bridge's deck nearly five meters above street level. Fig. 100 shows the extensometer locations utilized for long term monitoring and the full-field X-displacement contour plot representing the surface activity shift between February 1, 2016 and March 10, 2016. The displacement results across the visible crack are detailed in Fig. 101.

With regard to data plotted in Fig. 99, the measurements performed on March 1st, June 23rd, and October 18th were accomplished with the payload attached to the UAV. As is it possible to observe from both data sets, the system is capable of tracking the relative motion of the two edges of the cracks with a degree accuracy suitable for civil applications, both for micro-displacement (on the order of 10^{-4} m or smaller) and larger fractures (on the order of millimeters). Measurement errors do not depend on the kind of supporting technique as they are equal to $2.4 \cdot 10^{-5}$ m and $2.7 \cdot 10^{-5}$ m for the handheld case and the UAV respectively in the first set of data and equal to $7.0 \cdot 10^{-5}$ m and $3.6 \cdot 10^{-5}$ m for the handheld case and the UAV respectively in the second set of data. Therefore, more than the stability of the whole system to vibration and movements, optimal exposure time and lighting conditions are parameters that should be prioritized for ensuring good quality measurements.

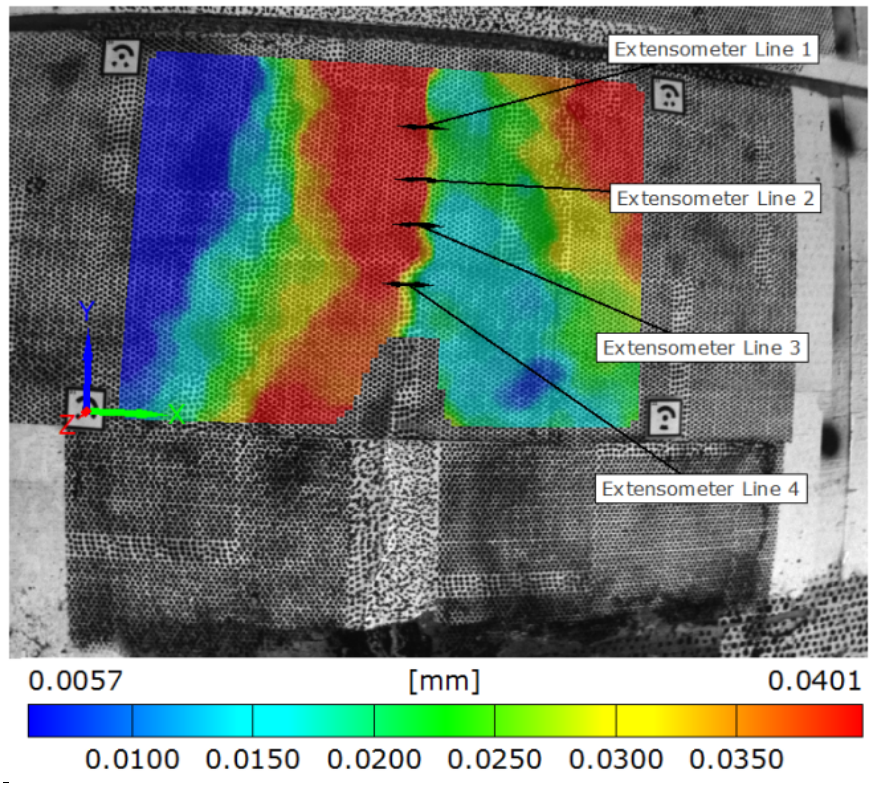

Fig. 100. Monitoring Area 2-6, full-field X-displacement contour plot and extensometer locations. Monitoring period February 1, 2016 to March 10, 2016

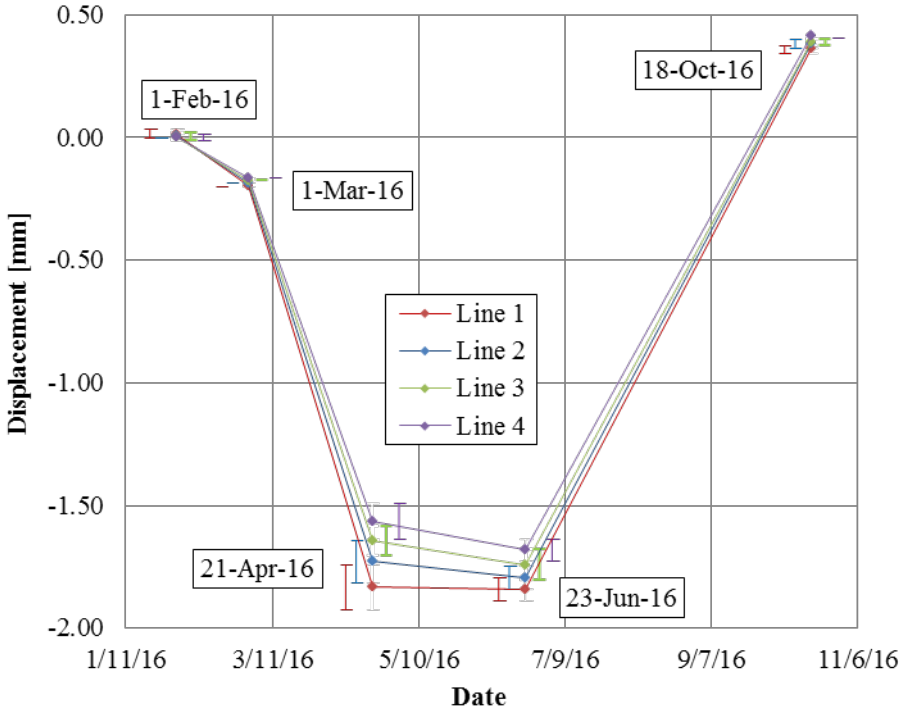

Fig. 101. Monitoring Area 2-6, averaged displacement results from individual optical extensometers. Monitoring period February 1, 2016 to October 18, 2016

7.2.8 Lincoln St. Bridge Subsurface Radar Imaging

The subsurface radar imaging result on Lincoln St. Bridge (Lowell, MA) is reported in this section, along with the integrated 3D point cloud modeling. Fig. 102 shows our field validation of the CivilEye+Radar system at Lincoln St. Bridge.

In this field test, three locations were chosen to understand the effect of i) surface irregularity (e.g., surface indentation), ii) surface cracks, and iii) subsurface steel rebar on SAR images of RC bridges. Fig. 103 shows the effect of surface irregularity on SAR images. Fig. 104 shows the effect of surface cracking on SAR images. Fig. 105 shows the effect of subsurface steel rebars on SAR images.

Fig. 102. Field validation of the CivilEye+Radar system at Lincoln St. Bridge, Lowell, MA

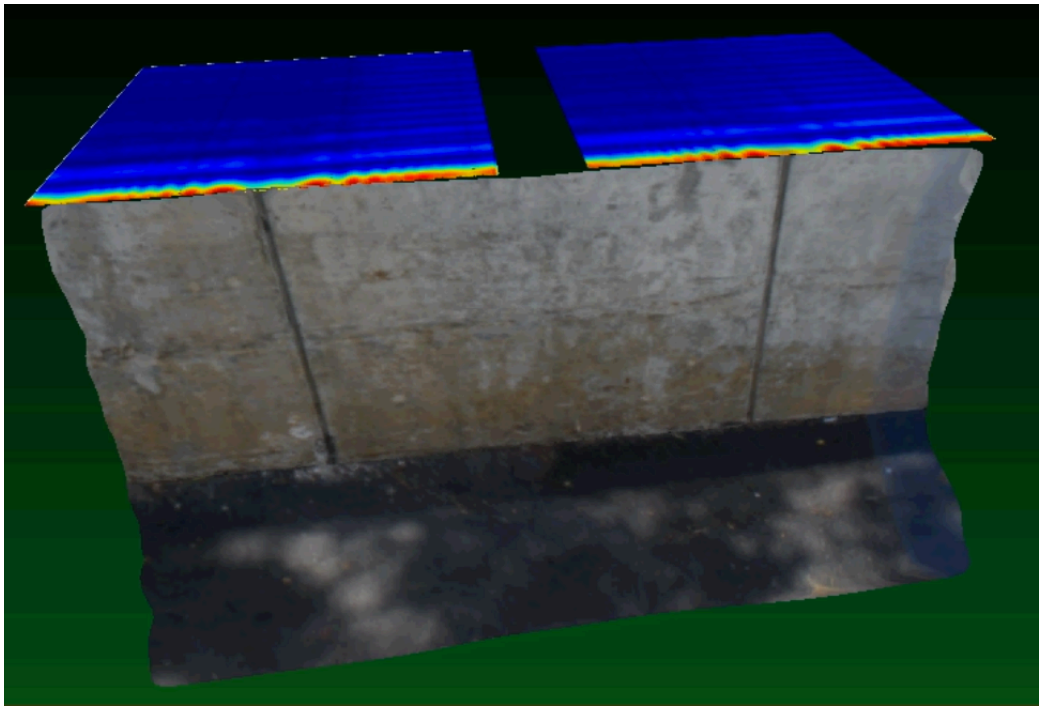

Fig. 103. Integrated 3D radar image – Effect of surface irregularity

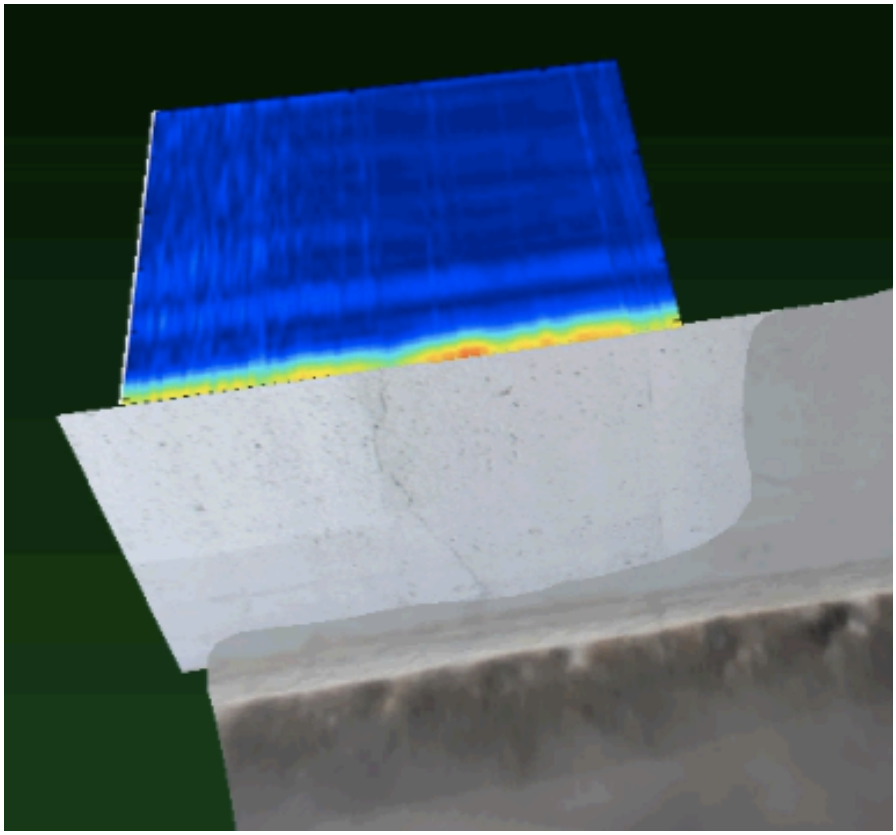

Fig. 104. Integrated 3D radar image – Effect of surface cracking

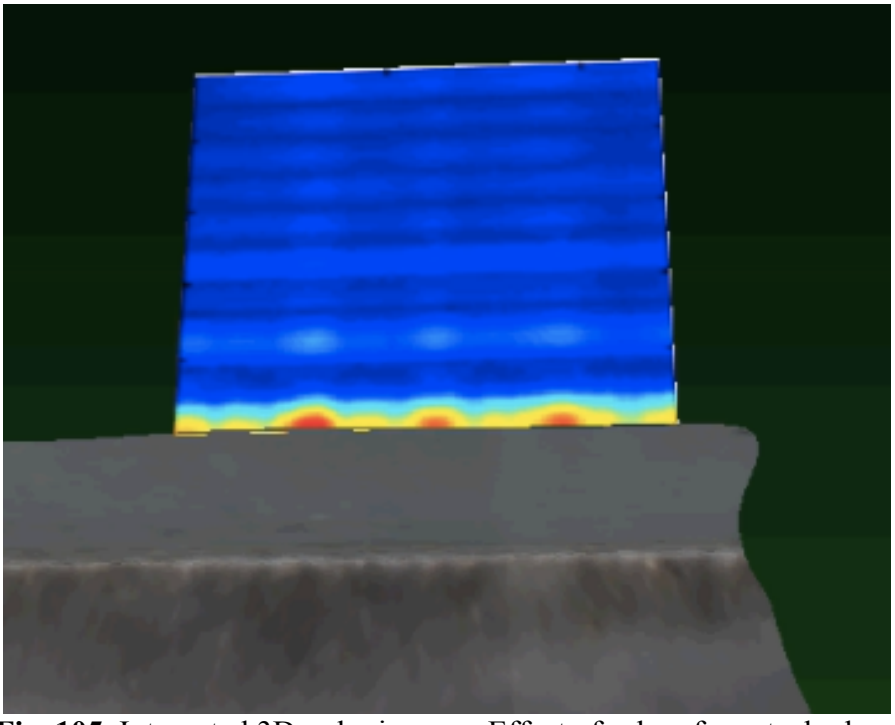

Fig. 105. Integrated 3D radar image – Effect of subsurface steel rebars

In Fig. 103, it was found that the presence of surface irregularity (in this example, an indentation) scatters away the incident radar signals, resulting in reduced SAR amplitudes. Such effect can also be induced by the presence of surface cracks in concrete, as shown in Fig. 104. On the other hand, the presence of subsurface steel rebars can amplify the intensity of returned radar signals, resulting in increased SAR amplitudes as shown in Fig. 105.

Fig. 106. Integrated 3D radar image with mechanical strength of concrete, Lincoln St. Bridge

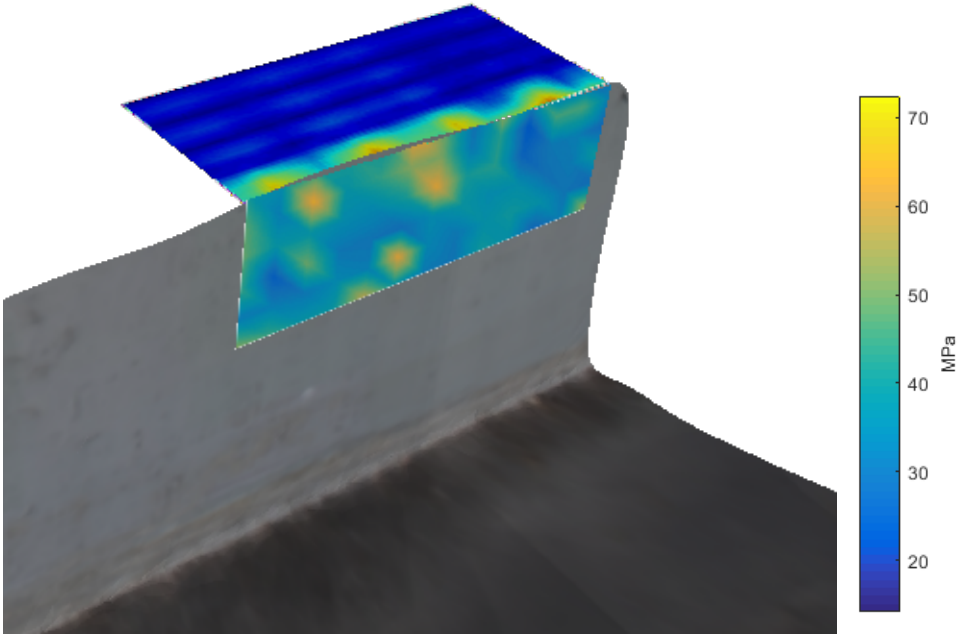

Fig. 107. Integrated concrete surface strength with subsurface radar image at Lincoln St. Bridge

To further explore the meaning of SAR image for condition assessment of concrete structures, we also conducted a survey on the mechanical strength of concrete abutment at Lincoln St. Bridge. A commercially available rebound hammer (SilverScchmidt by Proceq) was used in this survey. Figs 106 and 107 illustrate the integrated 3D point cloud model of the bridge with both SAR images and surface strength distribution images. From the integration between SAR images and mechanical strength distribution, it is found that the SAR amplitude of weak concrete is higher than the one of strong concrete. This can be explained by the moisture content of concrete since wet concrete has lower mechanical strength than dry concrete. Consequently, wet concrete produces higher SAR amplitudes, due to the high effective dielectric constant of wet concrete.

Chapter 8. Project Dissemination and Commercialization Plan

8.1 Project Dissemination

We have created a project website (http://faculty.uml.edu/tzuyang_yu/USDOT_QUAV.aspx) to disseminate our research activities and findings to the transportation community. Fig. 106 shows the screen shot of our project website. We have delivered 14 conference presentations and published two journal papers with many journal manuscripts submitted/under review. From our conference presentations, we have received many comments and questions about this USDOT project. It is obvious to us that, the use of autonomous robotic platforms such as UAV is the future of efficient inspection and monitoring of civil infrastructure systems.

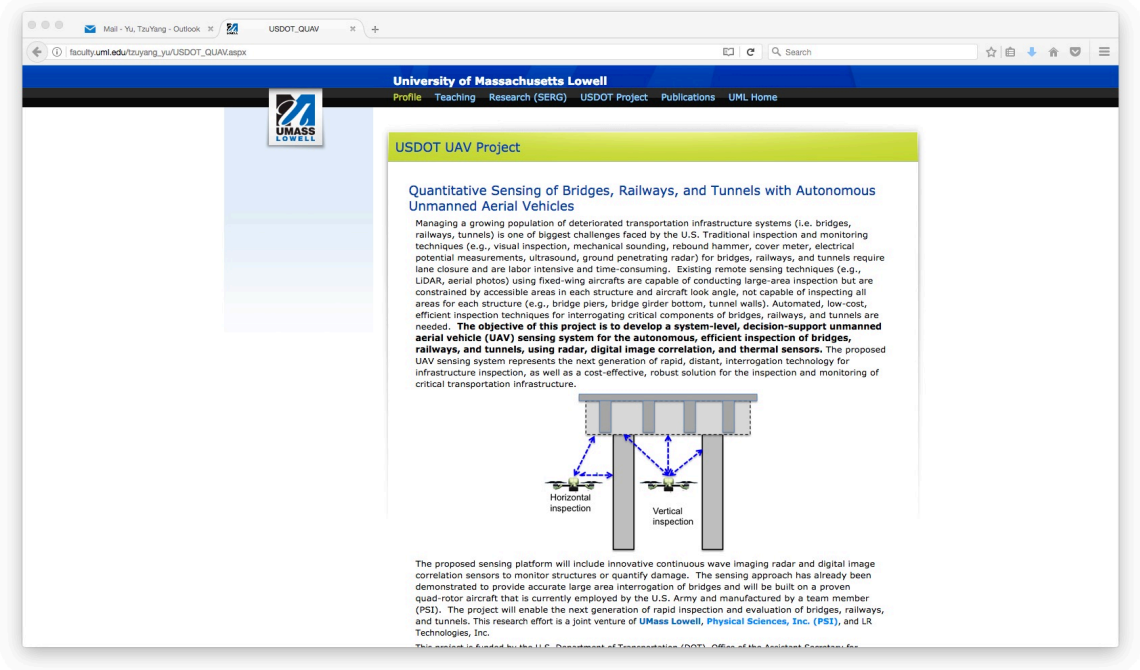

Fig. 106. USDOT project website

The list of our conference presentations is provided in the following, as well as our published/accepted journal publications.

Conference presentations

- Yu, T., C. Nonis, C. Niezrecki, S. Ahmed, C-F Su, X. Zou, X. Wang (2014). Multi-modal remote sensing for the condition assessment of concrete bridges using distant imaging radar and digital image correlation. Structural Congress, Structural Engineering Institute (SEI), ASCE, Boston, MA
- Gladstone, R., Yu, T. (2014), Denoising analysis of synthetic aperture radar images using discrete wavelet transform for the radar NDE of concrete specimens. In: *Proc SPIE Smart Structures/NDE*, Mar. 9-13, San Diego, CA.

- Yu, T., J. Owusu-Twumasi (2014). Dielectric modeling of cementitious specimens using an open-ended coaxial probe in the frequency range of 0.5GHz to 4.5 GHz. *Proc SPIE Smart Structures/NDE*, Vol. 8694, Mar. 11-14, San Diego, CA.
- Le, V., T. Yu (2014). Mass and stiffness estimation using mobile devices for structural health monitoring. In: *Proc SPIE Smart Structures/NDE*, Vol. 9437, Mar. 8-12, San Diego, CA; doi: 10.1117/12.2084036
- Owusu Twumasi, J., T. Yu (2015). Forward and inverse dielectric modeling of oven-dried cement paste speicmens in the frequency range of 1.02 GHz to 4.50 GHz. In: *Proc SPIE Smart Structures/NDE*, Vol. 9437, Mar. 8-12, San Diego, CA; doi: 10.1117/12.2075672
- Tang, Q., T. Yu (2015), M. Jen. Finite element analysis for the damage detection of light pole structures. In: *Proc SPIE Smart Structures/NDE*, Vol. 9437, Mar. 8-12, San Diego, CA; doi: 10.1117/12.2075689
- Le, V.Q., T. Yu, J. Owusu Twumasi, Q. Tang (2016). Sizing and ranging criteria for SAR images of steel and wood specimens. In: *Proc SPIE Smart Structures/NDE*, Mar. 20-24, Las Vegas, NV; doi: 10.1117/12.2218441.
- Owusu Twumasi, J., V.Q. Le, Q. Tang, T. Yu (2016). Quantitative sensing of corroded steel rebar embedded in cement mortar specimens using ultrasonic testing, In: *Proc SPIE Smart Structures/NDE*, Mar. 20-24, Las Vegas, NV; doi: 10.1117/12.2218451
- D'Amico, N., T. Yu (2016). Photogrammetric analysis of concrete specimens and structures for condition assessment, In: *Proc SPIE Smart Structures/NDE*, Mar. 20-24, Las Vegas, NV; doi: 10.1117/12.2218640
- Reagan, D.R., C. Niezrecki, T. Yu, A. Sabato, R. Wilson (2016). An autonomous unmanned aerial vehicle sensing system for structural health monitoring of bridges, In: *Proc SPIE Smart Structures/NDE*, Mar. 20-24, Las Vegas, NV; doi: 10.1117/12.2218370
- Reagan, D.R., A. Sabato, C. Niezrecki (2017), Unmanned aerial vehicle acquisition of three-dimensional digital image correlation measurements for structural health monitoring of bridges, In: *Proc SPIE Smart Structures/NDE*, Mar. 26-29, Portland, OR (in press)
- D'Amico, N, T. Yu (2017)**,** Accuracy Analysis of Point Cloud Modeling for Evaluating Concrete Specimens, In: *Proc SPIE Smart Structures/NDE,* Mar. 25-29, Portland, OR (in press)
- Ingemi, C., J. Owusu Twumasi, S. Litt, T. Yu (2017), Condition assessment of Corroded Steel Rebar in Free Space using Synthetic Aperture Radar Images, In: *Proc SPIE Smart Structures/NDE*, Mar. 25-29, Portland, OR (in press)
- Yu, T. (2017), Synthetic aperture radar image processing techniques for damage detection of FRP-concrete systems, In: *Proc SPIE Smart Structures/NDE*, Mar. 25-29, Portland, OR (in press)

Journal publications

- Yu, T. (2016), Quantitative Assessment of CFRP-concrete Cylinders using Synthetic Aperture Radar Images, *Research in Nondestructive Evaluation (RNDE)*, doi: 10.1080/09349847.2016.1173266.
- Yu, T., J. Owusu-Twumasi, V. Le, Q. Tang, N. D'Amico (2017), Surface and Subsurface Remote Sensing of Concrete Structures using Synthetic Aperture Radar Imaging, ASCE, *Journal of Structural Engineering* (Accepted)

Degree theses

- D'Amico, N. (2017), *Photogrammetric Techniques forEvaluation and Analysis of Concrete Structures and Specimens*, Master's Thesis, Department of Civil and Environmental Engineering, University of Massachusetts Lowell, Lowell, MA.
- Reagan, D.R. (2017), *Unmanned Aerial Vehicle Measurement Using Three-Dimensional Digital Image Correlation To Perform Bridge Structural Health Monitoring*, Master's Thesis, Department of Mechanical Engineering, University of Massachusetts Lowell, Lowell, MA.

8.2 Commercialization Plan

The research team has worked closely with the Office of Technology Commercialization (OTC) at UML and our industry team members (PSI and LR Tech.) to identify potential patents and business models for commercialization. We understand both performance and cost are critical to the end users in the transportation industry. A high-performance, cost-effective technology for the condition assessment of transportation infrastructure is what the market needs.

Keys to the success of the CivilEye system include: low cost, operational simplicity and plug and play payloads to tailor the system for particular operations. We have developed CivilEye prototypes based on these key features. Two major sensing components (wireless airborne imaging radar and portable DIC sensors) are self-powered and wirelessly controlled for data collection and storage. The design concept allows us to use other UAV platforms for flying the imaging radar and DIC sensors, suggesting more possibilities of collaboration.

We also understand that it is important to allow the customer to acquire a multi-use technology thus spreading acquisition costs across several need areas. We have engaged end users (government and industry) to ensure that the developed CivilEye system meets their needs and is cost appropriate. Our current manufacturing model is: LR Tech builds the imaging radar; UML assembles the DIC sensor; and PSI constructs the UAV platform.

In order to manage possible risks that may occur during the course of the project, we have identified performance matrices to ensure that i) project progress will be on schedule, ii) project cost will be monitored and controlled (both expenses and cost share),

iii) project quality/performance will be assured and controlled, iv) project scope will be preserved, and v) safety of participants in laboratory and field testing will be assured. Our strategies for managing risk are based on our prior experience in executing numerous successful federal and state funded projects.

From this project, we have developed a wireless imaging radar prototype with a user's manual (shown in Fig. 107) and a wireless DIC prototype with a user's manual (as shown in Fig. 108). We have developed GUI for data interpretation of the radar and DIC systems (Figs. 109 and 110). The hardware casing design has also been completed, as shown in Fig. 111. An adaptor for the modular connection between the imaging radar and other UAV platforms has been developed as well (Fig. 18).

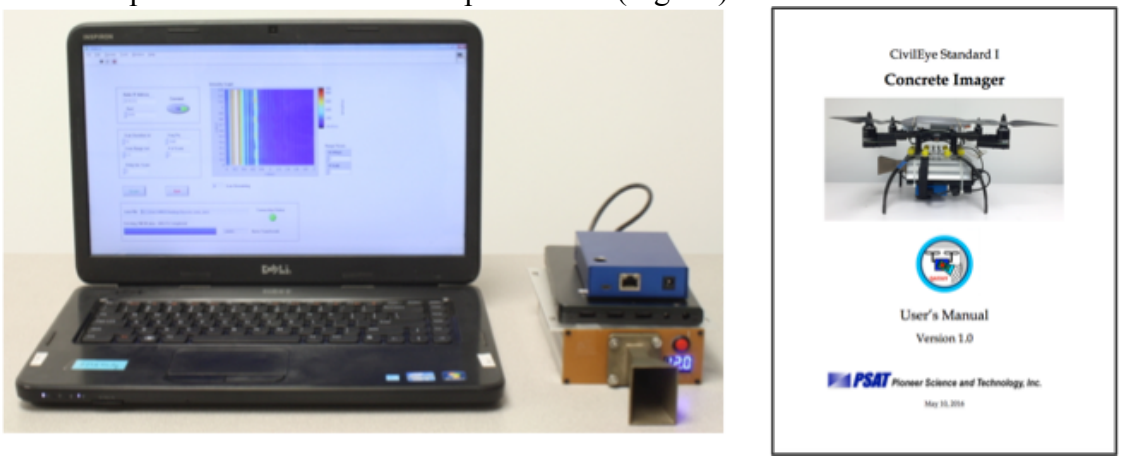

Fig. 107. Wireless imaging radar system and its manual

Fig. 108. Wireless DIC system and its manual

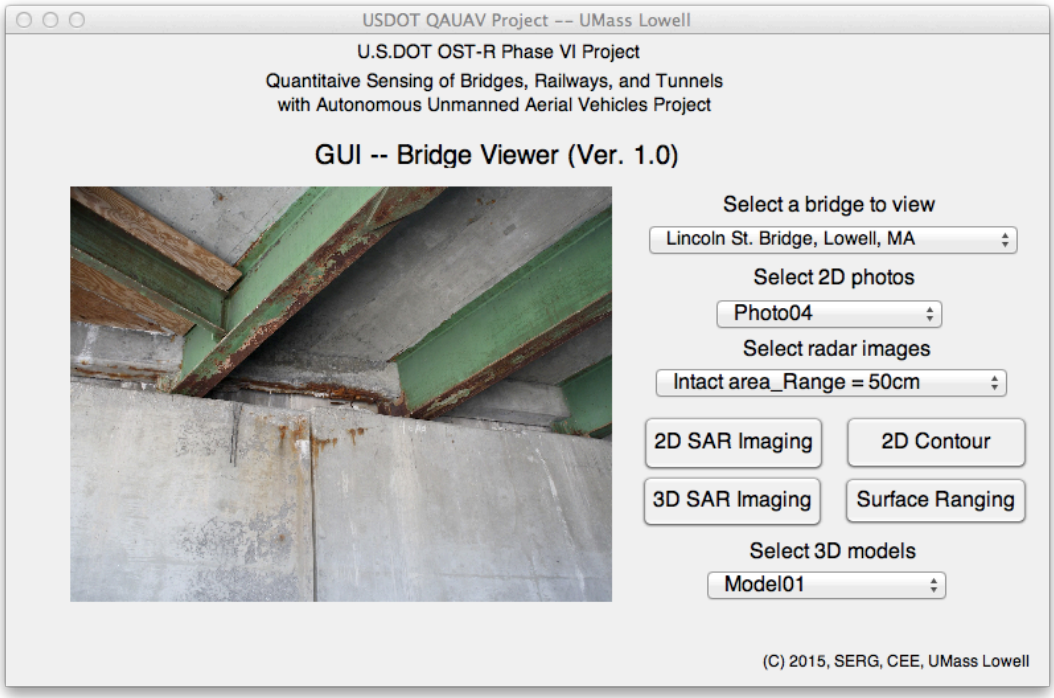

Fig. 109. Matlab-based GUI for condition assessment and decision support – Bridge Viewer

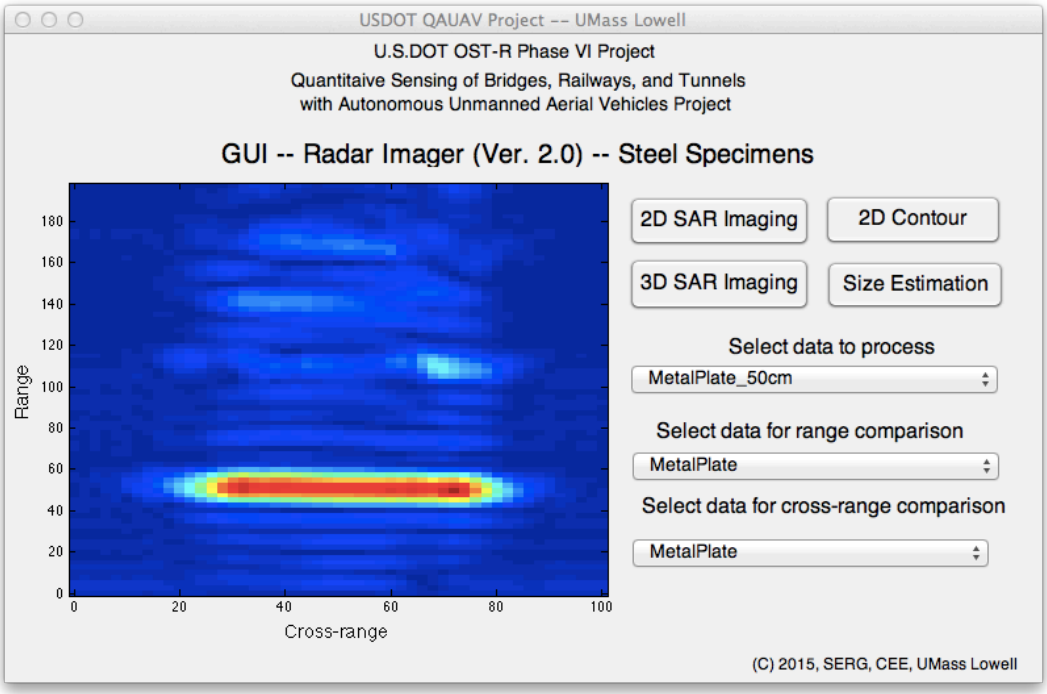

Fig. 110. Matlab-based GUI for condition assessment and decision support – Radar Imager

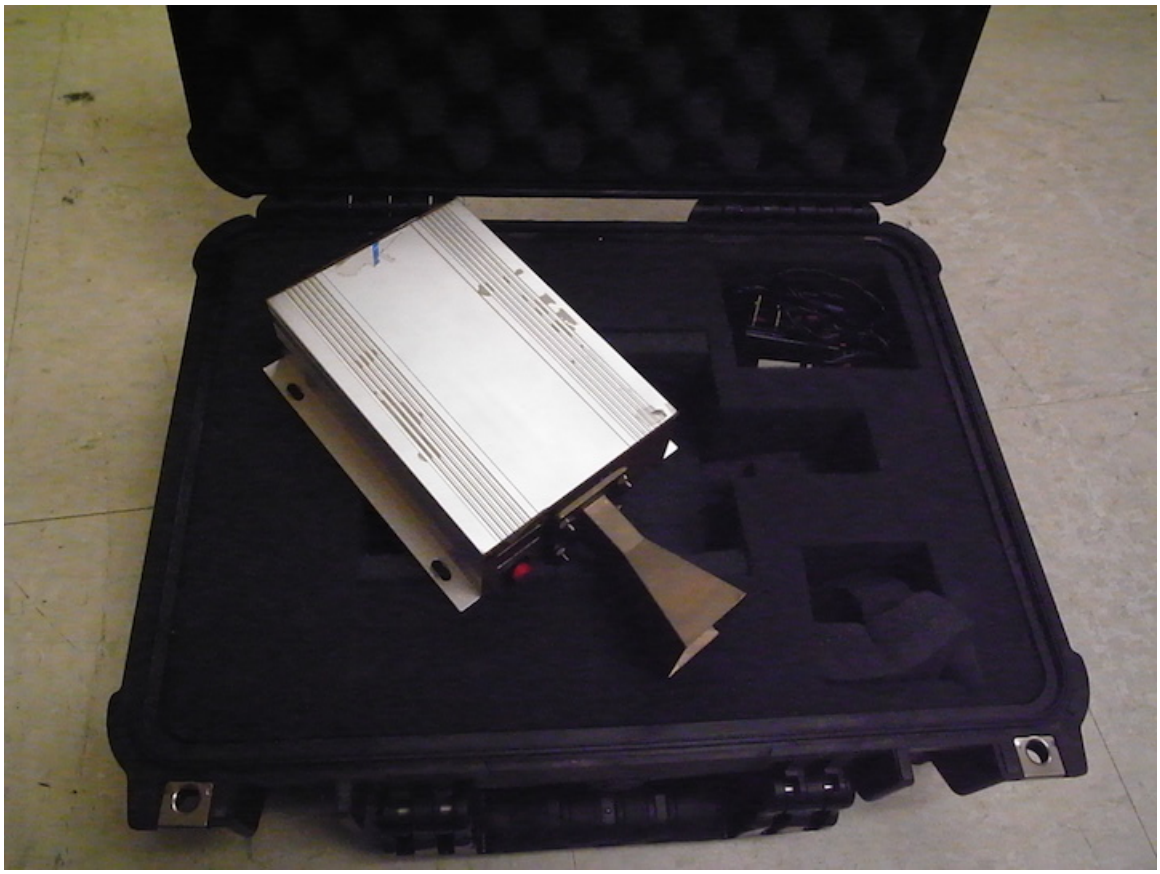

Fig. 111. Casing design of the CivilEye system for commercialization

Chapter 9. Conclusions

This USDOT project represents an effort to develop the next generation of rapid, low-cost interrogation/remote sensing technology for inspection and monitoring of critical transportation infrastructure. In the proposed CivilEye system, a decision-support asset analysis tool is first used to i) perform and assessment of the aging infrastructure systems and ii) prioritize the structures in need of inspection/repair. This analysis is performed based on the impact of each aged/deteriorated structure on various local traffic networks, using previous inspection records/reports. Once this system-level analysis is completed, the CivilEye system will be sent to the structure with the highest inspection priority. The proposed CivilEye system is capable of operating in two modes; CivilEye+Radar and CivilEye+DIC. The CivilEye system is designed to carry imaging radar and DIC sensors and is wirelessly controlled by a ground control station.

Our major research findings and conclusions are summarized in the following.

1. **3D point cloud modeling using photogrammetry** – The use of high definition (HD) videos to construct 3D point cloud models using 3D photogrammetry was demonstrated as promising tool for rapid prototyping and modeling of infrastructure systems.

2. **Digital image correlation (DIC) for surface sensing of concrete structures** – A wireless digital image correlation (DIC) sensor was applied to the long term monitoring of local and highway bridges and successfully identified the locations of surface distressing and concrete spalling.

3. **Synthetic aperture radar (SAR) imaging for subsurface sensing of concrete structures** – A wireless synthetic aperture radar (SAR) imaging sensor was developed for the subsurface sensing of concrete structures. Experimental results on bridges have demonstrated its capability to locate subsurface steel rebars inside bridge abutments and piers from 6 ft (2 m). The SAR imaging sensor was also applied for surface geometric characterization of concrete structures and successfully detect and locate concrete cracking.

4. **SAR imaging for strength estimation** – The developed wireless SAR imaging sensor was also used for estimating the surface mechanical strength of concrete bridges. A semi-empirical model was proposed to predict surface strength of concrete using SAR images. This new finding has the potential to significantly accelerate conventional bridge rating procedures by surface strength mapping/profiling of concrete bridges.

5. **UAV mobility in infrastructure sensing** – A new UAV platform (quad-rotor) was developed for enabling the autonomous inspection of bridges, railway, and tunnels, using a wireless SAR imaging sensor and a DIC sensor. This platform was field tested in both GPS-available and GPS-denied environments. Mobility provided by the UAV platform enables engineers to transport innovative sensors

to the difficult locations under inspection, such as the bottom side of high-elevation, long-span bridges. Such mobility can significantly reduce inspection and improve inspection efficiency (time) by performing infrastructure inspection without sending human inspectors and without closing traffic (lane closure).

6. **Multiphysical data fusion using 3D photogrammetry** – Our laboratory and field test results showed that, 3D photogrammetry can be used as a reliable tool to integrate multiphysical measurements such as SAR images and DIC images. 3D point cloud models of structures provide a versatile platform for integrating spatial results of different sensors. 3D photogrammetry offers a digital platform for data registration, assisting the end users to better locate suspicious/damaged locations and to improve damage detectability by using data in multiple formats. This integration can be used in infrastructure asset management (e.g., Pontis).

7. **Integration between radar image and mechanical strength** – From the integration between SAR images and mechanical strength distribution, it is found that the SAR amplitude of weak concrete is higher than the one of strong concrete. This can be explained by the moisture content of concrete since wet concrete has lower mechanical strength than dry concrete. Consequently, wet concrete produces higher SAR amplitudes, due to the high effective dielectric constant of wet concrete.

From conducting this project, we have learned the challenges in integrating various technologies into a practical sensing solution for civil infrastructure inspection and monitoring. Constraints and limitations in infrastructure inspection and monitoring problems are often unique and more challenging than the ones in other disciplines. And yet, innovative remote sensing solutions are needed for the nation's aging civil infrastructure. It can be expected that performance effective and cost efficient remote sensing solutions like the CivilEye system will play an important role in the near future of sustainable infrastructure management.

Acknowledgement

This USDOT is a team effort that will not be possible without the contributions from UML faculty researchers (Drs. Christopher Niezrecki, Nathan Gartner, and Iaonnis Raptis) and student researchers (Mr. Viet Le (Master's student in Civil Engineering), Mr. Jones Owusu Twumasi (doctoral student in Civil Engineering), Mr. Qixiang Tang (doctoral student in Civil Engineering), Mr. Nicolas D'Amico (Master's student in Civil Engineering), Mr. Daniel Reagan (Master's student in Mechanical Engineering), Mr. Mehmet Ali Guney (doctoral student in Mechanical Engineering)) and industry team members from Physical Sciences Inc. (PSI) (Mr. Dave Manegold, Dr. Richard Wilson) and LR Technologies Inc. (Drs. David Lai and Yexian Qin). Indispensable assistance from the MassDOT (Mr. Alexander Bardow) and the City Lowell (Ms. Lisa DeMeo) on field tests is greatly appreciated. In addition, the team also wants to express our appreciations on the comments and suggestions received from our technical advisory board/council members.

Finally, the team thanks the program manager Mr. Caesar Singh, P.E. at U.S.DOT for providing valuable advice and suggestions toward the success of this project.

REFERENCES

- Abdullah. H., M.S. Sabilurrashad, I.M. Ibrahim, R. Ariffin, S.Z. Jalil, W.K. Ali, M.N. Taib (2009), "Design of Portable Mini Anechoic Chamber Using Low Cost Composite Absorber." *IEEE Student Conference on Research and Development*, 526-528.
- Aggelis D.G., E.Z. Kordatos, D.V. Soulioti, T.E. Matikas (2010), "Combined use of thermography and ultrasound for the characterization of subsurface cracks in concrete." *Construction and Building Materials*, 1888-1897.
- Aggelis D.G., E.Z. Kordatos, D.V. Soulioti, T.E. Matikas (2011), "NDT approach for characterization of subsurface cracks in concrete," *Construction and Building Materials*, 3089-3097.
- Avendano, J., L.D. Otero, P. Cosentino (2013), "Towards the development of a complex structural inspection system using small-scale aerial vehicles and image processing." *Systems Conference (SysCon)*, IEEE International, Orlando, FL; 420-425.

- Benitz, G.R. (1997), "High-definition vector imaging," *Lincoln Laboratory Journal* Vol. 10 (2), 147-169.
- Bennett, P.J., F.R. Rutz (2012). "Structural health monitoring with interferometric radar." *Forensic Engineering*; 28-37.
- Bu, H., X. Bai, R. Tao (2010), "A Novel Algorithm for Synthetic Aperture Radar Imaging Based on Compressed Sensing", *Signal Processing* (ICSP), IEEE 10th International Conference; 2210-2213.
- Bungey, J.H. (2004), "Sub-surface radar testing of concrete: a review." *Construction Building Materials*; 18: 1-8.

- Chen, J., X. Zhang, N. Zhan, X. Hu (2010), "Deformation measurement across crack using two-step extended digital image correlation method." *Optics and Lenses in Engineering*, 1126–1131.
- Chowdhury. N.M. A, Hossain. S., Zhao. L., Liao. Z (2008). "Low Cost Indoor Environment for antenna measurement." *IEEE Journal*, 001353-001356.
- Collin Engineering Inc. (2010), "Indiana Bridge Inspection Manual," Part 6, Chapter 1~16, 6-1-1 ~ 6-16-2.
- Cox, B.N., D.B. Marshall (1991), "The determination of crack bridging forces," *International Journal of Fracture* 49: 159-176.
- Cyphy Works, Inc. (2014), website: http://cyphyworks.com/robots/parc/. Website acessed: Nov. 10, 2014.

- D'Amico, N., T. Yu (2016). Photogrammetric analysis of concrete specimens and structures for condition assessment, In: *Proc SPIE Smart Structures/NDE*, Mar. 20-24, Las Vegas, NV; doi: 10.1117/12.2218640
- D'Amico, N. (2017), *Photogrammetric Techniques forEvaluation and Analysis of Concrete Structures and Specimens*, Master's Thesis, Department of Civil and Environmental Engineering, University of Massachusetts Lowell, Lowell, MA.

- D'Amico, N, T. Yu (2017), Accuracy Analysis of Point Cloud Modeling for Evaluating Concrete Specimens, In: *Proc SPIE Smart Structures/NDE,* Mar. 25-29, Portland, OR (in press)
- Daniels, D.J. (2007), *Ground Penetrating Radar*. 2nd ed., UK: The Institution of Engineering and Technology.
- Deng, L., C.S. Cai (2007), "Applications of fiber optic sensors in civil engineering," *Structural Engineering and Mechanics*, Vol. 25, P. 577-596
- Destrebecq, J., E. Toussaint, E. Ferrier (2011), "Analysis of Cracks and Deformations in a Full Scale Reinforced Concrete Beam Using a Digital Image Correlation Technique." *Experimental Mechanics* 51: 879-890.
- Draganfly Innovations, Inc. (2017), website: http://www.draganfly.com/, Canada, Website accessed: Sep. 5, 2015.

- FHWA (2001), "Highway Bridge Inspection: State-of-the-Practice Survey," FHWA-RD-01-033, NDE Validation Center, U.S.DOT, Research, Development, and Tech.McLean, VI.
- Forward Florida Project (2014), Florida DOT. http://forwardflorida.com/florida-transportation/bridging-safety-gap/, Website accessed: Oct. 20, 2014.

- Germaneau A., P. Doumanlin, J.C. Dupre (2007), "Full 3D measurement of strain field by scattered light for analysis of structure," *Experimental Mechanics*, 47: 523-532.
- Gladstone, R., T. Yu (2014), "Denoising analysis of synthetic aperture radar images using discrete wavelet transform for the radar NDE of concrete specimens." In: *Proc SPIE Smart Structures/NDE*, Mar. 9-13, San Diego, CA.

- Hallermann, N., G. Morgenthal (2014), "Visual inspection strategies for large bridges using Unmanned Aerial Vehicles (UAV)," *Bridge Maintenance, Safety, Management and Life Extension* - Chen, Frangopol & Rural (eds). Taylor & Francis Group, London.
- Hammer, A., J. Dumoulin, B. Vozel, K. Chehdi (2007), "Deblurring of UAV aerial images for civil structures inspections using Mumford-Shah/Total variation regularization." In: *Proceedings of 5th International Symposium on Image and Signal Processing and Analysis*, ISPA: 262–267.
- Helfrick, M., Niezrecki, C., Avitabile, P., and Schmidt, T. (2008), "3D Digital Image Correlation Methods for Full-Field Vibration Measurement," In: *Proc. IMAC-XXVI*, Orlando, FL, February.
- Helfrick, M., Pingle, P., Niezrecki, C., and Avitabile, P. (2009a), "Using Full-Field Vibration Measurement Techniques for Damage Detection," In: *Proc. IMAC-XXVII*, Orlando, FL, February.
- Helfrick, M., Niezrecki, C., and Avitabile, P. (2009b), "Curvature Methods of Damage Detection using Digital Image Correlation," In: *Proc. SPIE Smart Structures/NDE*, San Diego, California, March 8-12.
- Hild, F., S. Roux (2006), "Measuring stress intensity factors with a camera: Integrated digital image correlation (I-DIC)," *Comptes Rendus Mechanique*, 334: 8–12.

- Hoegh K, L. Khazanovich (2015), "Extended synthetic aperture focusing technique for ultrasonic imaging." *NDT&E International*; 74: 33-42.
- Hößler, T., T. Landgraf (2014), "Automated Traffic Analysis in Aerial Images," In: *Proceedings of the 8th International Conference on Sensing Technology*, September 2-4, Liverpool, UK.

- Ingemi, C., J. Owusu Twumasi, S. Litt, T. Yu (2017), Condition assessment of Corroded Steel Rebar in Free Space using Synthetic Aperture Radar Images, In: *Proc SPIE Smart Structures/NDE*, Mar. 25-29, Portland, OR (in press)

- Jol, H.M. (2009), *Ground Penetrating Radar: Theory and Applications*. Amsterdam, The Netherlands; Elsevier.

- Kahn-Jetter, Z.L., T.C. Chu (1990), "Three-dimensional Displacement Measurements Using Digital Image Correlation and Photogrammic Analysis," *Experimental Mechanics*, Vol. 30, No 1, 10–16.
- Kamaya, M., M. Kawakubo (2011), "A procedure for determining the true stress–strain curve over a large range of strains using digital image correlation and finite element analysis," *Mechanics of Materials*, 243-253.
- Kesavan, K. , K. Ravisankar, S. Parivallal, P. Sreeshylam, S. Sridhar (2010), "Experimental studies on fiber optic sensors embedded in concrete," *Measurement* Vol. 43, P. 157–163.
- Khan M. (2010), *Bridge and Highway Structural Rehabilitation and Repair*, McGraw Hill, 2010.
- Krause M., F. Mielentz, B. Milman B, Muller W, Schmitz V, H. Wiggenhauser (2001) "Ultrasonic imaging of concrete members using an array system." *NDT&E International*; 34: 403–8.

- Le, V., T. Yu (2014). "Mass and stiffness estimation using mobile devices for structural health monitoring." In: *Proc SPIE Smart Structures/NDE*, Vol. 9437, Mar. 8-12, San Diego, CA.
- Le, V.Q., T. Yu, J. Owusu Twumasi, Q. Tang (2016). "Sizing and ranging criteria for SAR images of steel and wood specimens." In: *Proc SPIE Smart Structures/NDE*, Mar. 20-24, Las Vegas, NV.
- Lecompte, D., J. Vantomme, H. Sol (2006), "Crack Detection in a Concrete Beam using Two Different Camera Techniques," *Structural Health Monitoring* 5: 59-68.
- Li. Z., R.M. Narayanan (2006), "Data Level Fusion of Multilook Inverse Synthetic Aperture Radar (ISAR) Images", *Applied Imagery and Pattern Recognition Workshop*, 35th IEEE AIPR Conference.
- Luo, P.F., Chao, Y.J., Sutton M.A., and Peters, W.H. (1993), "Accurate Measurement of Three-Dimensional Deformations in Deformable and Rigid Bodies using Computer Vision," *Experimental Mechanics*, Vol. 33, No 2, 123-132.

- Metni, N., T. Hamel (2007), "A UAV for bridge inspection: Visual servoing control law with orientation limits." *Automation in Construction* 17: 3–10.

- Mulle, M., R. Zitoune, F. Collombet, L. Robert, Y. Grunevald (2009). "Embedded FBGs and 3-D DIC for the stress analysis of a structural specimen subjected to bending," *Composite Structure*s, 48-55.

- NBI (2007), "2006 Status of the Nation's Highways, Bridges, and Transit: Conditions and Performance – Report to Congress," Federal Highway Administration, Washington, DC, January 22.
- NIST TIP (2014), website: http://www.nist.gov/tip/. Website accessed: Nov. 10, 2014.

- Owusu Twumasi, J., T. Yu (2015). "Forward and inverse dielectric modeling of oven-dried cement paste speicmens in the frequency range of 1.02 GHz to 4.50 GHz," In: *Proc SPIE Smart Structures/NDE*, Vol. 9437, Mar. 8-12, San Diego, CA.
- Owusu Twumasi, J., V.Q. Le, Q. Tang, T. Yu (2016). "Quantitative sensing of corroded steel rebar embedded in cement mortar specimens using ultrasonic testing," In: *Proc SPIE Smart Structures/NDE*, Mar. 20-24, Las Vegas, NV.

- Pieraccini, M., G. Luzi, D. Mecatti, M. Fratini, L. Noferini, L. Carssimi, G. Franchioni, C. Atzeni (2004). "Remote sensing of building structural displacements using a microwave interferometer with imaging capability." *NDT&E International*; 37(7): 545-50

- Reagan, D.R., C. Niezrecki, T. Yu, A. Sabato, R. Wilson (2016). "An autonomous unmanned aerial vehicle sensing system for structural health monitoring of bridges," In: *Proc SPIE Smart Structures/NDE*, Mar. 20-24, Las Vegas, NV.
- Reagan, D.R. (2017), *Unmanned Aerial Vehicle Measurement Using Three-Dimensional Digital Image Correlation To Perform Bridge Structural Health Monitoring*, Master's Thesis, Department of Mechanical Engineering, University of Massachusetts Lowell, Lowell, MA.
- Reagan, D.R., A. Sabato, C. Niezrecki (2017), Unmanned aerial vehicle acquisition of three-dimensional digital image correlation measurements for structural health monitoring of bridges, In: *Proc SPIE Smart Structures/NDE*, Mar. 26-29, Portland, OR (in press)
- Rhim H., O. Buyukozturk (2000). "Wideband microwave imaging of concrete for nondestructive testing." *ASCE Journal of Structural Engineering*; 126 (12): 1451-1457.

- Sansalone M, W.B. Street (1997). *Impact-echo Nondestructive Evaluation of Concrete and Masonry*, Ithaca NY: Bullbrier Press.
- Sasaki, K.K., T. Paret, J.C. Araiza, P. Hals (2010), "Failure of concrete T-beam and box-girder highway bridges subjected to cyclic loading from traffic," *Engineering Structures* 32, 1838-1845.
- Schickert M, M. Krause, W. Muller (2003). "Ultrasonic imaging of concrete elements using reconstruction by synthetic aperture focusing technique." *ASCE Journal of Materials in Civil Engineering*; 15(3): 235–246.

- Sham F.C., N. Chen, L. Long (2008), "Surface crack detection by flash thermography on concrete surface," *Insight*, 240-243.
- Shiau, J.K., D.M. Ma, P.Y. Yang, G.F. Wang, J.H. Gong (2009), "Design of a solar power management system for an experimental UAV", *IEEE Transactions on Aerospace and Electronic Systems*, 45(4), 1350-1360.
- Shinozuka, M., R. Ghanem, B. Houshmand, B. Mansouri (2000), "Damage detection in urban areas by SAR imagery." *ASCE Journal of Engineering Mechanics*; 126(7): 769-777.
- Sumitro, S., S. Nishimura, H. Matsuda, I. Bartoli (2013), "GPS-based remote optical monitoring system for structural inspection." *Safety, Reliability, Risk and Life-Cycle Performance of Structures & Infrastructures*, Deodatis, Ellingwood & Frangopol (Eds), Taylor & Francis Group, London, UK.

- Tang, Q., T. Yu, M. Jen (2015). "Finite element analysis for the damage detection of light pole structures." In: *Proc SPIE Smart Structures/NDE*, Vol. 9437, Mar. 8-12, San Diego, CA.

- Warren, C., C. Niezrecki, P. Avitabile (2009), "Dynamic Monitoring of Rotating Blades Using Digital Image Correlation," In: *Proc. 7th Intl. Workshop on Structural Health Monitoring*, Stanford, CA, Sept. 9-11.
- Wu, Z., H. Rong, J. Zheng, F. Xu, W. Dong (2011), "Experimental investigation on the FPZ properties in concrete using digital image correlation technique," *Engineering Fracture Mechanics* 78; 2978-2990.

- Xu. L., J. Li, P. Stoica (2006), "Radar Imaging Via Adaptive MIMO Techniques," *14th European Signal Processing Conference*.

- Yang, J., L. Yuan (2009), "Package and installation of embeddable fiber optic sensors," *Optics and Lasers in Engineering*, Vol. 47, 1085-1090.
- Yu, T., C. Nonis, C. Niezrecki, S. Ahmed, C-F Su, X. Zou, X. Wang (2014). "Multi-modal remote sensing for the condition assessment of concrete bridges using distant imaging radar and digital image correlation." *Structural Congress*, Structural Engineering Institute (SEI), ASCE, Boston, MA
- Yu, T. (2009), "Damage Detection of GFRP-concrete Systems Using Electromagnetic Waves." Lambert Academic Publishing, Koln, Germany.
- Yu, T. (2011), "A distant damage assessment method for multi-layer composite systems using electromagnetic waves," *ASCE Journal of Engineering Mechanics*, 137 (8): 547-560.
- Yu, T., T.K. Cheng, A. Zhou, D. Lau (2016). "Remote defect detection of FRP-bonded concrete system using acoustic-laser and imaging radar techniques." *Construction Building Materials*; 109: 146-155.
- Yu, T., J. Owusu-Twumasi (2014). "Dielectric modeling of cementitious specimens using an open-ended coaxial probe in the frequency range of 0.5GHz to 4.5 GHz." In: *Proc SPIE Smart Structures/NDE*, Vol. 8694, Mar. 11-14, San Diego, CA.

- Yu, T. (2011), "Distant Damage Assessment Method for Multi-layer Composite Systems using Electromagnetic Waves," *ASCE Journal of Engineering Mechanics*, Vol. 137, No. 8, 547–560.
- Yu, T. (2016), "Quantitative Assessment of CFRP-concrete Cylinders using Synthetic Aperture Radar Images," *Research in Nondestructive Evaluation (RNDE)*, April, 1-18.
- Yu, T., O. Buyukozturk (2008). "A far-field airborne radar NDT technique for detecting debonding in GFRP-retrofitted concrete structures." *NDT&E International*; 41: 10-24.
- Yu, T., J. Owusu-Twumasi, V. Le, Q. Tang, N. D'Amico (2017), "Surface and Subsurface Remote Sensing of Concrete Structures using Synthetic Aperture Radar Imaging," ASCE, Journal of Structural Engineering (*Accepted*)